Optimization of Electrodes Towards More Practical Electrochemical Water Treatment

Thesis by

Heng Dong

In Partial Fulfillment of the Requirements for
the degree of
Doctor of Philosophy

Caltech

CALIFORNIA INSTITUTE OF TECHNOLOGY
Pasadena, California

2023
(Defended February 08, 2023)

© 2023
Heng Dong
ORCID: 0000-0002-4168-7297

ACKNOWLEDGEMENTS

My memories flood back to me as I put down the first words here. I still remember my anxiety when approaching the “Visiting Scholars” office in the summer of 2017 in the School of Environment, Tsinghua University, my alma mater. I carefully knocked on the door while murmuring my greetings, only to see a gentleman, Dr. Michael R. Hoffmann, in a suit who greeted me in unfluent Chinese with a smile. For the next 30 min, besides Mike’s knowledge and personal charisma, I was especially moved by his attitude towards research: “do meaningful research.” Mike has been constantly inspiring me in the same way during my entire Ph.D., and his academic attitude has surely, to a very large extent, influenced my choice of thesis research topic. That being said, I also appreciate Mike for allowing me to freely explore the electrochemical water treatment field and pursue my interest. Besides the academic advice, I will also remember and appreciate the personal advice Mike gave me as if he was my senior family member. My experience at Caltech could never be as enjoyable and rewarding without Mike.

I also feel privileged to have my committee members Professor George Rossman, Professor Harry Gray, Professor Kim See, and Professor Paul Wennberg, who offered me advice and guidance on my thesis work. Apart from Mike, George is the person I learned the most from at Caltech, and I am happy to say that George is more of a good friend to me than a supervisor. I remember how pressured I was each time I tried to reach out to him with mineralogy questions during my first year, and later realized how fast and how much I was growing being challenged and inspired by George. I love George’s collection of minerals in his office, and I am deeply touched by his sincere enthusiasm each time he introduced them to his new visitors like a tour guide.

Despite his myriad of academic achievements, I was shocked the most when Harry pronounced my name completely correctly the first time. His every question and every piece of advice was always right on spot. I am grateful for him being always responsive, patient, and helpful, and I want to specially thank him for being constantly concerned about my and my research group’s well-being.

I want to thank Kim for introducing me officially to the electrochemistry world. I had opened THE ELECTROCHEMISTRY TEXTBOOK many times before taking her class in electrochemistry, and always got frightened away in the end. That was why I felt so amazed as I found myself able to follow her deep into the electrochemistry theories without skipping any of the tough parts. I especially appreciate the last part of the class when she asked each one of us to select and re-review an already published paper in electrochemistry, and encouraged us to be brave enough to say “The paper is actually not worth publishing.” That has been an iconic piece to contribute to my overall impression of Caltech.

I want to thank Paul for his enormous help throughout, and especially during the final year of, my Ph.D. I feel lucky to have Paul on both my qualification exam committee and thesis advisory committee. His creative and ingenious questions always push me to think further about the scientific problems. I want to specially thank Paul for helping with my graduation process.

I want to thank Nora, Julie, and Bronagh for their constant support. Thank you for making the department a sweet home for me.

I am very grateful to the Bill and Melinda Gates Foundation and Safran for their generous funding support. I have also learned a lot from them on how technologies could, and should, be applied in the real world.

I always feel blessed to work with a great group of fellow graduate students, postdocs scholars, undergraduate students, and scientists: Yi Zhang, Dr. Alan Gu, Dr. Sean Seungkyeum, Axl LeVan, Dr. Cody Finke, Léopold Dobelle, Dr. Menglin Yu, Dr. Sean McBeath, Dr. Lei Guo, Dr. Soudabeh Saeid, Dr. Yang Yang, Dr. Kai Liu, Dr. Clement Cid, Dr. Jing Li, Dr. Eric Huang, Dr. Xingyu Lin, Dr. Su Young Ryu, Dr. A. J. Colussi, Hugo Leandri, Parker Deptula, Luana Dos Santos, Nicolas Jimenez-Lozano, Vignesh Vinayagam, Professor Lifeng Yin, Professor Yunrong Dai, and many others. I want to thank my collaborators outside of my research group, Xiaohan (Anita) Shao and Dr. Weilai Yu. I have not only learned a lot from, but also had great fun with them. My thesis work could be done in no way without them. I want to specially thank Yi Zhang, Léopold Dobelle, Parker Deptula, Luana Dos Santos, Dr. Sean McBeath, and Dr. Lei Guo for sharing a lot of interesting, stupid, and ridiculous moments with me in the lab and in the office. It was those moments that made my lab experiences more colorful and enjoyable.

I want to thank my friends Zhiquan Yuan, Yongzhao Guo, Yangcheng Luo, Yuanlong Huang, Guanya Shi. My Ph.D. would be incomplete without those eating, drinking, chatting, and basketball moments. I also want to thank my friends Xiao Zhang, Ning Yang, Zhe Li, Xianghao Chen, Lisheng Wang, Keren Zhou, Danqia Peng, and so many more for remotely supporting me through my Ph.D.

I want to give a special shout-out to my pals in CaltechC committee, Ziyi Wang, Ziran Zhou, Ding Zhong, Guanya Shi, Shengduo Liu, Ziyang Qin, Yue Bai, Haoyu Li, Haixu Shen, Yameng Zhang, Yuchun Sun, Jiajing Mao, and Xuefei Wang. I will not forget our effort of trying to make the Caltech Chinese community feel at home at Caltech, and it is even harder for me to forget about the barbecue we made, the cards we played, the boat we rode in, and the tour we shared.

Finally, I would like to thank my girlfriend Wenting Dai for being who you are and being who you are to me. Thanks to my parents and my family. I am coming home soon.

ABSTRACT

Due to water scarcity and water pollution, the world suffers from continuing water sanitation issues, which lead to billions of water-borne disease cases every year. Decentralized water treatment is regarded as an important supplement to the conventional wastewater treatment system to address the water sanitation and water pollution issues in rural, remote, and undeveloped regions. Electrochemical water treatment technology has been demonstrated to be feasible for decentralized water treatment systems because of the ambient operation conditions, robust performance, modular design, small footprint, and environmental compatibility. The performance of electrochemical water treatment systems relies heavily on the choice of electrodes. This thesis presents a comprehensive study towards understanding and optimizing the electrodes to enhance the performance and lower the cost of electrochemical water treatment systems. The research work on anodes followed an "understanding – development" approach and spanned both the scientific and engineering sides of the spectrum. Specifically, a comprehensive review was assembled through the analysis of existing literature on mixed metal oxide anodes. This review pointed towards potential future research directions. With the advancement of material sciences, it is important to focus not only on single catalytic metal elements, but also on the intermetallic electronic interaction to gain a deeper understanding of the catalytic activity of mixed metal oxides. The microscopic steric effects imposed by crystalline structures may also be a nonnegligible contributor to the catalytic properties.

Following the review, this thesis scrutinized the catalytic sites of crystalline $CoSb_2O_6$, an emerging anode for chlorine evolution reaction (CER) catalysis. It has been demonstrated to be a promising alternative for the conventional Ru- and Ir-based anodes based on its high activity and excellent stability, but its catalytic sites and mechanism are still unknown. By fabricating and testing a series of anodes with different Sb/Co ratios, it was discovered that the surface Sb/Co ratios in $CoSb_2O_6$ were ~50% higher than in the bulk. At the same time, it was surprising to find through scanning electrochemical microscopy (SECM) that Sb-rich samples showed higher catalytic activities, indicating that Sb sites may be even more active catalytic sites than the Co-sites. This was attributed to

the electronic interaction between Co and Sb, as revealed by X-ray photoelectron spectroscopy (XPS).

On the engineering side, a Ni–Sb–SnO_2 reactive electrochemical membrane (REM) was developed to treat primary effluent and greywater. In 30 min, the REM removed up to 78 ± 2% COD and 94 ± 0.6% turbidity from the primary effluent. The REM had ~100% COD removal and 89 ± 4% turbidity removal from greywater, with the effluent meeting the NSF/ANSI 350 standard. Compared to the conventional plate-type electrodes under the same conditions, the REM had 36% lower energy consumption for primary effluent treatment and 22% lower energy consumption for greywater treatment while yielding better treatment results. The REM-based electrochemical system was demonstrated to be a promising solution for decentralized wastewater treatment and recycling for single households and for vehicles.

Last but not the least, this thesis presents the 3D-printing-derived carbon lattice as a monolithic electro-Fenton cathode. The Fenton reaction is one of the most important advanced oxidation processes (AOPs) that is widely used in water treatment to remove non-biodegradable pollutants, and heterogeneous electro-Fenton (HEF) process catalyzed by carbon-based cathodes has received considerable attention as an evolving branch due to its wide working pH range and independence from chemical dosing. However, the conventional carbon cathodes suffered from poorly controlled porosities, which hampered the mass transport and limited the overall catalytic performance. Three rationally-designed carbon lattice cathodes with different macroscopic porosities were fabricated and tested, showing that it was feasible to facilitate the mass transport by tuning the macroscopic electrode structure. Specifically, Grid-2% cathode, which had the largest macroscopic porosity, showed 157% higher specific activity for electrochemical H_2O_2 production and 256% higher specific activity for trimethoprim degradation than the Star-2%, the one with the smallest macroscopic porosity. Grid-2% achieved 97% aqueous trimethoprim removal in 60 min, demonstrating the potential of the carbon lattice cathode to be used for water treatment and remediation.

PUBLISHED CONTENTS AND CONTRIBUTIONS

Dong, H.; Yu, W.; Hoffmann, M. R. Mixed Metal Oxide Electrodes and the Chlorine Evolution Reaction. *J. Phys. Chem. C* **2021**, *125* (38), 20745–20761. https://doi.org/10.1021/acs.jpcc.1c05671

H.D. and W.Y. conceived the idea. H.D. and M.R.H. analyzed the literature and wrote the paper. All authors provided critical feedback and edited the manuscript.

Dong, H.; Shao, X.; McBeath, S.; Tarpeh, W. A.; Hoffmann, M. R. Crystalline $CoSb_2O_6$ for Chlorine Evolution Reaction: Understanding the Catalytic Active Sites. *In preparation*.

H.D. conceived the idea. H.D. and X.S. designed the experiments. H.D., X.S. and S.M. finished the experiments. H.D. and X.S. analyzed the data. H.D. wrote the paper. W.A.T. and M.R.H. provided critical feedback.

Dong, H.; Dobelle, L.; Deptula, P.; Jimenez-Lozano, N.; Zhang, Y.; Cid, C. A.; Hoffmann, M. R. Heterojunction Ni–Sb–SnO_2 Reactive Electrochemical Membrane for Domestic Wastewater and Greywater Treatment. *In preparation*.

H.D., L.D., Y.Z. and C.A.C. conceived the idea. H.D. and L.D. designed the experimental plan. H.D., L.D., P.D., N.J. and Y.Z. finished the experiments. H.D., L.D., P.D. and N.J. analyzed the data. H.D. and D.L. wrote the paper. C.C.A. and M.R.H. provided critical feedback.

Dong, H.; Yu, M.; Hoffmann, M. R. Diffusion-Boosting Monolithic Electro-Fenton Cathodes Derived from 3D-Printing. *In preparation*.

H.D. and M.Y. conceived the idea, designed and finished the experiments as well as analyzed the data. H.D. wrote the paper. M.R.H. provided critical feedback.

TABLE OF CONTENTS

LIST OF FIGURES

LIST OF SUPPLEMENTARY FIGURES

LIST OF TABLES

LIST OF SUPPLEMENTARY TABLES

Chapter 1 Introduction

1.1 Decentralized water treatment problem

According to World Health Organization (WHO), as late as in 2020, 46% of the world population lacked access to safely managed sanitation service, and 45% household wastewater globally was discharged without safe treatment. As a result, 10% of the world population is believed to consume food irrigated by wastewater and at least 2 billion people globally use a drinking water source contaminated by feces. Microbiological contamination is estimated to lead to 485000 diarrhoeal deaths every year[1]. Consequently, the United Nations (UN) set a goal "clean water and sanitation" (Goal 6) among 17 sustainable development goals, with the Target 6.3 "By 2030, improve water quality by reducing pollution, eliminating dumping and minimizing release of hazardous chemicals and materials, halving the proportion of untreated wastewater and substantially increasing recycling and safe reuse globally."[2] Increased attention has been paid to creating ubiquitous access to proper water treatment systems for people all over the world, and especially in developing countries and regions. However, for conventional centralized water treatment systems, construction of treatment units as well as the massive water collection pipeline systems require adequate social infrastructure and substantial upfront investment. For scattered low-density populated regions, the upfront investment is often disproportionate to the population served[3]. Moreover, operating centralized water treatment plants require well-trained staff, who are unavailable in many remote or undeveloped regions and countries[4]. On the other hand, by keeping the treatment unit close to the waste source, decentralized treatment systems minimize the collection component. Meanwhile, they are often designed to have no or little requirement for chemical input or maintenance. Based on these features, decentralized treatment systems are identified to be more suitable for communities with low population density and varying site conditions, according to the United States Environmental Protection Agency (USEPA)[4].

Various technologies are applied for decentralized water treatment, including conventional septic tanks, constructed wetlands, biofiltration, membrane technologies, etc[3–5]. Electrochemical treatment has gained considerable attention as an emerging decentralized water treatment technology during the past two decades because of its ambient operation conditions, robust performance, modular design, small footprint, and the capability to adjust to different influent volume and composition[6]. It also features the compatibility with both grid power and alternative power sources such as photovoltaic (PV) cells. In the past decade, our research group developed electrochemistry-base wastewater management and recycling systems in the form of Caltech solar toilets, which were successfully applied in China, India, and South Africa to provide community-scale water sanitation solutions. However, application of electrochemical water treatment technologies in larger scales is hindered by its relatively high cost, which is specifically broken into CapEX and OpEX. CapEX is closely related to the price and the stability of the electrodes, while OpEX depends primarily on the energy cost[7]. Therefore, promoting the larger-scale application of electrochemical technologies as a means of decentralized treatment requires lowering both the electrode material cost and the operation energy consumption.

1.2 Technology background

1.2.1 Wastewater electrolysis

A wastewater electrolysis cell must have at least an anode, a cathode, and wastewater as the electrolyte. Under an applied voltage or current, the contaminants are degraded as a result of the redox reactions driven by the electrodes. Both reduction and oxidation reactions can contribute to the pollutant degradation[8,9], but oxidation reactions are essential in mineralization of the organic pollutants in water and deactivation of the pathogens in wastewater, especially when there is no other auxiliary treatment[10,11]. Oxidation of organic contaminants in an electrochemical cell can take place directly at the anode, or by reacting with electrochemically generated species[12].

Generally, water quality is evaluated by both its physical characteristics including odor, color, turbidity, presence of oily film and foam, and composition-based metrics, including organic compounds, which are usually accounted for by chemical oxygen demand (COD) or biological oxygen demand (BOD), pH, total nitrogen, total phosphorous, suspended solids (SS), pathogens, etc. To achieve effective wastewater sanitation and recycling, NSF/ANSI 350 and ISO/DIS 30500 standards impose requirements on disinfection and the removal of COD, total suspended solids (TSS), turbidity, total nitrogen, total phosphorous. In an electrochemical reactor, the organic compounds as well as the pathogens are generally removed by electrochemically triggered oxidation reactions. Meanwhile, phosphate is removed through forming hydroxyapatite with ammonia and magnesium[13]. Ammonia is removed by both struvite formation, and break-point chlorination, where the free chlorine stems from anodic chlorine evolution reaction (CER)[14]. Our research group has successfully employed electrochemical technology to treat aqueous organic pollutants including phenol, chlorinated phenols[11,15], various low-molecular-weight organic-acids[16], dyes, and pharmaceuticals[17] in simulated wastewater. Electrochemical oxidation (EO) also showed good performance in converting toxic aqueous As(III) to less toxic As(V)[18]. Meanwhile, the electrochemical reactor effectively removed over 95% COD and ammonia from domestic wastewater in 6 h[19]. With a mixed metal oxide anode, the electrolysis cell completely achieved 5-log removal of Coliphage MS2 within 10 min[20], and removed the COD from latrine wastewater in 4 h[6]. It is worth noting that when the anode and cathode chambers were separated with a cation exchange membrane (CEM), the direct energy consumption was reduced by over a half[21].

Simultaneously with the wastewater treatment, an electrochemical cell also produces H_2 by reducing water via the cathode, namely the hydrogen evolution reaction (HER). When powered by PV cell, a Bi-doped TiO_2 anode achieved >99% phenol removal in less than 10 min, with the cathodic current efficiency for hydrogen production close to 70% in 50 mM NaCl solution[15]. Interestingly, a synergistic effect between the anodic oxidative removal of organic substrates and cathodic HER was observed, which was attributed to the fact that the organics consumed the reactive radical species and prevented them to compete with protons to get reduced via the cathode[15,22]. It was observed that using inert electrolyte such as sulfate enhanced the cathodic HER efficiency compared to chloride electrolyte since there is no competing free chlorine reduction reactioni[11,15]. On the other hand, for experiments performed in actual municipal wastewater, the cathodic current efficiency in H_2 production was around 40%[22].

The produced hydrogen can be used to compensate the electricity cost during the treatment. In an electrochemical cell separated by a CEM, the produced H_2 was converted directly to electricity in a hydrogen-air fuel cell, which compensated 20% of the power consumption[21].

1.2.2 Anodic water oxidation and chlorine evolution reactions

One of the most widely used technologies for electrochemical wastewater treatment is electrochemical oxidation (EO), which relies on either direct anodic oxidation of organic substrates, or indirect oxidation based on anodic production of reactive oxygen species (ROS) and reactive chlorine species (RCS). Given the competing nature of these reactions, it is crucial to improve the Faradaic efficiency (FE) of the reactions that contribute to contaminant degradation. Generally, in domestic wastewater with a pH of 6-8 and a chloride concentration of ~30 mM, the prevalent anodic reactions are oxygen evolution reaction (OER, Eq 1) and chlorine evolution reaction (CER, Eq 2).

$$2\mathrm{H_2O} \rightleftharpoons \mathrm{O_2} + 4\mathrm{H^+} + 4\mathrm{e^-} \tag{1}$$

$$2\mathrm{Cl^-} \rightleftharpoons \mathrm{Cl_2} + 2\mathrm{e^-} \tag{2}$$

The standard thermodynamic potentials (E^θ) for OER and CER at standard conditions are +1.229 V and +1.358 V vs. SHE, respectively. In an electrochemical wastewater treatment cell, CER is primarily responsible for producing RCS, which includes not only Cl_2, but also HOCl and OCl^-. At elevated potentials (higher than +3 V vs. SHE), more oxidizing chlorine radicals ($Cl\cdot$, $Cl_2^-\cdot$) are produced[16]. On the contrary, the molecular oxygen produced by OER does not directly contribute to water treatment. However, it is worth mentioning that anodic water oxidation does not necessarily lead to molecular oxygen production. At higher applied potential, water may be directly oxidized to ozone (standard thermodynamic potential +2.07 V vs. SHE) and hydroxyl radicals ($\cdot OH$. standard thermodynamic potential 2.8 V vs. SHE), both of which are important ROS that contributes to calcitrant pollutant degradation and mineralization. Direct electron transfer (DET) between anode and the pollutant takes place when even higher potentials are applied. The anodic reactions are shown in Figure 1.

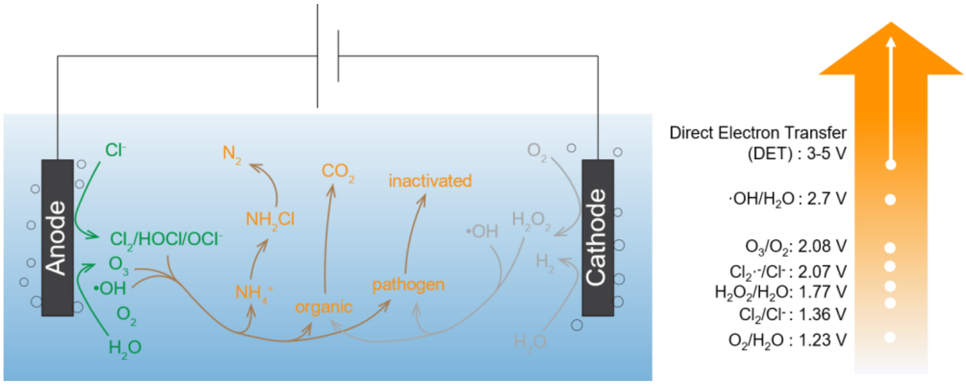

Figure 1.1. A diagram showing the anodic reactions.

The anode is a key for the EO performance. An ideal anode catalyzes the oxidation reactions with fast kinetics and high selectivity towards reactive species production, therefore increasing the efficiency while saving on operational costs. Depending on the overpotential for OER, anodes are generally classified into “active” anodes such as RuO_2, IrO_2, RuO_x-TiO_2, RuO_x-IrO_x-TiO_2, and “non-active” anodes such as boron doped diamond (BDD) and antimony doped tin oxide (ATO)[12]. “Active” anodes have low overpotential for OER and CER, which allows them to catalyze RCS production with fast kinetics at a relatively low applied potential. In the meantime, because of the high thermodynamic potentials of those reactions compared to that of OER and CER, “active” anodes tend to maintain high Faradaic efficiencies for OER and CER even at applied potentials where ozone and radical production as well as DET could take place. As a result, RCS was identified to be the major reactive species when the Ir-Ta based anode was used for domestic wastewater treatment[16,19].

On the other hand, “non-active” anodes have substantially higher overpotential for OER and CER catalysis than “active” anodes, which means that to catalyze CER at a comparable kinetics, “non-active” anodes consume more energy than “active” anodes. Nevertheless, the more sluggish OER and CER kinetics also result in higher Faradaic efficiencies for ozone and radical production at elevated applied potentials. Therefore, “non-active” anodes are often employed with a high applied potential to remove the recalcitrant pollutants by producing advanced oxidants like hydroxyl radicals and directly oxidizing the pollutants. In fact, BDD anode has been successfully used to degraded aqueous perfluorooctane sulfonate (PFOS), which is resistant to most other water treatment methods[23].

1.2.3 Cathodic oxygen reduction reaction

H_2O_2 is widely used in water treatment due to its high oxidation potential and clean product. Besides being used alone as an oxidant, H_2O_2 is also used in many advanced oxidation processes (AOPs), such as H_2O_2-Fe (the Fenton process), H_2O_2-UV, H_2O_2-O_3, as the source of ·OH[24]. Currently, H_2O_2 is industrially manufactured via the anthraquinone process, which not only requires substantial energy input, but also generates waste that requires further treatment. Moreover, because of the instability of H_2O_2, its transportation is also potentially hazardous[25]. In light of these, electrochemical 2-electron oxygen reduction reaction (ORR, Eq 3, $E^{\theta} = +0.695$ V) serves as an ideal alternative for low-cost, green, and onsite production of H_2O_2. Practically, its competitive reactions, 4-electron ORR (Eq 4, $E^{\theta} = +1.229$ V) and HER (Eq 5, $E^{\theta} = 0$ V), must also be considered.

$$O_2 + 2H^+ + 2e^- \rightleftharpoons H_2O_2 \tag{3}$$

$$O_2 + 4H^+ + 4e^- \rightleftharpoons 2H_2O \tag{4}$$

$$2H^+ + 2e^- \rightleftharpoons H_2 \tag{5}$$

Generally, given the ~0.7 V difference between the E^{θ} of 2-electron ORR and HER, HER is less recognized as a competing reaction for electrochemical H_2O_2 production, but the selectivity of 2-electron ORR over 4-electron ORR is a major concern for H_2O_2 production performance.

Similar to anodic oxidation reactions, the choice of cathode is the key for the activity and selectivity of ORR. Conventionally, noble metals showed excellent catalytic activity for ORR, and they are among the first materials to be used for electrochemical 2-electron ORR catalysis. Metals interacting weakly with O_2, including Au, Ag, and Pd, were found to successfully catalyze 2-electron ORR. 2-electron ORR on Au (111) and Au (110) facets was firstly reported back in 1983[26]. Gold nanoclusters (Au_{25}) capped by thiol ligand achieved 90% selectivity for 2-electron ORR in 0.1 M KOH medium[27]. Au-based alloys have also been extensively studied for electrochemical H_2O_2 production. The average electron transfer numbers for Au-Ni and Au-Ni-Pt catalysts in 0.1 M KOH solution were found to be 2.48 and 2.11, respectively. Notably, Au-Ni-Pt achieved a current efficiency of 95% for 2-electron ORR in 0.1 M KOH solution in the potential window of 0.45 ~ 0.55 V[28]. On the other hand, $Au_{1-x}Pd_x$ catalysts were also studied both experimentally and theoretically for 2-electron ORR. Carbon supported $Au_{0.92}Pd_{0.08}$ catalysts showed 95% current efficiency for 2-electron ORR in 0.1 M $HClO_4$ around 0 V vs. SCE. However, the selectivity was observed to drop quickly as the potential swept more negative[29]. Besides, Au_3Pd and Au_9Pd were found to catalyze 2-electron ORR at a very small overpotential, indicating their excellent activity[30].

Besides Au-based catalysts, Pd-Hg/C[31,32] and carbon-coated Pt[33] were also successfully used in 2-electron ORR catalysis. Both of them had a noble metal core and an outer shell composed of the more “inert” components. The effect of the core-shell structure was accounted for by the assumption that it may facilitate the “end-on” adsorption of O_2, which selectively favors 2-electron reduction[33].

Parallel to the noble metal catalysts are carbon-based catalysts, featuring low price, unique surface and structural properties that can be fine-tuned. Commercial carbon materials such as carbon felt and carbon black were used to catalyze 2-electron ORR[25,34,35], and researchers have developed a series of more porous carbon materials for efficient 2-electron ORR catalysis. For example, hierarchically porous carbon was synthesized by carbonizing metal organic framework (MOF), MOF-5. It achieved 80.9% ~ 95.0% selectivity for 2-electron ORR under pH 1 and 4 conditions[36].

On the other hand, heteroatoms like O and N were found to profoundly modify the catalytic behavior of carbon materials, and therefore doping of carbon materials was widely adopted as a viable strategy to enhance the catalytic activity and selectivity for 2-electron ORR. The effect of O doping on the catalytic performance of carbon nanotubes was systematically studied by Zhiyi et al. in 2018[37]. Oxygen doping was found to substantially increase the activity and selectivity (~90%) of carbon nanotubes (CNTs) towards 2-electron ORR, and carbon atoms adjacent to several dopant oxygen atoms, as in -COOH and C-O-C groups, were identified as the key catalytic sites. N-doped mesoporous carbon derived from different precursors were reported with good catalytic activity[38–41]. Graphitized N-doped single-wall carbon nanohorns were reported to achieve ~98% current efficiency towards H_2O_2 production at pH 1 condition. It is notable that the nanohorn catalyst maintained >60% FE in the pH range of 1-13[42]. Other than O and N, other dopant elements such as S and P were also shown to potentially enhance the catalytic performance of carbon materials for 2-electron ORR[43,44].

Given the excellent ORR catalytic performance, both noble-metal-based and carbon-based catalysts were used in water treatment for *in situ* electrochemical production of H_2O_2. Carbon-based cathodes are especially favored due to their low price and easy availability. Typically, the electrochemical synthesis of H_2O_2 is combined with various other “H_2O_2 activation processes”, such as UV, O_3, ultrasonication, to produce highly reactive $\cdot OH$[24].

The combination of 2-electron ORR and ozonation is often referred to as “electro-peroxone” process, where the produced H_2O_2 reacts with O_3 to generate $\cdot OH$. The mixture of O_3 and $\cdot OH$ provides powerful oxidation for the organic contaminants in wastewater. On the other hand, the reduction product of ozone reduction, O_2, also serves as the feedstock for 2-electron, which further facilitates the H_2O_2 production[45–47]. With a carbon black/PTFE cathode, electro-peroxone process removed 92% TOC from a landfill leachate concentrate in 6 h. In comparison, sole electrolysis with O_2 constantly sparged only removed 31% of the TOC in 6 h and ozonation alone removed 55% TOC. This demonstrated the potential of electro-peroxone process to treat refractory contaminants[46]. However, despite the good water treatment performance, O_3 and $\cdot OH$ may lead to the oxidation of carbon cathode over time and be detrimental for the long-term stability of the system. Therefore, a two-stage electro-peroxone system was developed, where the 2-electron ORR and reaction between H_2O_2 and O_3 took place in two separated chambers. The system was successfully used to treat synthetic greywater, reducing 89% of the TOC over 90 min[48].

Fenton process is another important H_2O_2 activation process, where Fe(II) and Fe(III) redox couple catalyze the cleavage of H_2O_2 to generate ·OH (Eq 6 and 7).

$$\mathrm{Fe^{2+} + H_2O_2 \rightleftharpoons Fe^{3+} + HO\cdot + OH^-} \tag{6}$$

$$\mathrm{Fe^{3+} + H_2O_2 \rightleftharpoons Fe^{2+} + HOO\cdot + H^+} \tag{7}$$

The conventional Fenton process relies on soluble ferrous and ferric ions in the water. When the H_2O_2 is produced by 2-electron ORR, the process is referred to as electro-Fenton (EF) process, which was demonstrated to be effective against a series of aqueous pollutants[49–51]. However, despite the good treatment performance, the Fenton process also brings substantial extra cost and operational complexity. Specifically, to keep Fe^{3+} soluble, a low pH (<4) must be maintained, and acidification is often needed for circum-neutral wastewater. The effluent is then neutralized with bases before discharge, generating undesired precipitation like $Fe(OH)_3$. It is reported that the cost associated with the treatment and disposal of the Fe sludge can take up 10~50% of the total wastewater treatment cost[52].

In this regard, heterogeneous Fenton reaction is adopted as an attractive alternative, where solid Fe catalysts replace the soluble Fe species to catalyze the activation of H_2O_2. Fe-based compounds including magnetite, ferrihydrite, hematite, goethite, akaganèite, lepidocrocite, maghemite, pyrite and pseudobrookite have all been used as heterogeneous Fenton catalysts[53]. Furthermore, the solid Fe catalysts are embedded into carbon cathodes to form heterogeneous electro-Fenton (HEF) catalysts, which directly catalyzes both 2-electron ORR and H_2O_2 activation to produce ·OH in the presence of dissolved oxygen

(DO) and an applied reduction potential. Compared to conventional Fenton process, HEF process requires no external chemical input and generates no Fe sludge in the effluent. Therefore, it has become one of the most studied branches of Fenton processes. A CNT filter functionalized with FeOCl was used for flow-through electro-Fenton process to remove aqueous tetracycline. With a flow rate of 1.5 mL min^{-1}, the electro-Fenton filter achieved 99.5% removal of 0.04 mM tetracycline from deionized (DI) water by a single pass, as well as 89% removal from tap water and 51% removal from lake water[54]. Our group also successfully developed an electrospinning-based Fe_3O_4-loaded carbon fiber cathode and metal-organic-framework-derived multi-phase porous electrocatalysts for the degradation and mineralization of pharmaceuticals and herbicides[10,55]. It is worth noting that the core-shell structure derived from pyrolysis of amino-functionalized MOF, MIL-88(Fe)-NH_2, greatly enhanced the stability of the resulted catalyst by preventing the leaching of Fe[55].

Besides Fe, many other multivalent metals such as Cr, Ce, Cu, Co, Ni, and La also showed catalytic activity for H_2O_2 activation[56], and the analogous production of $\cdot OH$ was named “Fenton-like” reactions. Carbon materials, including activated carbon[57], reduced graphene oxide (rGO)[58] and biochar[59], also showed catalytic activity towards H_2O_2 activation. Based on the versatility of carbon-based materials as cathodic catalysts, a porous carbon monolith (PCM) was developed as a “one-stop” catalyst for both 2-electron ORR and H_2O_2 activation to directly produce $\cdot OH$. It achieved ~80% removal of aqueous napropamide in the pH range of 4~10[60].

1.3 Thesis overview

This thesis consists of four major chapters.

Chapter 2 gives a comprehensive review of the recent progress in the investigation of anode catalysts for CER, and points out several feasible future research directions. The Chlorine Evolution Reaction (CER) has practical applications in the chlor-alkali industry and electrochemical wastewater treatment. Efficient, stable, and cost-effective electrodes are critical for energy efficient chlorine production, water disinfection, and wastewater treatment. These practical applications require an in-depth understanding of the catalytic mechanism of chlorine evolution, the need for lower-cost electrode materials, and improvements in electrode design at the atomic scale. We examine factors controlling activity, selectivity, and stability of alternative CER electrodes, and provide mechanistic insights for achieving improvements in performance and durability. Steric effects of crystal structure and intermetallic electron polarization provide insight for understanding and tuning the electrode activity and selectivity. Additional insight into electrode deactivation mechanisms is gained by employing model material systems under controlled conditions. Herein, we explore viable strategies for the development of more efficient noble-metal-free CER electrodes for use in a variety of practical applications.

Chapter 3 is on a mechanistic study of the active catalytic sites in crystalline $CoSb_2O_6$, a promising chlorine evolution reaction (CER) catalyst. CER is a key reaction in electrochemical oxidation (EO) water treatment. The conventional anodes based on platinum group metals (PGMs) suffer prohibitive price, which hinders the further application of the EO systems. Crystalline cobalt antimonate ($CoSb_2O_6$) was recently identified as a promising alternative to the conventional anodes due to its high catalytic activity and excellent stability in acidic media. However, its catalytic site and mechanism have not been revealed yet. This study shed light on the catalytic site in crystalline $CoSb_2O_6$ anode by using scanning electrochemical microscopy (SECM) to compare the CER catalytic activities of a series of anode samples with different Sb/Co ratios. The results showed that Sb sites served as even more active catalytic sites than the Co sites. The varied Sb/Co ratios were also linked with slightly different chemical states of each element, leading to different CER selectivity in dilute chloride solutions. Both the counterintuitively high activity of Sb sites and the varied electronic states of the elements underscored the significance of the electronic interaction between Co and Sb.

Chapter 4 describes the development of a series of 3D-printing-based monolithic HEF cathodes. Monolithic carbon materials are widely used in wastewater treatment because of their high activity for ORR catalysis, binder-free properties and earth abundance. However, these materials typically have mesoporous or even microporous structures that lead to sluggish inner mass transport. As a result, for bulky carbon monoliths, the catalysis is limited almost exclusively to the outer surface of the cathode, leading to the inner surface area being “wasted”. On the other hand, thin carbon monoliths like carbon paper are not ideal for practical application due to the low mechanical strength. Herein, various carbon lattice electrodes were fabricated form 3D-printed resin lattices to catalyze ORR and electro-Fenton reaction. The electrochemical performance was boosted by the lattice structure that favors diffusion of reactive species and electrolyte. The carbon lattice electrodes were successfully used in cathodic ORR catalysis to produce H_2O_2. The generated H_2O_2 was further converted to hydroxyl catalyzed by the embedded Fe_3O_4. It is worth noting that Grid structure carbon lattice cathodes had the highest specific H_2O_2 and hydroxyl radical production normalized to the catalysts loading, which was attributed to the better diffusion induced by the geometry. Grid carbon lattice achieved a trimethoprim degradation of 0.57 mg g^{-1} in 60 min under -0.146 V in circum-neutral Na_2SO_4 solution. This work demonstrated that 3D printing can be used to fabricate monolithic electro-Fenton cathodes with controlled morphology and porosity.

Chapter 5 describes the treatment of primary effluent and greywater by a Ni–Sb–SnO_2 reactive electrochemical membrane (REM). In 30 min, the REM removed up to 78 ± 2% COD and 94 ± 0.6% turbidity from the primary effluent. The REM had ~100% COD removal and 89 ± 4% turbidity removal from greywater, with the effluent meeting the NSF/ANSI 350 standard. When the volume was cut to about a half, the REM achieved fast removal of 93 ± 4% turbidity in 5 min. The internal cycling mode of REM was found to not only enhance the treatment performance, but also lower the energy consumption. REM showed better treatment performance and higher energy efficiency than the conventional plate-type electrode, demonstrating the importance of macroscopic electrode structure and morphology for the performance of the EO systems.

References

(1) World Health Organization. *Sanitation*. https://www.who.int/news-room/fact-sheets/detail/sanitation.

(2) United Nations. *United Nations Millennium Development Goals*. https://www.un.org/millenniumgoals/.

(3) Massoud, M. A.; Tarhini, A.; Nasr, J. A. Decentralized Approaches to Wastewater Treatment and Management: Applicability in Developing Countries. *J. Environ. Manage.* **2009**, *90* (1), 652–659. https://doi.org/10.1016/j.jenvman.2008.07.001.

(4) Geetha Varma, V.; Jha, S.; Himesh Karthik Raju, L.; Lalith Kishore, R.; Ranjith, V. A Review on Decentralized Wastewater Treatment Systems in India. *Chemosphere* **2022**, *300*, 134462. https://doi.org/10.1016/j.chemosphere.2022.134462.

(5) Hube, S.; Wu, B. Mitigation of Emerging Pollutants and Pathogens in Decentralized Wastewater Treatment Processes: A Review. *Sci. Total Environ.* **2021**, *779*, 146545. https://doi.org/10.1016/j.scitotenv.2021.146545.

(6) Yang, Y.; Shin, J.; Jasper, J. T.; Hoffmann, M. R. Multilayer Heterojunction Anodes for Saline Wastewater Treatment: Design Strategies and Reactive Species Generation Mechanisms. *Environ. Sci. Technol.* **2016**, *50* (16), 8780–8787. https://doi.org/10.1021/acs.est.6b00688.

(7) Radjenovic, J.; Sedlak, D. L. Challenges and Opportunities for Electrochemical Processes as Next-Generation Technologies for the Treatment of Contaminated Water. *Environ. Sci. Technol.* **2015**, *49* (19), 11292–11302. https://doi.org/10.1021/acs.est.5b02414.

(8) Yang, Y.; Hoffmann, M. R. Synthesis and Stabilization of Blue-Black TiO_2 Nanotube Arrays for Electrochemical Oxidant Generation and Wastewater Treatment. *Environ. Sci. Technol.* **2016**, *50* (21), 11888–11894. https://doi.org/10.1021/acs.est.6b03540.

(9) Rao, U.; Su, Y.; Khor, C. M.; Jung, B.; Ma, S.; Cwiertny, D. M.; Wong, B. M.; Jassby, D. Structural Dependence of Reductive Defluorination of Linear PFAS Compounds in a UV/Electrochemical System. *Environ. Sci. Technol.* **2020**, *54* (17), 10668–10677. https://doi.org/10.1021/acs.est.0c02773.

(10) Liu, K.; Yu, J. C.-C.; Dong, H.; Wu, J. C. S.; Hoffmann, M. R. Degradation and Mineralization of Carbamazepine Using an Electro-Fenton Reaction Catalyzed by Magnetite Nanoparticles Fixed on an Electrocatalytic Carbon Fiber Textile Cathode. *Environ. Sci. Technol.* **2018**, *52* (21), 12667–12674. https://doi.org/10.1021/acs.est.8b03916.

(11) Park, H.; Vecitis, C. D.; Hoffmann, M. R. Solar-Powered Electrochemical Oxidation of Organic Compounds Coupled with the Cathodic Production of Molecular Hydrogen. *J. Phys. Chem. A* **2008**, *112* (33), 7616–7626. https://doi.org/10.1021/jp802807e.

(12) Martínez-Huitle, C. A.; Ferro, S. Electrochemical Oxidation of Organic Pollutants for the Wastewater Treatment: Direct and Indirect Processes. *Chem. Soc. Rev.* **2006**, *35* (12), 1324–1340. https://doi.org/10.1039/B517632H.

(13) Cid, C. A.; Jasper, J. T.; Hoffmann, M. R. Phosphate Recovery from Human Waste via the Formation of Hydroxyapatite during Electrochemical Wastewater Treatment. *ACS Sustainable Chem. Eng.* **2018**, *6* (3), 3135–3142. https://doi.org/10.1021/acssuschemeng.7b03155.

(14) Mook, W. T.; Chakrabarti, M. H.; Aroua, M. K.; Khan, G. M. A.; Ali, B. S.; Islam, M. S.; Abu Hassan, M. A. Removal of Total Ammonia Nitrogen (TAN), Nitrate and Total Organic Carbon (TOC) from Aquaculture Wastewater Using Electrochemical Technology: A Review. *Desalination* **2012**, *285*, 1–13. https://doi.org/10.1016/j.desal.2011.09.029.

(15) Park, H.; Vecitis, C. D.; Choi, W.; Weres, O.; Hoffmann, M. R. Solar-Powered Production of Molecular Hydrogen from Water. *J. Phys. Chem. C* **2008**, *112* (4), 885–889. https://doi.org/10.1021/jp710723p.

(16) Park, H.; Vecitis, C. D.; Hoffmann, M. R. Electrochemical Water Splitting Coupled with Organic Compound Oxidation: The Role of Active Chlorine Species. *J. Phys. Chem. C* **2009**, *113* (18), 7935–7945. https://doi.org/10.1021/jp810331w.

(17) Jasper, J. T.; Shafaat, O. S.; Hoffmann, M. R. Electrochemical Transformation of Trace Organic Contaminants in Latrine Wastewater. *Environ. Sci. Technol.* **2016**, *50* (18), 10198–10208. https://doi.org/10.1021/acs.est.6b02912.

(18) Kim, J.; Kwon, D.; Kim, K.; Hoffmann, M. R. Electrochemical Production of Hydrogen Coupled with the Oxidation of Arsenite. *Environ. Sci. Technol.* **2014**, *48* (3), 2059–2066. https://doi.org/10.1021/es4046814.

(19) Cho, K.; Qu, Y.; Kwon, D.; Zhang, H.; Cid, C. A.; Aryanfar, A.; Hoffmann, M. R. Effects of Anodic Potential and Chloride Ion on Overall Reactivity in Electrochemical Reactors Designed for Solar-Powered Wastewater Treatment. *Environ. Sci. Technol.* **2014**, *48* (4), 2377–2384. https://doi.org/10.1021/es404137u.

(20) Huang, X.; Qu, Y.; Cid, C. A.; Finke, C.; Hoffmann, M. R.; Lim, K.; Jiang, S. C. Electrochemical Disinfection of Toilet Wastewater Using Wastewater Electrolysis Cell. *Water Res.* **2016**, *92*, 164–172. https://doi.org/10.1016/j.watres.2016.01.040.

(21) Yang, Y.; Lin, L.; Tse, L. K.; Dong, H.; Yu, S.; Hoffmann, M. R. Membrane-Separated Electrochemical Latrine Wastewater Treatment. *Environ. Sci.: Water Res. Technol.* **2019**, *5* (1), 51–59. https://doi.org/10.1039/C8EW00698A.

(22) Cho, K.; Hoffmann, M. R. Molecular Hydrogen Production from Wastewater Electrolysis Cell with Multi-Junction BiOx/TiO_2 Anode and Stainless Steel Cathode: Current and Energy Efficiency. *Appl. Catal. B.* **2017**, *202*, 671–682. https://doi.org/10.1016/j.apcatb.2016.09.067.

(23) Carter, K. E.; Farrell, J. Oxidative Destruction of Perfluorooctane Sulfonate Using Boron-Doped Diamond Film Electrodes. *Environ. Sci. Technol.* **2008**, *42* (16), 6111–6115. https://doi.org/10.1021/es703273s.

(24) Sun, M.; Chu, C.; Geng, F.; Lu, X.; Qu, J.; Crittenden, J.; Elimelech, M.; Kim, J.-H. Reinventing Fenton Chemistry: Iron Oxychloride Nanosheet for PH-Insensitive H_2O_2 Activation. *Environ. Sci. Technol. Lett.* **2018**, *5* (3), 186–191. https://doi.org/10.1021/acs.estlett.8b00065.

(25) Luo, H.; Li, C.; Wu, C.; Dong, X. In Situ Electrosynthesis of Hydrogen Peroxide with an Improved Gas Diffusion Cathode by Rolling Carbon Black and PTFE. *RSC Adv.* **2015**, *5* (80), 65227–65235. https://doi.org/10.1039/C5RA09636G.

(26) Adžić, R. R.; Tripković, A. V.; Marković, N. M. Structural Effects in Electrocatalysis: Oxidation of Formic Acid and Oxygen Reduction on Single-Crystal Electrodes and the Effects of Foreign Metal Adatoms. *J. Electroanal. Chem.* **1983**, *150* (1–2), 79–88. https://doi.org/10.1016/S0022-0728(83)80192-2.

(27) Lu, Y.; Jiang, Y.; Gao, X.; Chen, W. Charge State-Dependent Catalytic Activity of $[Au_{25}(SC_{12}H_{25})_{18}]$ Nanoclusters for the Two-Electron Reduction of Dioxygen to Hydrogen Peroxide. *Chem. Commun.* **2014**, *50* (62), 8464–8467. https://doi.org/10.1039/C4CC01841A.

(28) Zheng, Z.; Ng, Y. H.; Wang, D.-W.; Amal, R. Epitaxial Growth of Au-Pt-Ni Nanorods for Direct High Selectivity H_2O_2 Production. *Adv. Mater.* **2016**, *28* (45), 9949–9955. https://doi.org/10.1002/adma.201603662.

(29) Jirkovský, J. S.; Panas, I.; Ahlberg, E.; Halasa, M.; Romani, S.; Schiffrin, D. J. Single Atom Hot-Spots at Au–Pd Nanoalloys for Electrocatalytic H_2O_2 Production. *J. Am. Chem. Soc.* **2011**, *133* (48), 19432–19441. https://doi.org/10.1021/ja206477z.

(30) Pizzutilo, E.; Kasian, O.; Choi, C. H.; Cherevko, S.; Hutchings, G. J.; Mayrhofer, K. J. J.; Freakley, S. J. Electrocatalytic Synthesis of Hydrogen Peroxide on Au-Pd Nanoparticles: From Fundamentals to Continuous Production. *Chem. Phys. Lett.* **2017**, *683*, 436–442. https://doi.org/10.1016/j.cplett.2017.01.071.

(31) Verdaguer-Casadevall, A.; Deiana, D.; Karamad, M.; Siahrostami, S.; Malacrida, P.; Hansen, T. W.; Rossmeisl, J.; Chorkendorff, I.; Stephens, I. E. L. Trends in the Electrochemical Synthesis of H_2O_2: Enhancing Activity and Selectivity by Electrocatalytic Site Engineering. *Nano Lett.* **2014**, *14* (3), 1603–1608. https://doi.org/10.1021/nl500037x.

(32) Deiana, D.; Verdaguer-Casadevall, A.; Malacrida, P.; Stephens, I. E. L.; Chorkendorff, I.; Wagner, J. B.; Hansen, T. W. Determination of Core-Shell Structures in Pd-Hg Nanoparticles by STEM-EDX. *ChemCatChem* **2015**, *7* (22), 3748–3752. https://doi.org/10.1002/cctc.201500791.

(33) Choi, C. H.; Kwon, H. C.; Yook, S.; Shin, H.; Kim, H.; Choi, M. Hydrogen Peroxide Synthesis via Enhanced Two-Electron Oxygen Reduction Pathway on Carbon-Coated Pt Surface. *J. Phys. Chem. C* **2014**, *118* (51), 30063–30070. https://doi.org/10.1021/jp5113894.

(34) Drogui, P.; Elmaleh, S.; Rumeau, M.; Bernard, C.; Rambaud, A. Hydrogen Peroxide Production by Water Electrolysis: Application to Disinfection. *J. Appl. Electrochem.* **2001**, *31* (8), 877–882. https://doi.org/10.1023/A:1017588221369.

(35) Soltani, R. D. C.; Rezaee, A.; Khataee, A. R.; Godini, H. Electrochemical Generation of Hydrogen Peroxide Using Carbon Black-, Carbon Nanotube-, and Carbon Black/Carbon Nanotube-Coated Gas-Diffusion Cathodes: Effect of Operational Parameters and Decolorization Study. *Res. Chem. Intermed.* **2013**, *39* (9), 4277–4286. https://doi.org/10.1007/s11164-012-0944-8.

(36) Liu, Y.; Quan, X.; Fan, X.; Wang, H.; Chen, S. High-Yield Electrosynthesis of Hydrogen Peroxide from Oxygen Reduction by Hierarchically Porous Carbon. *Angew. Chem. Int. Ed.* **2015**, *54* (23), 6837–6841. https://doi.org/10.1002/anie.201502396.

(37) Lu, Z.; Chen, G.; Siahrostami, S.; Chen, Z.; Liu, K.; Xie, J.; Liao, L.; Wu, T.; Lin, D.; Liu, Y.; Jaramillo, T. F.; Nørskov, J. K.; Cui, Y. High-Efficiency Oxygen Reduction to Hydrogen Peroxide Catalysed by Oxidized Carbon Materials. *Nat. Catal.* **2018**, *1* (2), 156–162. https://doi.org/10.1038/s41929-017-0017-x.

(38) Fellinger, T.-P.; Hasché, F.; Strasser, P.; Antonietti, M. Mesoporous Nitrogen-Doped Carbon for the Electrocatalytic Synthesis of Hydrogen Peroxide. *J. Am. Chem. Soc.* **2012**, *134* (9), 4072–4075. https://doi.org/10.1021/ja300038p.

(39) Park, J.; Nabae, Y.; Hayakawa, T.; Kakimoto, M. Highly Selective Two-Electron Oxygen Reduction Catalyzed by Mesoporous Nitrogen-Doped Carbon. *ACS Catal.* **2014**, *4* (10), 3749–3754. https://doi.org/10.1021/cs5008206.

(40) Hasché, F.; Oezaslan, M.; Strasser, P.; Fellinger, T.-P. Electrocatalytic Hydrogen Peroxide Formation on Mesoporous Non-Metal Nitrogen-Doped Carbon Catalyst. *J. Energy Chem.* **2016**, *25* (2), 251–257. https://doi.org/10.1016/j.jechem.2016.01.024.

(41) Yang, Y.; He, F.; Shen, Y.; Chen, X.; Mei, H.; Liu, S.; Zhang, Y. A Biomass Derived N/C-Catalyst for the Electrochemical Production of Hydrogen Peroxide. *Chem. Commun.* **2017**, *53* (72), 9994–9997. https://doi.org/10.1039/C7CC04819J.

(42) Iglesias, D.; Giuliani, A.; Melchionna, M.; Marchesan, S.; Criado, A.; Nasi, L.; Bevilacqua, M.; Tavagnacco, C.; Vizza, F.; Prato, M.; Fornasiero, P. N-Doped Graphitized Carbon Nanohorns as a Forefront Electrocatalyst in Highly Selective O_2 Reduction to H_2O_2. *Chem* **2018**, *4* (1), 106–123. https://doi.org/10.1016/j.chempr.2017.10.013.

(43) Perazzolo, V.; Durante, C.; Pilot, R.; Paduano, A.; Zheng, J.; Rizzi, G. A.; Martucci, A.; Granozzi, G.; Gennaro, A. Nitrogen and Sulfur Doped Mesoporous Carbon as

Metal-Free Electrocatalysts for the in Situ Production of Hydrogen Peroxide. *Carbon* **2015**, *95*, 949–963. https://doi.org/10.1016/j.carbon.2015.09.002.

(44) Xia, Y.; Shang, H.; Zhang, Q.; Zhou, Y.; Hu, X. Electrogeneration of Hydrogen Peroxide Using Phosphorus-Doped Carbon Nanotubes Gas Diffusion Electrodes and Its Application in Electro-Fenton. *J. Electroanal. Chem.* **2019**, *840*, 400–408. https://doi.org/10.1016/j.jelechem.2019.04.009.

(45) Wang, H.; Mustafa, M.; Yu, G.; Östman, M.; Cheng, Y.; Wang, Y.; Tysklind, M. Oxidation of Emerging Biocides and Antibiotics in Wastewater by Ozonation and the Electro-Peroxone Process. *Chemosphere* **2019**, *235*, 575–585. https://doi.org/10.1016/j.chemosphere.2019.06.205.

(46) Li, Z.; Yuan, S.; Qiu, C.; Wang, Y.; Pan, X.; Wang, J.; Wang, C.; Zuo, J. Effective Degradation of Refractory Organic Pollutants in Landfill Leachate by Electro-Peroxone Treatment. *Electrochim. Acta* **2013**, *102*, 174–182. https://doi.org/10.1016/j.electacta.2013.04.034.

(47) Li, X.; Wang, Y.; Yuan, S.; Li, Z.; Wang, B.; Huang, J.; Deng, S.; Yu, G. Degradation of the Anti-Inflammatory Drug Ibuprofen by Electro-Peroxone Process. *Water Res.* **2014**, *63*, 81–93. https://doi.org/10.1016/j.watres.2014.06.009.

(48) Dobelle, L.; Kim, S.; LeVan, A. X.; Leandri, H.; Hoffmann, M. R.; Cid, C. A. Onsite Graywater Treatment in a Two-Stage Electro-Peroxone Reactor with a Partial Recycle of Treated Effluent. *ACS EST Eng.* **2021**, *1* (12), 1659–1667. https://doi.org/10.1021/acsestengg.1c00240.

(49) Chen, C.-Y.; Tang, C.; Wang, H.-F.; Chen, C.-M.; Zhang, X.; Huang, X.; Zhang, Q. Oxygen Reduction Reaction on Graphene in an Electro-Fenton System: In Situ Generation of H_2O_2 for the Oxidation of Organic Compounds. *ChemSusChem* **2016**, *9* (10), 1194–1199. https://doi.org/10.1002/cssc.201600030.

(50) Liu, Y.; Chen, S.; Quan, X.; Yu, H.; Zhao, H.; Zhang, Y. Efficient Mineralization of Perfluorooctanoate by Electro-Fenton with H_2O_2 Electro-Generated on Hierarchically Porous Carbon. *Environ. Sci. Technol.* **2015**, *49* (22), 13528–13533. https://doi.org/10.1021/acs.est.5b03147.

(51) Liu, M.; Feng, Z.; Luan, X.; Chu, W.; Zhao, H.; Zhao, G. Accelerated Fe^{2+} Regeneration in an Effective Electro-Fenton Process by Boosting Internal Electron

Transfer to a Nitrogen-Conjugated Fe(III) Complex. *Environ. Sci. Technol.* **2021**, *55* (9), 6042–6051. https://doi.org/10.1021/acs.est.0c08018.

(52) Munoz, M.; de Pedro, Z. M.; Casas, J. A.; Rodriguez, J. J. Preparation of Magnetite-Based Catalysts and Their Application in Heterogeneous Fenton Oxidation – A Review. *Appl. Catal. B.* **2015**, *176–177*, 249–265. https://doi.org/10.1016/j.apcatb.2015.04.003.

(53) Zhu, Y.; Zhu, R.; Xi, Y.; Zhu, J.; Zhu, G.; He, H. Strategies for Enhancing the Heterogeneous Fenton Catalytic Reactivity: A Review. *Appl. Catal. B.* **2019**, *255*, 117739. https://doi.org/10.1016/j.apcatb.2019.05.041.

(54) Li, Z.; Shen, C.; Liu, Y.; Ma, C.; Li, F.; Yang, B.; Huang, M.; Wang, Z.; Dong, L.; Wolfgang, S. Carbon Nanotube Filter Functionalized with Iron Oxychloride for Flow-through Electro-Fenton. *Appl. Catal. B.* **2020**, *260*, 118204. https://doi.org/10.1016/j.apcatb.2019.118204.

(55) Liu, K.; Yu, M.; Wang, H.; Wang, J.; Liu, W.; Hoffmann, M. R. Multiphase Porous Electrochemical Catalysts Derived from Iron-Based Metal–Organic Framework Compounds. *Environ. Sci. Technol.* **2019**, *53* (11), 6474–6482. https://doi.org/10.1021/acs.est.9b01143.

(56) Chumakov, A.; Batalova, V.; Slizhov, Y. Electro-Fenton-like Reactions of Transition Metal Ions with Electrogenerated Hydrogen Peroxide; Tomsk, Russia, 2016; p 040004. https://doi.org/10.1063/1.4964563.

(57) Anfruns, A.; García-Suárez, E. J.; Montes-Morán, M. A.; Gonzalez-Olmos, R.; Martin, M. J. New Insights into the Influence of Activated Carbon Surface Oxygen Groups on H_2O_2 Decomposition and Oxidation of Pre-Adsorbed Volatile Organic Compounds. *Carbon* **2014**, *77*, 89–98. https://doi.org/10.1016/j.carbon.2014.05.009.

(58) Lyu, L.; Yu, G.; Zhang, L.; Hu, C.; Sun, Y. 4-Phenoxyphenol-Functionalized Reduced Graphene Oxide Nanosheets: A Metal-Free Fenton-Like Catalyst for Pollutant Destruction. *Environ. Sci. Technol.* **2018**, *52* (2), 747–756. https://doi.org/10.1021/acs.est.7b04865.

(59) Fang, G.; Gao, J.; Liu, C.; Dionysiou, D. D.; Wang, Y.; Zhou, D. Key Role of Persistent Free Radicals in Hydrogen Peroxide Activation by Biochar: Implications to Organic Contaminant Degradation. *Environ. Sci. Technol.* **2014**, *48* (3), 1902–1910. https://doi.org/10.1021/es4048126.

(60) Yu, M.; Dong, H.; Liu, K.; Zheng, Y.; Hoffmann, M. R.; Liu, W. Porous Carbon Monoliths for Electrochemical Removal of Aqueous Herbicides by “One-Stop” Catalysis of Oxygen Reduction and H_2O_2 Activation. *J. Hazard. Mater.* **2021**, *414*, 125592. https://doi.org/10.1016/j.jhazmat.2021.125592.

Chapter 2 Mixed Metal Oxide Electrodes and the Chlorine Evolution Reaction: Fundamental Principles and Practical Applications

Heng Dong[1], Weilai Yu[2], and Michael R. Hoffmann[1*]

[1]Linde Laboratories and [2]Division of Chemistry and Chemical Engineering

California Institute of Technology, Pasadena, California 91125, USA

[*]Corresponding author:

Michael R. Hoffmann - mrh@caltech.edu

2.1 Abstract

The Chlorine Evolution Reaction (CER) has practical applications in the chlor-alkali industry and electrochemical wastewater treatment. Efficient, stable, and cost-effective electrodes are critical for energy efficient chlorine production, water disinfection, and wastewater treatment. These practical applications require an in-depth understanding of the catalytic mechanism of chlorine evolution, the need for lower-cost electrode materials, and improvements in electrode design at the atomic scale. Herein, we examine factors controlling activity, selectivity, and stability of alternative CER electrodes, and provide mechanistic insights for achieving improvements in performance and durability. Steric effects of crystal structure and intermetallic electron polarization provide insight for understanding and tuning the electrode activity and selectivity. Additional insight into electrode deactivation mechanisms is gained by employing model material systems under controlled conditions. Herein, we explore viable strategies for the development of more efficient noble-metal-free CER electrodes for use in a variety of practical applications.

2.2 Introduction

Chlorine gas (Cl_2) is a commodity chemical that is widely used in construction materials, plastics, organic synthesis, metallurgy, and water disinfection along with many other applications.[1] In the chlor-alkali industry, $Cl_2(g)$ is produced via the chlorine evolution reaction (CER, Equation 1) in acidic NaCl aqueous electrolyte solutions at concentrations of 200 g L^{-1} (3.42 M) NaCl in the anolyte[1]. The oxygen evolution reaction (OER, Equation 2) is a competitive side reaction. Given that 150 TWh of electricity is consumed by chlor-alkali industry per year,[2] optimization of the anodic processes can result in improved economic and environmental benefits. Seawater, a low cost source of chloride, is now considered to be an alternative electrolyte for CER.[3–5] In addition, CER plays a key role in the onsite electrochemical oxidation (EO) of wastewater in decentralized facilities.[6] In the latter case, chloride in wastewater is anodically oxidized into free reactive chlorine (Cl_2, HOCl and OCl^-), which contributes to organic matter oxidation and wastewater disinfection. In multiple practical cases, EO has been shown to be relatively efficient for the onsite treatment of household wastewater[7–11] as well as trace pharmaceutical and personal care products (PPCPs).[12]

$$2Cl^- \rightleftharpoons Cl_2 + 2e^- \tag{1}$$

$$2H_2O \rightleftharpoons O_2 + 4H^+ + 4e^- \tag{2}$$

Anode is a key for both chlor-alkali and EO systems. An ideal anode catalyzes CER with fast kinetics and high selectivity, therefore boosting the efficiency while saving the operational cost. Dimensionally stable anodes (DSAs), which often consist of a Ti base metal plate as the conductive substrate and one or more metal oxide coatings as the active electrocatalyst, are traditionally employed in the chlor-alkali industry for CER. Beer[13] proposed the use of oxides of the platinum group metals (PGMs, including Ru, Rh, Pd, Os, Ir and Pt) as the active catalyst layer. However, early generations of DSAs were often compromised by dissolution under high applied potentials and acidic conditions. The PGM oxides are also susceptible to reductive dissolution upon polarity reversal. To overcome these problems, IVB and VB group transition metals such as Ti, Ta, Nb and Zr, also known as valve metals, were used to form mixed metal oxides (MMO) to stabilize the PGM oxides. For example, RuO_2-TiO_2 (RTO) electrodes exhibited enhanced catalytic activity as well as improved stability, enabling their use in the chlor-alkali industry.[13] The performance of RTO electrodes was further improved by IrO_2 doping. Thus, the family of RuO_2-IrO_2-TiO_2 electrodes can be considered 'state-of-art' for the CER in the chlor-alkali industry and for onsite wastewater electrolysis.[14] Considering the scarcity and prohibitive price of Ru and Ir, anode stability and lifetime are directly related to the capital cost.

Optimization of MMO electrodes (e.g., RTO and RuO_2-IrO_2-TiO_2) has been explored by controlling annealing temperature,[15] elemental composition[16,17], and particle size[18]. Comninellis and Vercesi investigated the DSAs with various "PGM + valve metal" binary coatings prepared by thermal deposition procedure. Low thermal deposition yields were noticed for SnO_2 and Pt, as opposed to the almost 100% yield for IrO_2, RuO_2 and Ta_2O_5.[19] Pt-Ta_2O_5 electrode produced the largest electrochemically active surface area as quantified by integration of the cyclic voltammograms, while IrO_2-Ta_2O_5 electrode had the longest service lifetime with respect to the catalyst loading.[20] At the same time, numerous factors have been identified to influence the apparent (practical) electrode performance, including electrode morphology, porosity, catalyst loading, gas bubble formation and removal as well as electrolyte pH and composition.[21] Brian et al. studied the influence of chloride concentration on CER kinetics over Pt electrodes and concluded that the reaction kinetics were controlled by the recombination of Cl· instead of mass transfer.[22]

However, after 60 years of research, the underlying catalytic mechanism of CER on MMO electrodes remains poorly understood. Moreover, RTO and RuO_2-IrO_2-TiO_2 electrodes have lower CER selectivity in wastewater with typical chloride concentrations of ~30 mM.[6,23,24] Lower chloride concentrations often reduce electrode lifetimes as the concurrent OER compromises electrode stability.[25] For industrial applications, the use of PGMs increases capital costs and thus limits wide implementation of electrochemical technology for wastewater treatment in developing countries. In this regard, PGM-free electrodes that have high activity, long-term stability, and preferential selectivity for the CER are critical for developing practical electrochemical applications that are more efficient and economical. In order to achieve these goals, detailed mechanistic insights into CER catalysis at the atomic scale are essential. In this perspective, we focus on summarizing recent developments in the design, fabrication, and evaluation of CER anodes.

2.3 Evaluation of electrodes

The objective assessment of the performances of CER anodes requires standardized experimental protocols to properly evaluate activity, selectivity, and stability (Table 2.1). Electrochemical activity, as quantified by CER overpotential, and selectivity, as quantified by the Faradaic Efficiency (FE) or the current efficiency, need to be clearly defined. FE is defined as

$$\mathrm{FE} = \frac{Q_{\mathrm{CER}}}{Q_{\mathrm{overall}}} = \frac{\int i_{\mathrm{CER}} dt}{\int i_{\mathrm{overall}} dt} \tag{3}$$

where Q is the charge passed and I is the current at an arbitrary time = t. At lower applied potentials in a NaCl solution, OER is the only primary side reaction competing with CER, giving an FE as follows:

$$\mathrm{FE} = \frac{\int i_{\mathrm{CER}} dt}{\int i_{\mathrm{overall}} dt} \approx \frac{\int i_{\mathrm{CER}} dt}{\int (i_{\mathrm{CER}} + i_{\mathrm{OER}}) dt} \tag{4}$$

With no mass transfer limitations, the Tafel equation can be applied

$$\eta = \frac{RT}{\alpha_{\mathrm{CER}} F} ln i_{0,\mathrm{CER}} + \frac{RT}{\alpha_{\mathrm{CER}} F} ln i_{\mathrm{CER}} \tag{5}$$

where i_0 represents the exchange current, α represents the transfer coefficient, η represents overpotential and F = 96,485 C mol^{-1}. For a system with two competing reactions, Tilak et al.[26] developed an expression for FE as follows:

$$\mathrm{FE} = \frac{1}{1 + \delta \mathrm{FE}^{-\epsilon} I^{-\epsilon}} \tag{6}$$

$$\delta = \frac{i_{0,1}}{i_{0,2}} exp\ (k_2 \Delta E) i_{0,1} \epsilon \tag{7}$$

$$\epsilon = \frac{k_1 - k_2}{k_1} \tag{8}$$

The subscripts 1 and 2 in Equation 7 and 8 are the two reactions, CER and OER, and I represents the overall current density. ΔE is the difference between the Nernst potentials of the two reactions and k is the inverse of Tafel slopes for each reaction (Equation 9)

$$k = \frac{\alpha_{\mathrm{CER}} F}{RT} \tag{9}$$

Based on Equation 5-9, the kinetics of the CER are reflected in both the overpotential and the Faradaic Efficiency. However, the FE also includes the kinetics of OER. Thus, activity and selectivity should not be used interchangeably.

Table 2.1. Key aspects and caveats in evaluating the overall performance of CER anodes.

Aspects	**Caveats**	**Refs**
Activity (overpotential)	Qualitative techniques: CV&LSV	29-34
	Concentrated, acidified chloride solution to suppress OER	27, 28
	Quantitative techniques: Tafel plots	29, 35-38
	Gaseous Cl_2 saturation for Nernstian potential calculation	39
Selectivity (Faradaic efficiency)	Gaseous Cl_2 & O_2 detection: DEMS, OLEMS	27, 37, 42, 43
	Aqueous Cl_2 detection: DPD reagent, iodometry	6, 23, 32
	Different Cl^- concentrations correspond to different applications	23, 27
Stability (service lifetime)	NaCl, $KClO_4$, H_2SO_4 and $HClO_4$ often used for ALT	6, 15, 32, 51-54, 57-59,
	CV and EIS coupled with ALT to understand deactivation mechanism	15, 51-58
	Chronoamperometry may be helpful for understanding the deterioration of catalytic sites	55
	Well-controlled nanoparticles used to unravel the intrinsic degradation of pure metal oxides	55

2.3.1 Activity evaluation

Overpotential plays a key role in the screening of anodes for use in the traditional chlor-alkali industry. For measurements of electrode activity or overpotential, increasing the

CER selectivity is essential to minimize interference due to competition with the OER. This can be achieved by increasing the chloride concentration and acidifying the electrolyte[2s7,28]. However, the FE of the CER often drops below 50% in circum-neutral dilute chloride solutions such as found in wastewater.[6,23] Therefore, quantifying electrode selectivity under the conditions related to wastewater is essential for evaluating the performance of an electrode for practical environmental applications.

$$E = E^{\theta} + \frac{RT}{2F} ln \frac{a(Cl_2)}{a(Cl^-)^2} \tag{10}$$

In practice, it is challenging to determine the overpotential of the CER due to the difficulty of determining the Nernst potential (Equation 10) due to a constantly changing chloride activity and chlorine fugacity (i.e., evolution of Cl_2 vs. time) during an electrochemical reaction. Therefore, potential sweeping techniques such as cyclic voltammetry (CV) and linear sweep voltammetry (LSV) are often used as convenient ways to compare the overpotential of CER anodes.[29–34] Although these methods are easy to implement, it is often difficult to compare results between different studies, since the reported results are sensitive to various experimental factors, including electrolyte composition, electrochemical setup, and scan rate. To overcome these limitations, polarization curves and Tafel plots obtained using steady-state chronoamperometry (CA) or quasi-steady potential sweeping methods at low scan rates[29,35–38] are often used for electrode evaluation and inter-comparison. Analogously, chronopotentiometry (CP) was also employed to compare the overpotential of electrodes at a fixed current density[39,40] which is more convenient but gives less kinetic insights compared to Tafel analysis.

To calculate the CER overpotential of a given electrode, the thermodynamic equilibrium potential of CER under standard-state conditions must be subtracted from the data obtained from the Tafel plots. The thermodynamic potential of the CER has been measured by Sohrabnejad-Eskan et al.,[37] and Finke et al.[39] In one study,[37] the equilibrium CER potential was estimated by extrapolating the polarization curve to yield an approximate thermodynamic potential value of 1.26 V in a 5 M NaCl solution adjusted to pH = 2. On the other hand, Finke et al.,[39] determined the thermodynamic equilibrium potential of CER by pre-saturating a 5 M NaCl solution with 1.0 atm $Cl_2(g)$ while controlling the pH at 2. Under these conditions, a thermodynamic potential was determined as 1.288 V at 25 °C. In the scenario of CP measurements, a concentrated NaCl electrolyte minimized the competition from OER and changes in the thermodynamic equilibrium potential of CER caused by the continuous consumption of chloride ion. Saturation of the electrolyte with $Cl_2(g)$ also allows for the free chlorine fugacity to remain constant during the reaction, thereby allowing for a more reliable and precise determination of the actual thermodynamic potential.

2.3.2 Selectivity evaluation

Selectivity, as reflected by the FE, is often evaluated by measuring the ratio of anodically generated $Cl_2(g)$ to that of $O_2(g)$ or by comparing the generated $Cl_2(g)$ to the total charge passed. Given the 2-electron nature of the CER as opposed to the 4-electron OER, selectivity is influenced by the kinetics of both reactions at electrode surface.[1]

Chronopotentiometry is most often used for determination of selectivity.[5,6,23,40,41] The production rate of dissolved Cl_2 in solution is determined using traditional analytical methods that using N,N-diethyl-p-phenylenediamine (DPD)[6,23,32] colorimetry or iodometry.[40] The production rate of $Cl_2(g)$ in gas-phase can be determined using differential electrochemical mass spectroscopy (DEMS)[27,42,43] or online electrochemical mass spectrometry (OLEMS),[37] where $O_2(g)$ can be analyzed in parallel. It is worth noting that the formed chlorine is usually quantified by HCl signal (m/z = 36 or 38) in mass spectrometers due to the easy breakage of Cl-Cl bond.[37] Considering the evaporation from acidified chloride solution, the signal should be carefully calibrated. Due to the moderate solubility of Cl_2 in water given a Henry's law constant of 9.5×10^{-2} M atm^{-1} at 25 ˚C[44], the partitioning of Cl_2 between the aqueous and gaseous phases must be taken into account when determining the overall selectivity between Cl_2 and O_2. For example, a faster rate of the CER leads to a more rapid saturation of Cl_2 in the aqueous phase coupled with a fairly large fraction of Cl_2 released into the gaseous phase. On the other hand, if the CER proceeds at a slower rate, a larger fraction of the evolved Cl_2 will remain in the aqueous electrolyte.

Based on Henry's law considerations, the release of $Cl_2(g)$ from acidic solution into gas phase is expected to occur regardless of its aqueous-phase concentration. However, the water-to-air gas transfer can be relatively slow depending on the concentration gradient near the water-air interface as well as the turbulence within the reactor. Similar concerns are relevant for large-scale CER applications. The apparent Faradaic Efficiencies obtained from measuring only the aqueous-phase Cl_2 concentration could be considered sufficient for anode evaluation. However, it should also be noted that the partitioning of Cl_2 into the gas phase matters in practical applications (e.g., the chlor-alkali industry or municipal water disinfection). Thus, the partitioning of Cl_2 between the gaseous and aqueous phases should be considered in calculating the electrode selectivity. Furthermore, the selectivity measurement is also influenced by a variety of experimental parameters including electrolysis time, applied current, and total electrolyte volume. As a consequence, aqueous-phase measurements are preferred in cases involving dilute chloride solutions with short electrolysis times and low currents,[23] while gas-phase measurements are more suitable when concentrated chloride solutions with longer electrolysis times and larger applied currents are employed.[27]

The electrochemically generated chlorine may also be lost due to further anodic oxidation to chlorate (Equation 11). Different stoichiometries have been proposed by Kuhn and Mortimer,[45] Rius and Llopis,[46] and Jasper et al.,[9] respectively. Although this reaction is valuable for chlorate production, it results in not only parasitic oxygen release in industrial chlorine production, but also chlorate formed as a toxic by-product in water treatment.[6,9] The reaction is especially significant at relatively high temperature (e.g. 70 ° C) and low chloride activity.[45] For measurement of CER selectivity, formation of chlorate consumes a fraction of chlorine but adds to the oxygen production, leading to underestimation of CER selectivity. Rotating ring-disk electrodes (RRDE) can be employed to mitigate the interference since it prevents the further contact of formed ClO^- with the anode.[47] However, it is worth noting that since this reaction is inevitable under most hydraulic conditions, evaluating the “chlorate formation corrected” CER selectivity is still sensible for practical applications.

$$aClO^- + bH_2O \rightleftharpoons cClO_3^- + dCl^- + xH^+ + yO_2 + ze^- \qquad (11)$$

Even though quantifying chlorine in only one phase may be sufficient for a rough comparison between different CER anodes, this approach will result in an underestimation of the chlorine production rate and the FE. Thus, to accurately determine the FE of CER for a given electrode formulation, measurements in both aqueous and gaseous phases should be made simultaneously to access the total yield of Cl_2 (e.g., $\{Cl_2\}_T = \{Cl_2\}_{aq} + \{Cl_2\}_g$). Uncontrolled losses in the quantification of total chlorine activity, $\{Cl_2\}_T$, is likely to account for some of the discrepancies in reported FEs.[32,48]

Apparent electrode selectivity is impacted by numerous factors other than the intrinsic properties of a specific electrode. In addition to the different electron transfer numbers and chloride concentrations, another pronounced difference lies in the different pH-dependent kinetics of the CER and OER (Equation 1 and 2). Acidification has been widely used to increase CER selectivity in chlor-alkali industry.[1] This approach is also useful in tests of CER activity of electrodes to minimize the interference from the OER.[39,40] In addition, anions such as F^-, SO_4^{2-}, NO_3^-, PO_4^{3-} are also know to affect CER selectivity most likely due competitive surface binding.[1] In particular, bidentate ligands have been shown to bind strongly to RTO electrode surfaces leading to a lower CER selectivity[1], while F^- deactivates RTO electrodes by forming TiF_6^{2-},[49,50] or more likely, by replacement of surface hydroxy sites, >TiOH and >RuOH, with >TiF and >RuF, where " > " denotes a specific surface binding site. Thus, competitive surface complexation by F^- and HSO_4^-, SO_4^{2-} can block key surficial binding sites (e.g., >RuOH), for Cl^- substitution. Furthermore, formation of radicals such as $Cl_2^{\cdot -}$, ·OH, and $HO_2\cdot$ are usually neglected in calculation of the FE due to their low steady-state concentrations, in spite of their important role in oxidative wastewater treatment.

2.3.3 Stability evaluation

Considering the high cost of PGMs like Ir and Ru, conventional MMO electrodes require sufficiently high catalytic activities, high FE's, and long service lifetimes to be economically feasible for practical application. Oxidative dissolution and the growth of an insulating interlayer between the substrate and active catalyst layer are the two main deactivation mechanisms for MMO-type electrodes.[14] Since conventional DSAs need to have lifetimes on the order of years, the stability of anodes is most often estimated using accelerated life tests (ALT). In a typical ALT, anodes are tested using chronopotentiometry under at high current densities in very acidic electrolytes.[15,51–55] Electrode lifetime is estimated by the amount of time taken for the applied potential to exhibit a sharp increase, or to increase to a set value. Other techniques such as CV and electrochemical impedance spectroscopy (EIS) are also used along with ALT to monitor the changes in the electrochemical properties of electrode during long-term tests.[15,51–58] Methods used for material characterization include scanning electron microscopy (SEM),[53,54] X-ray diffraction (XRD)[15,54], and X-ray photoelectron (XPS)[55] to reveal microstructural and compositional changes after the electrochemical tests.

NaCl solutions are traditionally used as the electrolyte to simulate the working conditions of chlor-alkali industry.[51,58] As the dissolution of PGMs has been shown to be closely correlated with the OER, sulfuric acid and perchloric acid are often used as electrolytes with concentration ranging from 0.1 N to 2 N.[15,51–54,57,59] Perchlorate solutions are often used in environmental studies to better estimate electrode lifetimes in wastewater media.[6,32] However, given the complicated electrolyte composition, the actual service lifetimes of electrodes used in wastewater treatment may vary substantially from the estimated lifetime by ALT. For example, organic compounds such as CH_3OH, HCHO and HCOOH at concentrations as high as 0.5 M have been shown to substantially reduce the service lifetime of Ir-Ta electrodes in Na_2SO_4 solutions.[60] These results indicate that different deactivation mechanisms are likely to co-exist for aqueous-phase species traditionally considered as unimportant in terms of CER electrode lifetime, even though the chlorine radical species may react with a wide array of organic and inorganic species in surface water, groundwater water, or wastewater. Thus, in order to fully understand the stability of electrodes in wastewater, it is necessary to fundamentally unravel the effects of different solutes as they may impact the deactivation of electrodes.

In the absence of an accepted protocol to conveniently and rapidly screen electrodes, the time-intensive ALT methods of DSA-type electrodes provide a limited insight into the properties of surface catalytic sites (e.g., valence state, stoichiometry, and crystallinity) during the electrode dissolution. This is most likely due to the inhomogeneity of electrodes prepared by brush or spray coating techniques. Moreover, the loss of electrode activity may be due to a reduction in conductivity, electrochemically-active surface area (ECSA), or electrode-specific activity as measured in terms of catalytic activity per surface area.

Although changes in electrode conductivity can be characterized using EIS, the conventional ALT protocol, even when coupled with CV and other characterization techniques, often fails to distinguish between the loss of ECSA and a decrease in specific activity.

To overcome inhomogeneity issues, several model electrodes based on well-defined nanostructures or nanoparticles of iridium oxide have been studied to understand its deactivation mechanism for the OER. For example, Tan et al.[55] combined LSV, Tafel plots, and EIS to monitor the activity of the IrO_2 anodes over time, while the dissolved Ir species in the aqueous solution were measured by inductively coupled plasma mass spectrometry (ICP-MS). Amorphous IrO_x was found to have a higher catalytic activity, but lower stability compared with crystalline-phase IrO_2. Tan et al.[55] proposed a mechanism for Ir(III) dissolution to explain this apparent discrepancy. The deactivation of highly crystalline IrO_2 was attributed to the loss in specific activity of the catalytic sites, whereas the deactivation of amorphous IrO_x was due to the dissolution and loss of ECSA. In their study, the current density per geometric surface area was taken as the apparent catalytic activity summed over all catalytic sites. ECSA was determined by integral of the CV voltammograms to monitor the changes in the number of catalytic active sites. Specific activity was then quantified using the current density normalized to ECSA as determined by intermittent chronoamperometry experiments over the course of electrode deactivation. In this way, the decrease in the number of active sites and the deterioration of each site was uncoupled by the loss in ECSA and the decrease in specific activity, respectively. However, constant potential conditions were required by this approach to reasonably compare the specific activities. In conventional ALT protocols, the loss of ECSA usually leads to an increasing potential, which accelerates the changes in the specific activity of the catalytic sites.

ICP-MS measurements are used with ALT to monitor the real-time ionic leaching from electrode surfaces. However, detection and quantification of gaseous corrosion products such as RuO_4(g) requires the use of online GC-MS. Electrochemical quartz crystal microbalance (EQCM) weight measurements versus time provide an alternative method to monitor dissolution of thin-film electrodes under electrochemical conditions.[61–63] EQCM has been used to investigate the dissolution of various metal oxides used for the OER.[64–66]

Extending EQCM to research on the CER could provide additional mechanistic insight in to electrode stability under controlled operating conditions.

2.4 Activity & selectivity

Various experimental factors, including electrolyte pH and composition, specific adsorption of ions, bubble formation and removal and passivation of the substrate, can influence the catalytic CER kinetics. Early study on these factors has been comprehensively reviewed by Trasatti.[21] With the advancement of fabrication and characterization techniques, more attention has been redirected onto screening next-generation electrode materials with high intrinsic chemical properties, and Sabatier principle has played an important role in connecting the material properties with CER catalytic performance.[67] According to the Sabatier principle, the adsorption energy of reactive species near catalyst surfaces should be optimized to allow for facile sorption of the substrate and equally facile desorption of the product. This principle leads to the "volcano plot" relationship between catalytic activity and the surface properties of heterogenous catalysts (Figure 2.1).[68] As mentioned above, the oxides of the PGMs are found near the apex of a volcano plot with RuO_2 serving as the benchmark for the CER[69,70] although IrO_2, PtO_2 and CoO_x are also considered to be suitable CER catalysts.[1]

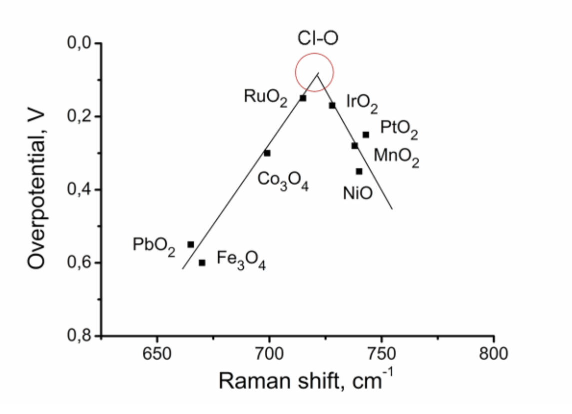

Figure 2.1. Volcano plot for CER catalysis reproduced with permission from Zeradjanin et al.[68] Copyright 2012 WILEY-VCH Verlag GmbH & Co. KGaA, Weinheim.

The CER activity of the MMO electrodes primarily relies on the use of PGMs, although Ru is most used. The effect of various metal ion dopants on the catalytic performance of RuO_2 has been reviewed by Karlsson and Cornell.[1] The metal dopants can be categorized into: (1) valve metals (e.g. Ti, Zr, Ta and Sn);[5,34,36,43,68,71–77] (2) non-valve first-row transition metals (Zn, Co, Ni, Zn);[26,42,78–85] and (3) other metals such as Ce and Mg.[36,86] Iridium, which is more expensive than Ru, is often used as a dopant to prolong the service lifetime of the other PGM oxides.[13,73,87–91] Valve metals are traditionally viewed as intrinsically inactive electrode stabilizers that are used solely for increasing electrode lifetimes. However, this argument has been challenged by the enhanced activities exhibited by Ti- or Sn-containing electrodes that enhance the CER selectivity of RuO_2.[26,77] In the case of RTO electrodes prepared by thermal deposition using homogenous precursor solutions, Ti has been shown by Rutherford backscattering spectrometry and XPS to preferentially segregate at the electrode surface to “cover” Ru sites.[92] Moreover, Tafel plots were used to show that a RTO electrode made with 35 wt% RuO_2 had a similar CER activity as an electrode made with 80 wt% RuO_2.[16] This result implies that Ti (e.g., >TiOH) also functions as catalytically active sites on the surface of RTO electrodes.

Transition metals such as Fe, Co and Ni can be incorporated into the rutile lattice of RuO_2 to form a single-phase mixture,[42,78,79,82,84] although Co and Ni dopants form new phases at high annealing temperatures.[72,74] At an atomic percentage of <20%, cobalt forms a single-phase binary nanocrystalline catalyst with RuO_2 with a mean size of 20-60 nm that results in both enhanced OER activity and increased selectivity.[84] Iron was shown to increase the OER activity and while suppressing the CER.[78] Nickel was shown to be enriched at the surface upon doping into the rutile RuO_2 matrix without forming a distinct phase.[80] This resulted in an increase in both the CER selectivity and activity. The optimal CER selectivity was achieved at 10% Ni doping, whereas the highest activity was observed at 20% Ni doping for both CER and OER.[42] In contrast, doping RuO_2 with Zn and Mg formed local ilmenite structures intergrow with rutile blocks that resulted in reduction in current density in chloride electrolyte solutions.[85,86] In addition, the CER selectivity of RuO_2 decreased with Zn doping,[83] while selectivity was increased with Mg doping.[86]

IrO_2 has a higher CER selectivity than RuO_2 in dilute chloride solutions despite its lower activity, as shown by Kuhn and Motimer.[45] Contradictive result was reported by Vos and Koper using RRDE.[47] The discrepancy was partly caused by the static solution and high temperature (70 °C) used by Kuhn and Motimer that facilitate chlorate formation. On the other hand, the differences were also attributed to the different catalyst fabrication methods. The electrochemical generation of chlorine species over RuO_2 and IrO_2 electrodes was further examined by Yoon et al.[93] under constant current condition at room temperature. Higher rates of both free chlorine and chlorate production were observed for RuO_2 in dilute chloride solution. Based on the above results, it is speculated that RuO_2 had higher CER selectivity than IrO_2, but also higher catalytic activity for hypochlorite oxidation. Therefore, IrO_2 may show higher effective CER selectivity under the condition of high temperature and hypochlorite concentration.

Ir-doping causes a shift in the selectivity of RuO_2 electrodes towards the CER.[94] Given that RuO_2 and IrO_2 with the same rutile structure and similar lattice parameters, their different electrocatalytic selectivity may be attributed to differences in electronic properties. In spite of the differences between RuO_2 and IrO_2 electrodes, iridium oxides have been used for the CER.[47,48,95] In addition to bimetallic electrodes, electrodes containing three or more elements have also been developed in efforts to enhance electrode performance.[5,74] For example, a ternary RuO_2–IrO_2–TiO_2 electrode has been shown to have both enhanced activity and improved stability.[14] However, the detailed catalytic mechanisms of ternary electrodes are poorly characterized.

The Sabatier principle also provides a semi-empirical strategy for tuning the activity of CER active anodes. For example, an ideal CER electrode should have “just right” affinity for chloride to be located at the apex of the Sabatier volcano, while the opposite should be expected for the OER in order have an electrode with high activity and selectivity for the CER. However, this may be challenging to achieve in practice considering the dynamic nature of the catalyst surface, as influenced by applied potential, solution pH, the formation of surface hydroxy groups (e.g., $>MOH^{2+}$, $>MOH$, and $>MO^{-}$) on hydrated surfaces, and the presence of competitive adsorbates or complexing ligands at electrode surface.[70,96] As illustrated by the DFT calculations of Hansen et al., further complication arise due to the intertwining of the mechanisms for the OER and CER (Figure 2.2).[70]

Modulating the affinity toward surfaces of the target reactants and resulting products with on electrode surfaces may allow for higher efficiency CER catalysis by tuning the surface properties of the electrodes, by changing either steric or electronic factors. Steric factors include surface morphology, lattice structure, and the potential stacking of catalytically active sites. The electronic factors include the intrinsic electronic properties of each catalytic site as reflected in the time-dependent valence states, surface charges, and surface potentials.

In terms of steric factors, the influence of surface morphology of Ru-based electrodes on their CER and OER activities has been investigated. For example, Zeradjanin et al.[27] attributed improved performance of an RTO electrode in concentrated NaCl solutions to larger microscopic "cracks" as revealed by SEM, which were thought to lead to enhanced mass transport of both reactants to and products away from the active surface sites.[27] Their observations were supported by the results of Trieu et al.,[97] who emphasized the importance of accessible "outer surface area" for electrode activity. In a related study, microscopic cracks were introduced into RuO_2 by Sn doping in order to enhance OER catalytic activity by facilitating gas bubble detachment.[98] Lower Ru leaching under the same applied potential profile was observed in the study as well. Chen et al. had contradictive argument that $Ru_{0.3}Sn_{0.7}O_2$ electrodes with "mud-crack" morphology had compromised stability because of the electrolyte penetrating the cracks to oxidize the Ti substrate, based on the L-edge XAS spectra.[99] However, control experiments with compact-morphology samples are needed to solidify the conclusion. They also reported comparable CER activity of crack-free electrodes compared to the "mud-crack" ones. The discrepancy in activity in the two studies might be due to the different techniques used. High-performance CER catalysis has been achieved using "superaerophobic" nanoarray-structured RTO electrodes that repelled gas bubbles and had fast product detachment.[34] In contrast, lowered CER selectivity and a decrease in overall activity with Zn-doped RuO_2 was attributed to the formation of inclusions ilmenite-like structures.[83,85]

Modification of catalytic surfaces at the nano or atomic scale is limited by available fabrication methods and a lack of understanding the mechanistic details of the CER. On the other hand, there appears to be a relationship between CER catalytic activity and the rutile crystal structure, as shown in the cases of RuO_2, IrO_2, PtO_2, RTO, and RuO_2-IrO_2-TiO_2 anodes. In addition to the PGM-based anodes, a series of transition metal antimonate catalysts with rutile structures ($MSbO_x$, M = Ni, Co, Mn) have been shown to have high activity and stability for both the OER and CER in acidic electrolytes.[40,100] These results suggest that the crystal structures and crystalline facets may have an intrinsic influence on CER catalysis. For example, the different crystal facets of RuO_2 have substantially different OER catalytic activities.[101] Additional experimental and computational studies need to be focused on resolving the effects of both crystal structure and specific crystalline facet for catalysts that have polymorphs such as PbO_2 and MnO_2.

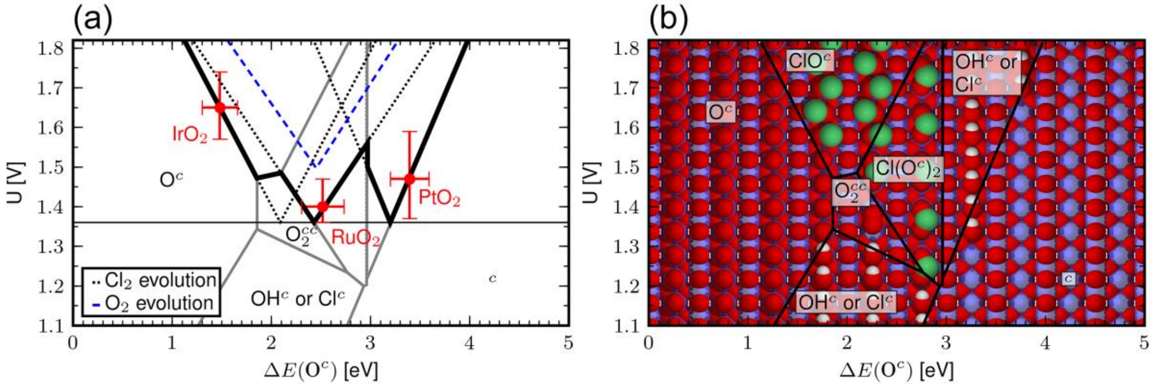

Figure 2.2. Computational diagrams of different intermediate species of the CER over the rutile (110) surface. (a) Computational Sabatier volcano plots for CER and OER catalysis over the rutile (110) facet adapted with permission from the PCCP Owner Societies from Hansen et al.[70] Copyright 2010 Royal Society of Chemistry. Black dotted lines denote the overpotential as a function of material descriptor $\Delta E(O^c)$ for CER mediated by ClO^c, $Cl(O^c)_2$ and Cl^c (from left to right), while dashed blue lines marked the calculated volcano plot for OER. The domains of the most stable surface structure as function of potential and oxygen binding energy (details shown in (b)) is marked by gray. To be truly active, the intermediate should form at sites that are stable, as this makes the active site abundant. The solid black line shows the combined Sabatier volcano taking into account the stability of the active sites for a given mechanism. The activity of IrO_2 and

RuO_2 are indicated with error bars derived from the variation of the O^c adsorption energy with varying O^c coverage.

In comparison to steric factor, modification of the electronic valance state of the catalytic sites may lead to an improved mechanistic understanding of the catalytic activity for both the PGM oxides and MMO electrodes. It was noted as early as in 1980 by Mozota et al. that cyclic-voltammetry-treated Ir and Ru electrodes showed substantially higher CER catalytic activity.[102] The authors speculated that it was due to a change in oxidation state of surface Ir and Ru atoms. XPS analyses together with DFT calculations suggest that the higher OER catalytic activity of amorphous hydrous IrO_x is due to the existence of Ir(III/IV) mixed valence states compared to rutile IrO_2.[103] Furthermore, the activity of RTO electrodes has been correlated with valence change of metals as studied by Finke et al.[39] via atomic layer deposition (ALD) and by Näslund et al.[104] via scanning electrochemical microscopy (SECM), respectively. In both studies, the authors attributed the higher observed electrochemical activity of RTO electrodes compared to pure RuO_2 to decreases in the XPS binding energy (BE) of Ti 2p states (Figure 2.3). These results suggested the presence of a partially reduced Ti state within the binary RTO matrix. Also, an increase in the BE of Ru 3d as observed by Näslund et al., implied a more oxidized state of Ru that resulted from electron polarization within the "$RuO_x^{\delta+}$-$TiO_x^{\delta-}$" matrix that in turn could account for the enhanced activity of RTO electrodes. Näslund et al., favored $RuO_x^{\delta+}$ as the catalytically active site, while Finke et al., favored $TiO_x^{\delta-}$ as the primary catalytically active site. Negative shifts in the BE of the XPS peak for TiO_x in the Ti-Ir mixture were observed by Finke et al.[39], while Yang et al,[6] indicated that the electronic interaction of the metals may contribute to the catalytic activity of conventional DSAs. The aforementioned electronic interaction indicate that Ti plays a more active role in CER catalysis than simply serving as an inactive stabilizer in MMO electrodes. Although TiO_2 is a wide band-gap semiconductor with low conductivity in its normal state, when it is partially reduced to a lower valence state (e.g. Ti^{3+}) it becomes an active CER and OER.[23,105] Photochemical studies also show similar effects are achieved by doping aliovalent atoms in to the TiO_2 lattice (Figure 2.4).[106] It is quite clear both electrochemically and photochemically that

$TiO_x^{\delta-}$ serves as an active catalytic center. Partially reduced Ti as induced by doping rather than by chemical reduction, also leads to improved electrode stability. Valence tuning as observed for Ti has also been observed for Sn and Nb oxides that are doped with Ru, Sb or N (Figure 2.3) in the TiO_2 structure.[107–109]

Although well-known and extensively used in photocatalysis, the strategy of valence tuning should be further explored in electrochemistry. Questions that remain to be answered include: 1) does partially reduced TiO_x really serve as an active site in RTO electrodes; 2) can other non-PGM elements also lead to the partial reduction of TiO_x; and 3) does valence tuning activate other valve metals for CER catalysis. Activating valve metals by valence tuning may be a promising route for future developments of CER electrodes with increased stability as well as reduced electrode costs.

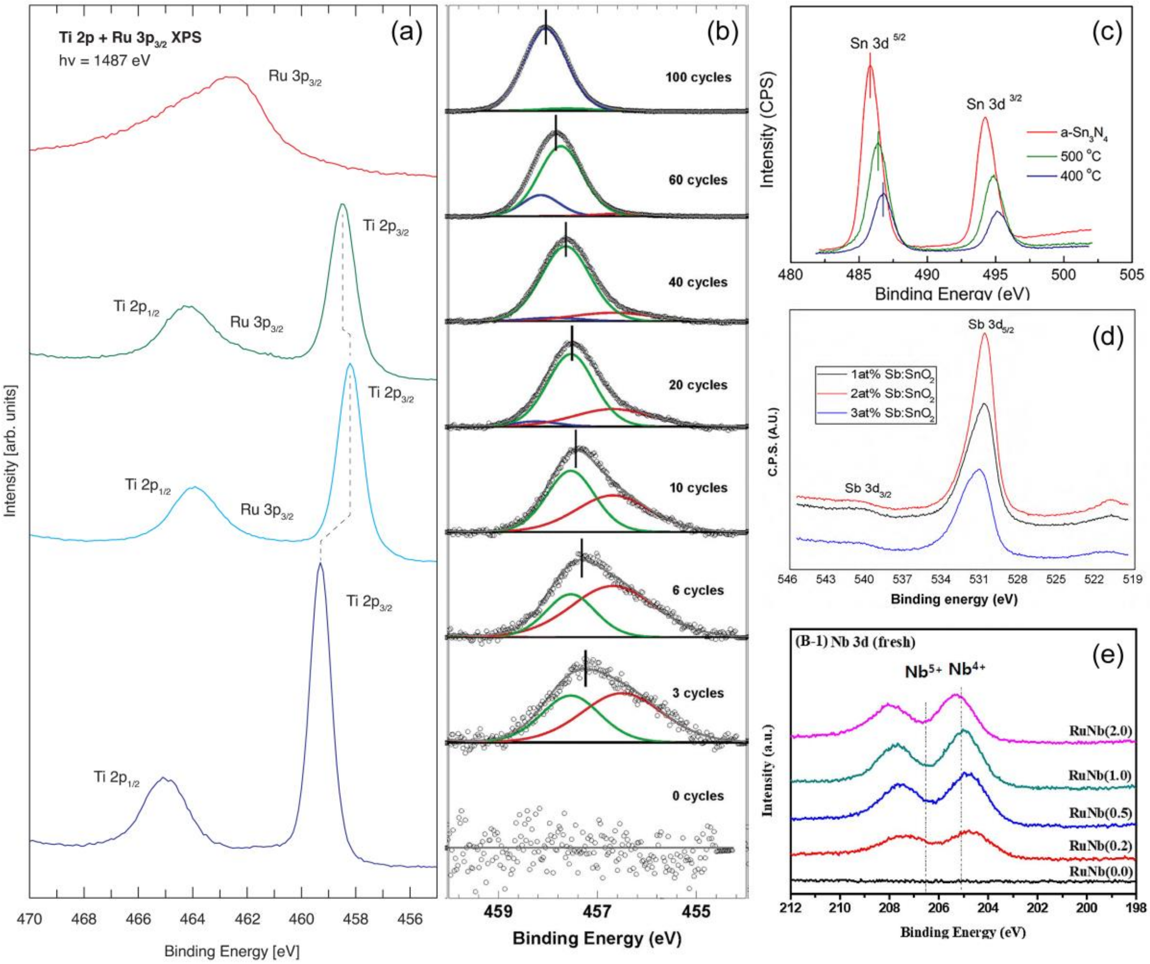

Figure 2.3. XPS spectra of valence-tuned valve metals. (a) Ti 2p XPS peak displacement after Ru doping adapted from Näslund et al.[104] Copyright 2013 American Chemical Society. The XPS spectra correspond to pure RuO_2, $Ru_{0.5}Ti_{0.5}O_2$, $Ru_{0.3}Ti_{0.7}O_2$ and pure TiO_2 from top to bottom. (b) Ti 2p XPS peak evolution during TiO_2 ALD on RuO_2 surface adapted from Finke et al.[39] Copyright 2019 Royal Society of Chemistry. Deposited TiO_2 with low cycle numbers had core-level peaks agreeing to that of Ti^{3+}, while 100-cycle TiO_2 produced XPS signal of bulk TiO_2. This clearly showed that the valence tuning effect of TiO_2 is limited to a certain range. (c) Sn 3d XPS spectra of Sn_3N_4 and N-doped SnO_2 prepared by annealing Sn_3N_4 at different temperatures adapted from Pan et al.[107] Copyright 2012 Springer. N doping led to significant Sn 3d peak shift towards low BE. (d) XPS spectra of SnO_2 doped with different levels of Sb adapted from Babar et al.[108] Copyright 2010 Elsevier. Sb doping led to shift of Sn 3d XPS peaks towards high BE. (e) Nb 3d XPS spectra of Ru-Nb/Al_2O_3 catalysts adapted from Jeon et al.[109] Copyright 2018 Elsevier. Numbers in the parentheses refer to different Nb/Ru molar ratios.

Developing new CER catalysts with both improved activity and selectivity requires an in-depth understanding of the CER catalytic mechanism. Given the limited number of *in situ* spectroscopic tools for probing reaction intermediates, DFT calculations can be a useful guiding tool for understanding catalytic processes at the atomic level. Most often, the computational studies of the CER have focused primarily on rutile systems, especially on RuO_2. The classical CER mechanisms based on kinetic studies, include the Volmer-Tafel mechanism:

$$2* + 2Cl^- \rightarrow 2Cl^* + 2e^- \tag{12}$$

$$2Cl^* \rightarrow 2* + Cl_2 \tag{13}$$

the Volmer-Heyrovsky mechanism:

$$* + Cl^- \rightarrow Cl^* + e^- \tag{14}$$

$$Cl^* + Cl^- \rightarrow * + Cl_2 + e^- \tag{15}$$

and the Krishtalik mechanism:

$$* + Cl^- \rightarrow Cl^* + e^- \tag{16}$$

$$Cl^* \rightarrow Cl^{*+} + e^- \tag{17}$$

$$Cl^{*+} + Cl^- \rightarrow * + Cl_2 \tag{18}$$

where * denotes an active catalytic site, which can be either a surface bound oxygen atom or a metal atom. The Volmer-Tafel mechanism consists of the initial binding of active sites with aqueous chloride (Equation 12, 14 and 16, denoted as the Volmer step) followed by combination of two adjacent adsorbed chlorine atoms into molecular chlorine (Equation 13, denoted as the Tafel step). The Volmer–Heyrovsky mechanism consists of a similar Volmer step but invokes consecutive adsorption of another Cl^- and release of Cl_2 (Equation 15, which is known as Heyrovsky step). The Krishtalik mechanism differs from Volmer-Heyrovsky mechanism in the adsorption of the second chloride, while the Volmer-Heyrovsky mechanism assumes a concomitant electron transfer. Only one active site is needed for either the Volmer-Heyrovsky or the Krishtalik mechanisms while two active sites are required for the Volmer-Tafel mechanism.

Even though the above mechanisms provide simple two or three elementary reaction pathways for the CER, they do not explicitly define the specific nature of the active catalytic sites. DFT calculations were first applied to the study of the catalytic oxidation of HCl in gas-phase (i.e., the Deacon process) to provide a fundamental basis to interpret experimental results in light of a sequence of elementary steps.[110,111] Hansen et al. used DFT calculations to investigate the room-temperature aqueous phase CER over the (110) facet of the rutile phases of RuO_2 and IrO_2.[70] Surface Pourbaix diagrams of RuO_2 (110) and IrO_2 (110) were constructed based on the adsorption free energies of the various possible reaction intermediates. The formation energy of surface oxygen, $\Delta E(O^c)$ was proposed as a universal "descriptor" because of its linear relationship with to the different chlorine-containing intermediates, where the superscript (^{c}) denotes a coordinatively unsaturated site (CUS). Hansen et al. established the ground work for a series of follow-up investigations that improved the thermodynamic computational results by considering the effects of the solvent,[112] bridging lattice oxygen atoms,[113] overpotential,[114] and the uncertainties involved in DFT calculations.[96]

It should be emphasized that the use of a specific descriptor, such as $\Delta E(O^c)$, significantly generalizes the calculational results leading to identification of different CER mechanisms based on the computed values of $\Delta E(O^c)$. According to Hansen et al.,[70] Sumaria et al.[96] and Exner et al.,[113] the Volmer-Heyrovsky mechanism was identified as the favored CER mechanism over the rutile (110) surfaces of RuO_2, IrO_2, TiO_2, SnO_2, PtO_2 and RhO_2. The reaction intermediates varied in the order of $ClO^c \rightarrow Cl(O^c)_2 \rightarrow Cl^c$ with increasing $\Delta E(O^c)$. Thus, the CER is predicted to be mediated by the ClO^c species on IrO_2 and RuO_2 and by Cl^c on TiO_2 under the conditions of T = 298.15 K, pH = 0, and $a_{Cl^-} = 1$.[70,115] Karlsson et al., also used thermodynamic calculations to shed light on the activity and selectivity of rutile-structured RTO electrodes.[115] $\Delta E(O^c)$ of TiO_2 was found to decrease with Ru doping, which lowered the thermodynamic energy barrier for the CER, thus enhancing CER activity. Furthermore, the shift of the $\Delta E(O^c)$ also resulted in a higher thermodynamic barrier for the OER than for the CER by 0.4 eV resulting in an enhanced CER selectivity. On the other hand, $\Delta E(O^c)$ of RuO_2 was changed slightly upon Ti doping. The computational study by Karlsson et al. suggests that TiO_x in RTO electrodes functions as catalytic active centers. Exner et al.[116] found that coating of a TiO_2 monolayer on top of RuO_2 lowered the formation energy of the ClO^c intermediate, but raised the formation energy for OER intermediate OOH^c. These two opposing effects enhanced both the catalytic activity and selectivity of the CER.[116] The conclusions above rely on the assumption that the energy barriers for CER and OER are well represented by the ΔG^0_f of the ClO^c and OOH^c intermediates, which are, in turn, linearly related to $\mathit{\Delta}E(O^c)$. Even though the Brønsted−Evans−Polanyi principle argues that activation energy barriers are linearly related to the corresponding reaction enthalpies, Exner et al. stated that this principle only applies to the Volmer step in the CER, and that the overall energy barrier, as dictated by kinetic energy barrier of Heyrovsky step, may be inversely related to the free energy of ClO^c.[117] However, postulation of a reaction mechanisms based thermodynamic calculations, may lead to large uncertainties in the prediction of catalytic activity as pointed out by Sumaria et al.[96] Besides the uncertainties caused by DFT calculation itself, lack of knowledge about the pre-exponential factor in Arrhenius equation may be another contributor to the large error in kinetics computation.[118] Thus, further kinetic studies are needed to fully understand the activity and selectivity of CER electrodes. It should also be noted that hydrolysis of surface >M-O-M< sites into >MOH[112,119,120] and the amphoteric behavior of the >MOH sites also leads to the protonated and deprotonated surface species $>MOH^{2+}$ and $>MO^-$. These important surface sites in aqueous electrochemistry are often overlooked or ignored in computational studies. In addition, as pointed out by Ooka et al., there are also various other important factors that current DFT calculations have failed to fully account for, including the influence of electrolyte, crystal defects, mass transfer and possibly charged reaction intermediates.[67] All of these contribute to the gap between computational and experiments.

Relatively few studies have been focused exclusively on the CER selectivity of MMO electrodes. Most studies about chlor-alkali process employ high chloride activities and low pH, which leads to conditions for a highly selective CER. Other non-OER O_2-contributing reactions have also been identified.[1] These factors make CER selectivity over OER not very interesting under chlor-alkali conditions. However, it is impractical to manipulate either pH or $\{Cl^-\}$ in water or wastewater treatment applications. Typical chloride concentration are ~30 mM in domestic wastewater with pH ranging from 6 to 8.[6] Thus for onsite wastewater treatment applications, CER selectivity plays a crucial role in determining performance and energy efficiency. Similar limitations are present in the case of electrochemical surface water treatment. CER selectivity is also a key parameter in seawater electrolysis for Cl_2 production considering that the average pH of seawater is8.3) with lower $[Cl^-] = 0.5$ M than employed in the chlor-alkali industry.

The competitive mechanisms underlying the CER and OER present challenges for developing CER-selective electrodes for use given the conditions encountered wastewater and sea water. In this regard, several experimental efforts to tune the CER selectivity have been made by doping of RuO_2 or IrO_2. Cu, Ni, and Mg doping were shown to increase CER selectivity of RuO_2.[42,86,121] The effects of Cu doping were attributed to the reduction in binding energy of OER-related intermediates (e.g., HO^c, O^c, HOO^c), resulting in larger OER overpotentials.[121] However. the effects of Ni and Mg doping are not fully understood. Ni doping enhances the CER selectivity of IrO_2, while Co and Zn doping shift the selectivity towards OER.[122]

Multi-layer electrodes containing an $Ir_{0.7}Ta_{0.3}O_x$ active layer coupled with mixed metal oxide coatings of Sn, Bi, Ti and Co oxides have been developed for electrochemical water and wastewater treatment, trace organic contaminant remediation, and for the oxidation of the toxic form of arsenic, arsenite, to arsenate.[6,7,9–12,32,123,124] The coated MMO electrodes were shown to have a higher CER selectivity compared to uncoated $Ir_{0.7}Ta_{0.3}O_x$ electrodes.[6,32]

An atomically dispersed Pt-N4 catalyst doped on to carbon nanotubes was reported to have both a higher CER activity and better selectivity compared to commercially available DSA electrodes.[125] The Pt-N4 catalyst maintained a CER selectivity > 95% in a pH neutral 0.1 M NaCl electrolyte. The high selectivity was ascribed to the active role of the intermediate Cl^c instead of the more commonly identified ClO^c intermediate for IrO_2 and RuO_2. In spite of the high activity and selectivity of Pt-N4 on CNTs, practical applications may be limited due to the small particle size of the Pt-N4/CNT hybrid material and concerns over its long-term stability.

DFT calculations and $\Delta E(O^c)$ values as a material descriptor should be used to provide insight for rationally designing CER-selective electrodes. Based on the different slopes of CER and OER volcano plots, a $\Delta E(O^c)$ of ~ 3.2 eV appears to be a critical point that produces the largest difference in the thermodynamic barrier between the OER and CER and thus result in the highest CER selectivity as discussed by Karlsson et al.[115] On the other hand, Exner[119] proposed that ($\Delta E(OOH^c)$ - $\Delta E(ClO^c)$) provides another useful material descriptor for screening of materials for CER selectivity and electrode stability. Of course, other factors including steric effects, crystal defects, and crystalline imperfections may also be key factors. Therefore, an improved understanding of the catalytic mechanism leading to the CER is crucial step toward future developments of CER-selective anodes.

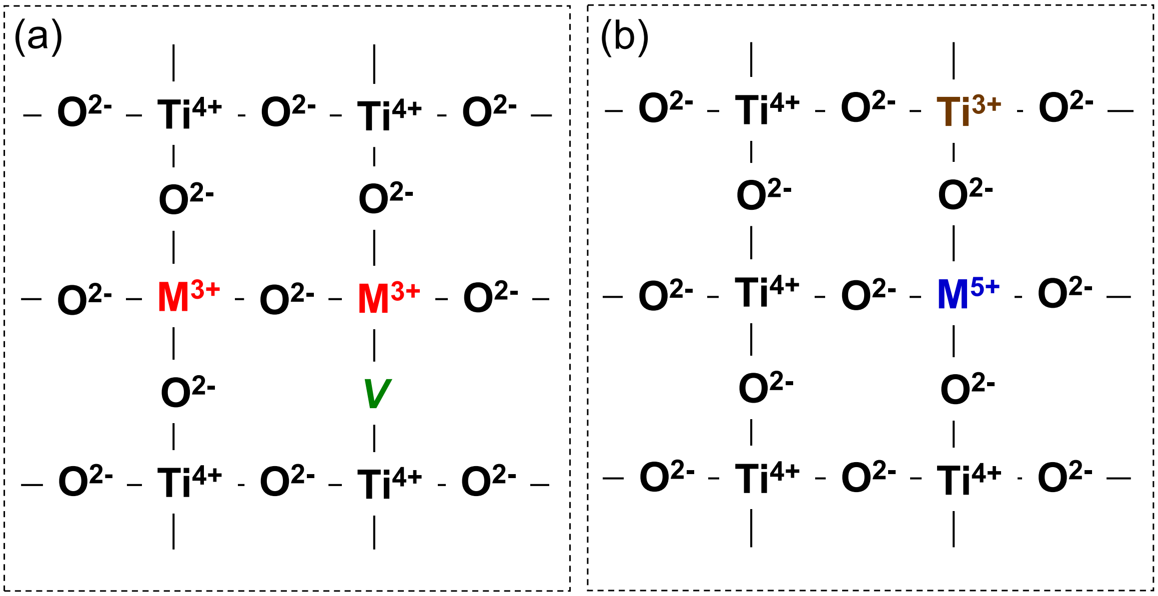

Figure 2.4. Schematic illustration of influence of aliovalent metal dopants on the TiO_2, adapted from Takata and Domen.[106] Copyright 2009 American Chemical Society. It is generally believed that to maintain charge neutrality, (a) lower-valence dopants induce oxygen vacancies while (b) higher-valence dopants induce reduced Ti^{3+} species.

2.5 Surface chemistry of CER on RuO_2, IrO_2, RTO, and other MMO electrodes

As mentioned above, despite that computational studies have identified the catalytic sites of rutile RuO_2 systems for CER, there is still a gap from experimental results since the catalyst surface properties have not been considered. Metal oxides such as TiO_2 form surface hydroxy groups upon exposure to water or humid air.[126–128] The same basic surface chemistry also applies to the hydration of RuO_2, IrO_2, and SnO_2.[129–132]

Surface ‘titanol’ groups (>TiOH) are formed upon exposure of anhydrous TiO_2 to water or humid air. Analogous hydrolysis reactions for SiO_2 or Al_2O_3 result in the formation of surface silanol ((>SiOH) and aluminol (>AlOH). Surface titanol groups, >TiOH, have surface concentrations ranging from 3 and 6 hydroxyl groups per nm^2,[133] up to a total of 17 groups per nm^2.[134–138]

Surface titanium hydroxy groups are amphoteric in that the >TiOH surface groups undergo protonation and deprotonation depending on pH. A hydrated TiO_2 surface has four distinctly identifiable surface species that include $>TiOH_2^+$, >TiOH, and $>TiO^-$ and bridging >Ti-O-Ti< groups. In water, these primary surface species dominate surface charges compared to oxygen or cation vacancies. The balancing of charges on the TiO_2 surface is established when $[>TiOH_2^+]_s = [>TiO^-]_s$. The charge-balanced state is experimentally determined by measurement of the “pH of zero point of charge” (pH_{zpc}) or by determination of the “iso-electric point” (IEP).[135,139] The pH_{zpc} is the experimentally-determined pH at which the activity of the positively charged titanol groups $\{>TiOH_2^+\}$ is balanced by the activity of negatively charged group $\{>TiO^-\}$. This equivalency leads to a net zero surface charge that is approximately equal to what is obtained at the isoelectric point.[139] Adsorption of organic or inorganic ligands (e.g., Cl^-) to TiO_2 thus occurs in part via inner-sphere ligand substitution of surface hydroxy groups (e.g., >TiOH) as a function of pH.[140,141] Inner-sphere coordination of formate and acetate on TiO_2 over the pH range of 3 to 9 on the rutile (110) surface has been fully characterized.[142]

The surface adsorption of formate and acetate on rutile is analogous to the formation of a metal-ligand complexes in aqueous solution via a conventional ligand substitution reaction:

$$> \mathrm{TiOH} + \mathrm{HCOOH} \rightleftharpoons \mathrm{TiO_2CH} + \mathrm{H_2O} \tag{19}$$

$$> \mathrm{TiOH} + \mathrm{HCO_2^-} \rightleftharpoons \mathrm{TiO_2CH} + \mathrm{OH^-} \quad (20)$$

The surface chemistries of MMO electrodes are dominated by their corresponding surface hydroxy groups (e.g., $>$RuOH + Cl^- + H^+ $\rightleftharpoons$ $>$RuCl + H_2O; $>$IrOH + Cl^- + H^+ $\rightleftharpoons$ IrCl + H_2O; and $>$TiOH + Cl^- + H^+ $\rightleftharpoons$ $>$TiCl + H_2O). The pH_{zpc} or IEP values for TiO_2, IrO_2, and RuO_2 in the rutile phases are 5.8, 3.0, and 5.8, respectively.[130–132,143] Kleijn and Lyklema reported that the pH_{zpc} of colloidal RuO_2 was 5.75 in a KNO_3 solution, while the IEP was determined to occur at pH 5.8.[131,132] However, in KCl solutions, the pH_{zpc} and the IEP shifted to higher and lower values, respectively. This shift was attributed to the specific adsorption (i.e., surface complexation) of Cl^-.[132]

Given constraints imposed by the pH_{zpc} or IEP values, the primary surface species at pH < 3 for RuO_2 and IrO_2 in an aqueous electrolyte (e.g., NaCl) will be $>RuOH_2^+$, $>$RuOH, $>IrOH_2^+$ and $>$IrOH. In light of the strong evidence for Cl^- adsorption via ligand substitution, a more detailed CER mechanism than that given by the legacy mechanisms of Equation 12-18 should take place at specific surface sites as follows in the case of RuO_2:

$$> \mathrm{RuOH_2^+} \rightleftharpoons\, > \mathrm{RuOH} + \mathrm{H^+}\ (\mathrm{pK_{a1,surf}}) \quad (21)$$

$$> \mathrm{RuOH} \rightleftharpoons\, > \mathrm{RuO^-} + \mathrm{H^+}\ (\mathrm{pK_{a2,surf}}) \quad (22)$$

where the $pH_{zpc} = (pK_{a1,surf} + pK_{a2,surf})/2$. Thus, for RuO_2 and IrO_2, the net zero charge surfaces are given defined by $pH_{zpc} = 5.75$ and $pH_{zpc} = 3.0$, respectively. Thus, in an NaCl electrolyte, the following CER surface reactions will take place at an applied potential (E_{app}) or by UV irradiation at energies greater than the band gap, E_g, which is 2.7 eV for hydrous RuO_2:

$$> \mathrm{Ru^{IV}OH_2^+} + \mathrm{Cl^-} \rightleftharpoons\, > \mathrm{Ru^{IV}Cl} + \mathrm{H_2O} \quad (23)$$

$$> \mathrm{Ru^{IV}OH} + \mathrm{Cl^-} + \mathrm{H^+} \rightleftharpoons\, > \mathrm{Ru^{IV}Cl} + \mathrm{H_2O} \quad (24)$$

$$> \mathrm{Ru^{IV}Cl} + \mathrm{H_2O} + \mathrm{E_{app}} \rightleftharpoons\, > \mathrm{Ru^{III}OH_2} + \mathrm{Cl}\cdot \quad (25)$$

$$\mathrm{Cl}\cdot + \mathrm{Cl^-} \rightleftharpoons \mathrm{Cl_2^{\cdot-}} \quad (26)$$

$$2\mathrm{Cl}\cdot \rightleftharpoons \mathrm{Cl_2} \quad (27)$$

$$> \mathrm{Ru^{IV}OH} + \mathrm{Cl_2^{\cdot-}} \rightleftharpoons\, > \mathrm{Ru^{III}OH^-} + \mathrm{Cl_2} \quad (28)$$

$$2 > \mathrm{Ru^{III}OH^-} + \mathrm{E_{app}} \rightleftharpoons 2 > \mathrm{Ru^{IV}OH} \quad (29)$$

$$2 > \mathrm{Ru^{IV}OH} + 2\mathrm{H^+} \rightleftharpoons\ 2 > \mathrm{Ru^{IV}OH_2^+} \tag{30}$$

For two adjacent hydroxylated surface sites under an applied potential, E_{app},

$$2 > \mathrm{Ru^{IV}Cl} + 2\mathrm{H_2O} + \mathrm{E_{app}} \rightleftharpoons\ 2 > \mathrm{Ru^{IV}OH_2} + \mathrm{Cl_2} \tag{31}$$

$$2 > \mathrm{Ru^{III}OH_2} + \mathrm{E_{app}} \rightleftharpoons\ 2 > \mathrm{Ru^{IV}OH_2^+} \tag{32}$$

Additional CER pathways may also involve ion pair formation close to the positively charged surfaces at pH < 3, coupled with a high concentration of Cl^- within the electrical double layer (EDL). In this case, surface bound hydroxyl radical is generated by the first electron transfer step in OER.

$$> \mathrm{Ru^{IV}OH_2^+} + \mathrm{Cl^-} \rightleftharpoons > \mathrm{Ru^{IV}OH_2^+ : Cl^-} \tag{33}$$

$$> \mathrm{Ru^{IV}OH} + \mathrm{E_{app}} \rightleftharpoons > \mathrm{Ru^{IV}OH} \cdot \tag{34}$$

$$> \mathrm{Ru^{IV}OH} \cdot +\ \mathrm{H_2O} \rightleftharpoons > \mathrm{Ru^{IV}OH_2} + \cdot \mathrm{OH} \tag{35}$$

$$> \mathrm{Ru^{IV}OH_2^+ : Cl^-} + \cdot \mathrm{OH} \rightleftharpoons > \mathrm{Ru^{IV}OH_2^+} + \mathrm{Cl} \cdot + \mathrm{OH^-} \tag{36}$$

A similar sequence of reactions will take place on each metal oxide surface of an MMO anode or on the surface of an individual metal oxide. In addition to the alternative CER mechanism proposed herein, we must also consider the total charge on anode surface, the surface potential under a given applied potential, and the ionic strength of the electrolyte. These factors will affect the thickness or shape of the EDL and near anode surface concentration of chloride relative to its bulk water phase concentration. Equation 23 is a ligand substitution reaction involving the surface complexation of Cl^- and the displacement of water from the specific surface site $>RuOH_2^+$. This initial step in the CER mechanism can be described in terms of the following equilibrium constant for a charged RuO_2 surface reaction with a complexing ligand:

$$K_{\mathrm{app}}^{\mathrm{S}} = K_{\mathrm{int}}^{\mathrm{S}} exp\ (-F\Psi/RT) \tag{37}$$

where K^s_{app} and K^s_{int} are the apparent and intrinsic constants for complexation of Cl^- at a protonated surface 'rutinol' site (i.e., $>RuOH + H^+ \rightleftharpoons >RuOH_2^+$). This equation arises from a consideration of the total ΔG^o for formation of the surface complex, which takes into account both the chemical and electrical contributions to the total complexation/sorption energy (e.g., $\Delta G^o_{tot} = \Delta G^o_{int} + \Delta G^o_{coul}$) where ΔG^o_{int} is the chemical term and ΔG^o_{coul} is the electrostatic or coulombic term. This can be expressed as follows:

$$\Delta G^{\mathrm{o}}_{\mathrm{tot}} = \Delta G^{\mathrm{o}}_{\mathrm{int}} + \Delta zF\Psi \tag{38}$$

where Ψ is the surface potential and Δz is the change in charge of the surface complex species. Identical treatments apply to the surface acidity constants (e.g., pK^{s}_{a1} and pK^{s}_{a2}, *vide supra*) and each subsequent step in the above reaction mechanism. Detailed treatments of metal oxide surface complexation and sorption thermodynamics have been presented by Stumm and Morgan,[144] Dzombak and Morel,[145] Schindler and Stumm,[146] Rodriquez et al.[147] and Faust et al.[148]

2.6 Stability of CER catalysts

Deactivation of conventional DSA's such as the MMO, RTO, RuO_2-IrO_2-TiO_2 anodes, involves dissolution of the PGM elements and growth of insulating TiO_2 layers between the catalytic coating and Ti substrate.[14] Similar deactivation mechanism was also found for OER in proton exchange membrane electrolyzers, and it is important to learn both processes to gain mechanistic insights into electrode stability.[149] Dissolution of Ru and Ir is predicted given the predictions of the corresponding Pourbaix diagrams at pH < 2. For example, RuO_2 and IrO_2 under typical applied potentials for the chlor-alkali or electrochemical oxidation processes at pH < 2 are likely to form RuO_4 and IrO_4^-, respectively.[150] Both Ir(VIII) and Ru(VIII) oxides are highly unstable. The electrochemically oxidized amorphous oxides are reported to have substantially higher dissolution rates compared to their crystalline counterparts. However, some of the amorphous oxides have been shown to have higher OER catalytic activities.[55,59,151] For example, the dissolution of RuO_2 was found to be transformed into $RuO_2(OH)_2$ and $RuO_3(OH)$ before forming RuO_4. Amorphous hydrated oxides including $RuO_2(OH)$ and $RuO_2(OH)_2$ were identified as reaction intermediates in the OER.[152] In a similar fashion, $IrO_2(OH)$ is predicted to form on the surface of IrO_2. $Ir^{V}O_2(OH)$ forms $Ir^{III}(OH)_3$ at low applied potentials and $Ir^{VI}O_3$ at high applied potentials.[153] Additionally, Ir(V)- Ir(III) and Ir(V)-Ir(VI) were identified as two distinct pathways for Ir dissolution, both of which contributed to the OER catalytic activity.[154] Analogously, crystal defects of Pt electrodes were also reported to have higher catalytic activity.[155] However, in the case of crystalline RuO_2, the OER catalytic activity of different crystalline facets did not establish a clear correlation between catalytic activity and stability.[101] This again highlighted the necessity of unraveling the influence of crystal facets for the overall CER catalytic performance of MMO electrodes beyond pure RuO_2 electrodes. In addition to OER-related dissolution under constant potential conditions, transient dissolution triggered by electrochemical modification of the Ru valence state also leads to dissolution of Ru even when the applied potential is lower than the OER potential.[151]

High chloride activity and low pH conditions favor the CER and they also extend anode lifetimes by suppressing the OER. However, the lifetime of electrodes in low ionic strength and circum-neutral pH wastewater can be impacted by more favorable conditions for the OER. On the other hand, the evolution of anode selectivity during deactivation is unclear for either the RuO_2/IrO_2 or MMO anodes. For example, the deactivation of IrO_x may involve the deterioration of IrO_x surface sites even before their dissolution as suggested by Tan et al.[55] The loss of catalytic activity may be due to changes in the surface crystalline structure and the extent of surface hydroxylation, which may also influence CER selectivity. Experimentally, the evolution in selectivity over time can be monitored over time using an RRDE[47] or DEMS.[42,43]

The stability of the PGM oxides is enhanced by mixing in acid-resistive valve metals including Ti, Zr, Nb, Ta, and Sn.[156] The valve metals also influence the deactivation mechanism of electrodes. The deactivation of conventional MMO anodes begins with dissolution of surface active Ru or Ir, followed by the electrolyte or the products penetrating the coating layer to reach the Ti base metal.[14] Furthermore, electrode fabrication using thermal deposition methods also complicates the deactivation process by forming microscopically inhomogeneous surfaces, which allows for the electrolyte to penetrate via surface cracks and then through the deposited MMO layers. At the same time, deactivation of catalytic sites and loss of specific activity may accompany the dissolution of active components (loss of ECSA) as pointed out by Tan et al.[55] For example, the dissolution of Ru reduces the intensity of localized electron polarization effects such as $RuO_x^{\delta+}$-$TiO_x^{\delta-}$ and further decreases the electrode activity, which has rarely been studied so far. Along with the loss of ECSA, future research should focus more closely on the evolution of catalytic sites during the electrode deactivation process. In addition, the adhesion of $Cl_2(g)$ bubbles has been shown to lead to a gradual delamination of deposited thin-film catalysts resulting in a reduction in electrode stability. Nano-structuring of electrode surfaces can serve as an effective strategy for modulating electrode surface affinity for Cl_2(g) bubbles.[34]

2.7 PGM-free CER electrodes

High prices and limited availability of the PGMs constrains their use in large-scale applications as electrodes. Therefore, alternative electrode materials are being explored for use in CER catalysis (Figure 2.5). Suitable metals have been used primarily as dopants to enhance the performance of the PGM-based electrodes. Consequently, PGM-free electrodes are rarely used on a large scale due to either their instability or lower catalytic activity. For example, Co-based catalysts have shown moderate activity despite concerns over their stability due to anodic dissolution. In the past, Co_3O_4 was used as an active catalytic layer in chlor-alkali industry due to its high selectivity for CER.[1,157] However, Co_3O_4 nanobelt array electrodes that were synthesized by hydrothermal methods have been shown to have a comparable catalytic CER activity to that of RuO_2. With respect to the OER, Co_3O_4 in KOH solutions is reported to be a good catalyst.[158] The surprising performance of Co_3O_4 nanobelt array electrode is attributed to its nanobelt morphology and its high surface area.[159] In addition to suitable catalytic activity, improved stability was observed for the Co_3O_4 nanobelt array electrodes compared to pure RuO_2 electrodes in side-by side chronoamperometry tests. While the Co-N-C electrodes were stable for at least 30 days at 1.2 V vs. RHE in 5 M HCl, additional performance benchmarks are needed to compare it with the state-of-art RTO or RuO_2-IrO_2-TiO_2 ternary oxide electrodes. Lead oxide (PbO_2) has also been used for CER catalysis, but it is limited by high overpotentials and the reductive leaching of Pb^{2+} ions under open circuit conditions.[160–162]

Antimonates have been shown to inhibit the anodic dissolution of Co, Ni and Mn oxides in acidic solutions.[40,100] Antimonate catalysts have been synthesized by co-sputtering of metal alloys followed by thermal oxidation to produce crystalline $CoSb_2O_x$ and $MnSb_2O_x$, which more stable than RTO electrodes for CER in acidified and concentrated NaCl solutions in spite of their higher overpotentials.[40] Other antimonates have also been used as acid-stable OER catalysts.[100] Thus, it appears possible to stabilize the catalytically active metals (e.g., Co, Mn, Ni) through the formation of stable crystalline phases by alloying with other elements like Sb. However, given its altered composition and lattice structure, the catalytic mechanism of antimonate catalysts may differ from that of pure CoO_x. In the case of amorphous $CoSb_2O_6$[163], formation of Co(IV) sites and oxygen vacancies appear to be responsible for the OER catalytic activity However, formation of oxygen vacancies were not observed in crystalline $CoSb_2O_6$.

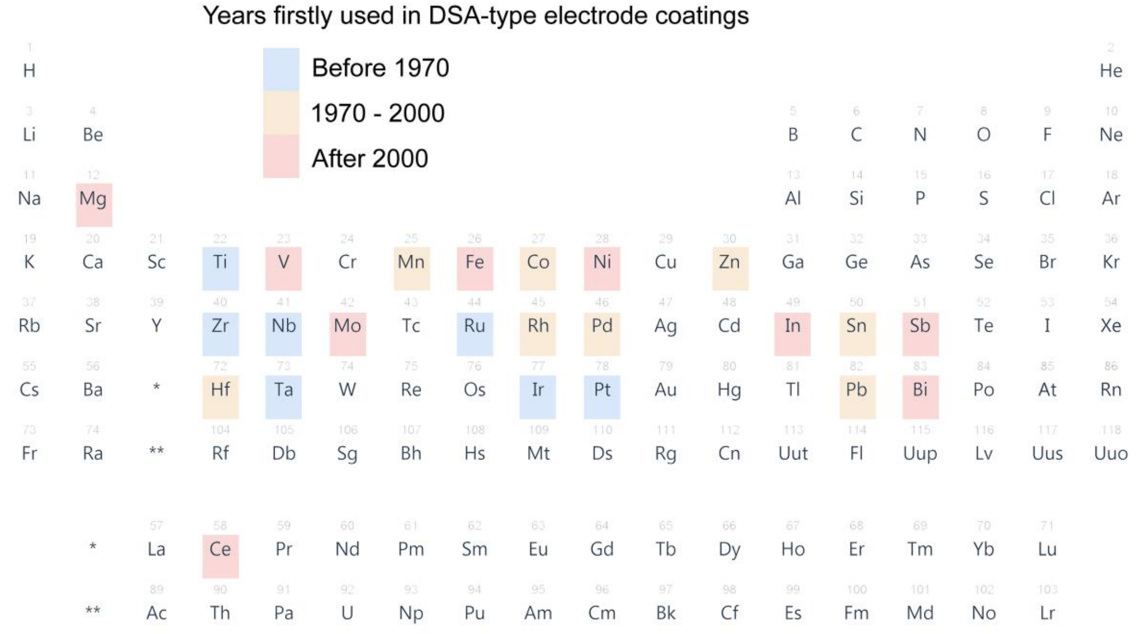

Figure 2.5. Timeframes for the use of metals in DSA electrodes for CER catalysis.

Defective TiO_x nanotubes have also been used for CER catalysis.[23,105] The TiO_2 nanotubes are prepared by anodization of Ti-metal sheets or Ti-metal foil in a fluoride electrolyte. Oxygen vacancies and $Ti^{+(4-x)}$ species are introduced into the TiO_2 lattice by either electrochemical cathodization or thermal hydrogen reduction. The reduced Ti-nanotube array electrodes have been shown to have comparable CER selectivity with commercially available DSAs. The anodic stability of reduced TiO_2 is substantially improved by selective Co^{3+} doping[105] or by a spray pyrolysis deposition of a thin TiO_2 "superficial skin" layer.[23]

The rational design of novel PGM-free catalysts remains a challenge due to a poor understanding of the detailed CER mechanism for non-rutile systems. For the non-PGM catalysts studied so far, the multivalent capability of Co and the non-stoichiometric nature of Ti(IV)/Ti(III) nanotubes have presented an additional challenge to resolve the catalytic CER and OER mechanisms over a broad range of pH. Computational chemistry should be focused on transition metal antimonate systems in order to validate the applicability of $\Delta E(O^c)$ as an appropriate material descriptor for the synthesis of PGM-free DSAs.

2.8 Future outlook

The wide application of CER in chlor-alkali industry and for electrochemical water and wastewater treatment should motivate further development of alternative anodes that are active, selective, and stable for CER catalysis. Cross-comparison between different studies requires evaluation of CER catalytic performance with a consistent set of testing conditions. Quantitative evaluation of CER activity, as characterized by overpotential, requires Tafel analyses under CER-favorable conditions such as those presented by concentrated and highly acidic chloride solutions. Saturating the electrolyte with chlorine gas is necessary for a stable thermodynamic CER potential determination. Moreover, accurate measurements of CER selectivity, as characterized by FE, require quantification of all produced chlorine species in both the gaseous and aqueous phases. Even though ALT procedures have been extensively used to estimate the lifetime of CER anodes, a detailed characterization of the evolution of catalytic sites over electrolysis timeframes are needed to unravel the deactivation mechanisms of MMO electrodes.

To develop more efficient and stable CER anodes, herein we propose that future study focus on the following aspects:

1) Resolving the effects of both crystal structure and specific crystalline facet for performance of catalysts that have multiple polymorphs, such as PbO_2 and MnO_2.
2) Understanding the catalytic sites in RTO electrodes and the effects of "$RuO_x^{\delta+}$-$TiO_x^{\delta-}$" electron polarization and extrapolating the model to other valve metals.

3) Studying the deterioration of catalytic sites and loss of specific activity during the deactivation of MMO electrodes, especially with the electron polarization effects in consideration.
4) Extending the computational chemistry method from rutile RuO_2 to trirutile transition metal antimonate systems to unveil their catalytic sites.

Despite the knowledge about catalytic sites, further comprehension of CER kinetics requires development of *in situ* material characterization techniques and more sophisticated computational models that take into account solvent environment, charged catalyst surface, crystal defects and mass transport.

2.9 Acknowledgements

The authors acknowledge generous financial support from Bill and Melinda Gates Foundation (Grant No. INV003227).

References

(1) Karlsson, R. K. B.; Cornell, A. Selectivity between Oxygen and Chlorine Evolution in the Chlor-Alkali and Chlorate Processes. *Chem. Rev.* **2016**, *116* (5), 2982–3028. https://doi.org/10.1021/acs.chemrev.5b00389.

(2) Chadwick, S. S. *Ullmann's Encyclopedia of Industrial Chemistry*; 1988; Vol. 16.

(3) Spagnoletto, G. Innovation in Food Grade Hypochlorination Generation and Injection Plant at Al Taweelah Site. *Desalination* **2005**, *182* (1–3), 259–265. https://doi.org/10.1016/j.desal.2005.04.016.

(4) Jeong, H. J.; Kim, H. R.; Kim, K. I.; Kim, K. Y.; Park, K. H.; Kim, S. T.; Yoo, Y. D.; Song, J. Y.; Kim, J. S.; Seong, K. A.; et al. NaOCl Produced by Electrolysis of Natural Seawater as a Potential Method to Control Marine Red-Tide Dinoflagellates. *Phycologia* **2002**, *41* (6), 643–656. https://doi.org/10.2216/i0031-8884-41-6-643.1.

(5) Chen, S.; Zheng, Y.; Wang, S.; Chen, X. Ti/RuO_2–Sb_2O_5–SnO_2 Electrodes for Chlorine Evolution from Seawater. *J. Chem. Eng.* **2011**, *172* (1), 47–51. https://doi.org/10.1016/j.cej.2011.05.059.

(6) Yang, Y.; Shin, J.; Jasper, J. T.; Hoffmann, M. R. Multilayer Heterojunction Anodes for Saline Wastewater Treatment: Design Strategies and Reactive Species Generation Mechanisms. *Environ. Sci. Technol.* **2016**, *50* (16), 8780–8787. https://doi.org/10.1021/acs.est.6b00688.

(7) Cho, K.; Qu, Y.; Kwon, D.; Zhang, H.; Cid, C. A.; Aryanfar, A.; Hoffmann, M. R. Effects of Anodic Potential and Chloride Ion on Overall Reactivity in Electrochemical Reactors Designed for Solar-Powered Wastewater Treatment. *Environ. Sci. Technol.* **2014**, *48* (4), 2377–2384. https://doi.org/10.1021/es404137u.

(8) Yang, Y.; Lin, L.; Tse, L. K.; Dong, H.; Yu, S.; Hoffmann, M. R. Membrane-Separated Electrochemical Latrine Wastewater Treatment. *Environ. Sci.: Water Res. Technol.* **2019**, *5* (1), 51–59. https://doi.org/10.1039/C8EW00698A.

(9) Jasper, J. T.; Yang, Y.; Hoffmann, M. R. Toxic Byproduct Formation during Electrochemical Treatment of Latrine Wastewater. *Environ. Sci. Technol.* **2017**, *51* (12), 7111–7119. https://doi.org/10.1021/acs.est.7b01002.

(10) Cho, K.; Hoffmann, M. R. Urea Degradation by Electrochemically Generated Reactive Chlorine Species: Products and Reaction Pathways. *Environ. Sci. Technol.* **2014**, *48* (19), 11504–11511. https://doi.org/10.1021/es5025405.

(11) Cho, K.; Kwon, D.; Hoffmann, M. R. Electrochemical Treatment of Human Waste Coupled with Molecular Hydrogen Production. *RSC Adv.* **2014**, *4* (9), 4596–4608. https://doi.org/10.1039/C3RA46699J.

(12) Jasper, J. T.; Shafaat, O. S.; Hoffmann, M. R. Electrochemical Transformation of Trace Organic Contaminants in Latrine Wastewater. *Environ. Sci. Technol.* **2016**, *50* (18), 10198–10208. https://doi.org/10.1021/acs.est.6b02912.

(13) Beer, H. B. The Invention and Industrial Development of Metal Anodes. *J. Electrochem. Soc.* **1980**, *127* (8), 303C. https://doi.org/10.1149/1.2130021.

(14) Hoseinieh, S. M.; Ashrafizadeh, F.; Maddahi, M. H. A Comparative Investigation of the Corrosion Behavior of RuO_2–IrO_2–TiO_2 Coated Titanium Anodes in Chloride Solutions. *J. Electrochem. Soc.* **2010**, *157* (4), E50. https://doi.org/10.1149/1.3294569.

(15) Liu, B.; Wang, C.; Chen, Y.; Ma, B. Electrochemical Behavior and Corrosion Mechanism of Ti/IrO_2-RuO_2 Anodes in Sulphuric Acid Solution. *J. Electroanal. Chem.* **2019**, *837*, 175–183. https://doi.org/10.1016/j.jelechem.2019.02.039.

(16) Burrows, I. R.; Denton, D. A.; Harrison, J. A. Chlorine and Oxygen Evolution on Various Compositions of RuO_2/TiO_2 Electrodes. *Electrochim. Acta* **1978**, *23* (6), 493–500. https://doi.org/10.1016/0013-4686(78)85026-9.

(17) Yi, Z.; Kangning, C.; Wei, W.; Wang, J.; Lee, S. Effect of IrO_2 Loading on RuO_2–IrO_2–TiO_2 Anodes: A Study of Microstructure and Working Life for the Chlorine Evolution Reaction. *Ceram. Int.* **2007**, *33* (6), 1087–1091. https://doi.org/10.1016/j.ceramint.2006.03.025.

(18) Kameyama, K.; Shohji, S.; Onoue, S.; Nishimura, K.; Yahikozawa, K.; Takasu, Y. Preparation of Ultrafine RuO_2-TiO_2 Binary Oxide Particles by a Sol-gel Process. *J. Electrochem. Soc.* **1993**, *140* (4), 1034.

(19) Comninellis, Ch.; Vercesi, G. P. Problems in DSA® Coating Deposition by Thermal Decomposition. *J Appl. Electrochem.* **1991**, *21* (2), 136–142. https://doi.org/10.1007/BF01464294.

(20) Comninellis, Ch.; Vercesi, G. P. Characterization of DSA®-Type Oxygen Evolving Electrodes: Choice of a Coating. *J Appl. Electrochem.* **1991**, *21* (4), 335–345. https://doi.org/10.1007/BF01020219.

(21) Trasatti, S. Progress in the Understanding of the Mechanism of Chlorine Evolution at Oxide Electrodes. *Electrochim. Acta* **1987**, *32* (3), 369–382. https://doi.org/10.1016/0013-4686(87)85001-6.

(22) Conway, B. E.; Novak, D. M. Chloride Ion Adsorption Effects in the Recombination-Controlled Kinetics of Anodic Chlorine Evolution at Pt Electrodes. *J. Chem. Soc., Faraday Trans. 1* **1979**, *75* (0), 2454. https://doi.org/10.1039/f19797502454.

(23) Yang, Y.; Hoffmann, M. R. Synthesis and Stabilization of Blue-Black TiO_2 Nanotube Arrays for Electrochemical Oxidant Generation and Wastewater Treatment. *Environ. Sci. Technol.* **2016**, *50* (21), 11888–11894. https://doi.org/10.1021/acs.est.6b03540.

(24) Cid, C. A.; Jasper, J. T.; Hoffmann, M. R. Phosphate Recovery from Human Waste via the Formation of Hydroxyapatite during Electrochemical Wastewater Treatment. *ACS Sustain. Chem. Eng.* **2018**, *6* (3), 3135–3142. https://doi.org/10.1021/acssuschemeng.7b03155.

(25) Duby, P. The History of Progress in Dimensionally Stable Anodes. *JOM* **1993**, *45* (3), 41–43.

(26) Tilak, B. V.; Tari, K.; Hoover, C. L. Metal Anodes and Hydrogen Cathodes: Their Activity Towards O_2 Evolution and ClO_3- Reduction Reactions. *J. Electrochem. Soc.* **1988**, *135* (6), 8.

(27) Zeradjanin, A. R.; Menzel, N.; Schuhmann, W.; Strasser, P. On the Faradaic Selectivity and the Role of Surface Inhomogeneity during the Chlorine Evolution Reaction on Ternary Ti–Ru–Ir Mixed Metal Oxide Electrocatalysts. *Phys. Chem. Chem. Phys.* **2014**, *16* (27), 13741–13747. https://doi.org/10.1039/C4CP00896K.

(28) Vos, J. G.; Liu, Z.; Speck, F. D.; Perini, N.; Fu, W.; Cherevko, S.; Koper, M. T. M. Selectivity Trends Between Oxygen Evolution and Chlorine Evolution on Iridium-Based Double Perovskites in Acidic Media. *ACS Catal.* **2019**, *9* (9), 8561–8574. https://doi.org/10.1021/acscatal.9b01159.

(29) Kuo, D.-Y.; Paik, H.; Nelson, J. N.; Shen, K. M.; Schlom, D. G.; Suntivich, J. Chlorine Evolution Reaction Electrocatalysis on RuO_2 (110) and IrO_2 (110) Grown Using Molecular-Beam Epitaxy. *J. Chem. Phys.* **2019**, *150* (4), 041726. https://doi.org/10.1063/1.5051429.

(30) Gedam, N.; Neti, N. R.; Kormunda, M.; Subrt, J.; Bakardjieva, S. Novel Lead Dioxide-Graphite-Polymer Composite Anode for Electrochemical Chlorine Generation. *Electrochim. Acta* **2015**, *169*, 109–116. https://doi.org/10.1016/j.electacta.2015.04.058.

(31) Cao, H.; Lu, D.; Lin, J.; Ye, Q.; Wu, J.; Zheng, G. Novel Sb-Doped Ruthenium Oxide Electrode with Ordered Nanotube Structure and Its Electrocatalytic Activity toward Chlorine Evolution. *Electrochim. Acta* **2013**, *91*, 234–239. https://doi.org/10.1016/j.electacta.2012.12.118.

(32) Cho, K.; Hoffmann, M. R. $Bi_xTi_{1x}O_z$ Functionalized Heterojunction Anode with an Enhanced Reactive Chlorine Generation Efficiency in Dilute Aqueous Solutions. *Chem. Mater.* **2015**, *27* (6), 2224–2233. https://doi.org/10.1021/acs.chemmater.5b00376.

(33) Menzel, N.; Ortel, E.; Mette, K.; Kraehnert, R.; Strasser, P. Dimensionally Stable Ru/Ir/TiO_2-Anodes with Tailored Mesoporosity for Efficient Electrochemical Chlorine Evolution. *ACS Catal.* **2013**, *3* (6), 1324–1333. https://doi.org/10.1021/cs4000238.

(34) Jiang, M.; Wang, H.; Li, Y.; Zhang, H.; Zhang, G.; Lu, Z.; Sun, X.; Jiang, L. Superaerophobic RuO_2-Based Nanostructured Electrode for High-Performance Chlorine Evolution Reaction. *Small* **2017**, *13* (4), 1602240. https://doi.org/10.1002/smll.201602240.

(35) Ferro, S.; De Battisti, A. Electrocatalysis and Chlorine Evolution Reaction at Ruthenium Dioxide Deposited on Conductive Diamond. *J. Phys. Chem. B* **2002**, *106* (9), 2249–2254. https://doi.org/10.1021/jp012195i.

(36) Santana, M. H. P.; De Faria, L. A. Oxygen and Chlorine Evolution on $RuO_2+TiO_2+CeO_2+Nb_2O_5$ Mixed Oxide Electrodes. *Electrochim. Acta* **2006**, *51* (17), 3578–3585. https://doi.org/10.1016/j.electacta.2005.09.050.

(37) Sohrabnejad-Eskan, I.; Goryachev, A.; Exner, K. S.; Kibler, L. A.; Hensen, E. J. M.; Hofmann, J. P.; Over, H. Temperature-Dependent Kinetic Studies of the Chlorine

Evolution Reaction over RuO_2 (110) Model Electrodes. *ACS Catal.* **2017**, *7* (4), 2403–2411. https://doi.org/10.1021/acscatal.6b03415.

(38) Rojas, M. I.; Esplandiu, M. J.; Avalle, L. B.; Leiva, E. P. M.; Macagno, V. A. The Oxygen and Chlorine Evolution Reactions at Titanium Oxide Electrodes Modified with Platinum. *Electrochim. Acta* **1998**, *43* (12–13), 1785–1794. https://doi.org/10.1016/S0013-4686(97)10002-0.

(39) Finke, C. E.; Omelchenko, S. T.; Jasper, J. T.; Lichterman, M. F.; Read, C. G.; Lewis, N. S.; Hoffmann, M. R. Enhancing the Activity of Oxygen-Evolution and Chlorine-Evolution Electrocatalysts by Atomic Layer Deposition of TiO_2. *Energy Environ. Sci.* **2019**, *12* (1), 358–365. https://doi.org/10.1039/C8EE02351D.

(40) Moreno-Hernandez, I. A.; Brunschwig, B. S.; Lewis, N. S. Crystalline Nickel, Cobalt, and Manganese Antimonates as Electrocatalysts for the Chlorine Evolution Reaction. *Energy Environ. Sci.* **2019**, *12* (4), 1241–1248. https://doi.org/10.1039/C8EE03676D.

(41) Neodo, S.; Rosestolato, D.; Ferro, S.; De Battisti, A. On the Electrolysis of Dilute Chloride Solutions: Influence of the Electrode Material on Faradaic Efficiency for Active Chlorine, Chlorate and Perchlorate. *Electrochim. Acta* **2012**, *80*, 282–291. https://doi.org/10.1016/j.electacta.2012.07.017.

(42) Macounová, K.; Makarova, M.; Jirkovský, J.; Franc, J.; Krtil, P. Parallel Oxygen and Chlorine Evolution on $Ru_{1-x}Ni_xO_{2-y}$ Nanostructured Electrodes. *Electrochim. Acta* **2008**, *53* (21), 6126–6134. https://doi.org/10.1016/j.electacta.2007.11.014.

(43) Palma-Goyes, R. E.; Vazquez-Arenas, J.; Ostos, C.; Manzo-Robledo, A.; Romero-Ibarra, I.; Calderón, J. A.; González, I. In Search of the Active Chlorine Species on Ti/ZrO_2-RuO_2-Sb_2O_3 Anodes Using DEMS and XPS. *Electrochim. Acta* **2018**, *275*, 265–274. https://doi.org/10.1016/j.electacta.2018.04.114.

(44) Lide, D. R. *CRC Handbook of Chemistry and Physics: A Ready-Reference Book of Chemical and Physical Data*; CRC press, 1995.

(45) Kuhn, A. T.; Mortimer, C. J. The Efficiency of Chlorine Evolution in Dilute Brines on Ruthenium Dioxide Electrodes. *J Appl. Electrochem.* **1972**, *2* (4), 283–287. https://doi.org/10.1007/BF00615275.

(46) Rius, A.; Llopis, J. Sobre La Oxidacion Anodica De Los Hipocloritos Alcalinos. In *Anales De Fisica y Quimica*; 1945; Vol. 41, pp 1030–1053.

(47) Vos, J. G.; Koper, M. T. M. Measurement of Competition between Oxygen Evolution and Chlorine Evolution Using Rotating Ring-Disk Electrode Voltammetry. *J. Electroanal. Chem.* **2018**, *819*, 260–268. https://doi.org/10.1016/j.jelechem.2017.10.058.

(48) Chung, C. M.; Hong, S. W.; Cho, K.; Hoffmann, M. R. Degradation of Organic Compounds in Wastewater Matrix by Electrochemically Generated Reactive Chlorine Species: Kinetics and Selectivity. *Catal. Today* **2018**, *313*, 189–195. https://doi.org/10.1016/j.cattod.2017.10.027.

(49) Wellington, T. C. *Modern Chlor-Alkali Technology*; Springer Science & Business Media, 2012; Vol. 5.

(50) Kelsall, G. H.; Robbins, D. J. Thermodynamics of Ti-H_2O-F(-Fe) Systems at 298 K. *J. Electroanal. Chem. Interfacial Electrochem.* **1990**, *283* (1–2), 135–157. https://doi.org/10.1016/0022-0728(90)87385-W.

(51) Hoseinieh, S. M.; Ashrafizadeh, F. Influence of Electrolyte Composition on Deactivation Mechanism of a Ti/$Ru_{0.25}Ir_{0.25}Ti_{0.5}O_2$ Electrode. *Ionics* **2013**, *19* (1), 113–125. https://doi.org/10.1007/s11581-012-0737-5.

(52) Hu, J. M.; Meng, H. M.; Zhang, J. Q.; Cao, C. N. Degradation Mechanism of Long Service Life Ti/IrO_2–Ta_2O_5 Oxide Anodes in Sulphuric Acid. *Corros. Sci.* **2002**, *44* (8), 1655–1668. https://doi.org/10.1016/S0010-938X(01)00165-2.

(53) Xu, L. K.; Scantlebury, J. D. A Study on the Deactivation of an IrO_2–Ta_2O_5 Coated Titanium Anode. *Corros. Sci.* **2003**, *45* (12), 2729–2740. https://doi.org/10.1016/S0010-938X(03)00108-2.

(54) Bock, C.; Spinney, H.; MacDougall, B. A Study of the Deactivation and Service Life of Ir Oxide Anodes Supported on Al Substrates. *J. Appl. Electrochem.* **2000**, *30* (5), 523–532. https://doi.org/10.1023/A:1003961701335.

(55) Tan, X.; Shen, J.; Semagina, N.; Secanell, M. Decoupling Structure-Sensitive Deactivation Mechanisms of Ir/IrO_x Electrocatalysts toward Oxygen Evolution Reaction. *J. Catal.* **2019**, *371*, 57–70. https://doi.org/10.1016/j.jcat.2019.01.018.

(56) Mazhari Abbasi, H.; Jafarzadeh, K.; Mirali, S. M. An Investigation of the Effect of RuO_2 on the Deactivation and Corrosion Mechanism of a Ti/IrO_2 + Ta_2O_5 Coating in an OER Application. *J. Electroanal. Chem.* **2016**, *777*, 67–74. https://doi.org/10.1016/j.jelechem.2016.07.036.

(57) Lassali, T. A. F.; Boodts, J. F. C.; Bulhões, L. O. S. Faradaic Impedance Investigation of the Deactivation Mechanism of Ir-Based Ceramic Oxides Containing TiO_2 and SnO_2. *J. Appl. Electrochem.* **2000**, *30* (5), 625–634. https://doi.org/10.1023/A:1003901520705.

(58) Panić, V.; A. Dekanski; Mišković-Stanković, V. B.; Milonjić, S.; Nikolić, B. On the Deactivation Mechanism of RuO_2–TiO_2/Ti Anodes Prepared by the Sol–Gel Procedure. *J. Electroanal. Chem.* **2005**, *579* (1), 67–76. https://doi.org/10.1016/j.jelechem.2005.01.026.

(59) Jovanovič, P.; Hodnik, N.; Ruiz-Zepeda, F.; Arčon, I.; Jozinović, B.; Zorko, M.; Bele, M.; Šala, M.; Šelih, V. S.; Hočevar, S.; et al. Electrochemical Dissolution of Iridium and Iridium Oxide Particles in Acidic Media: Transmission Electron Microscopy, Electrochemical Flow Cell Coupled to Inductively Coupled Plasma Mass Spectrometry, and X-Ray Absorption Spectroscopy Study. *J. Am. Chem. Soc.* **2017**, *139* (36), 12837–12846. https://doi.org/10.1021/jacs.7b08071.

(60) Hu, J.-M.; Sun, X.-J.; Hou, Y.-Y.; Zhang, J.-Q.; Cao, C.-N. Degradation Characteristics of IrO_2-Type DSA® in Methanol Aqueous Solutions. *Electrochim. Acta* **2008**, *53* (7), 3127–3138. https://doi.org/10.1016/j.electacta.2007.11.045.

(61) Stevens, M. B.; Enman, L. J.; Batchellor, A. S.; Cosby, M. R.; Vise, A. E.; Trang, C. D. M.; Boettcher, S. W. Measurement Techniques for the Study of Thin Film Heterogeneous Water Oxidation Electrocatalysts. *Chem. Mater.* **2017**, *29* (1), 120–140. https://doi.org/10.1021/acs.chemmater.6b02796.

(62) Moysiadou, A.; Hu, X. Stability Profiles of Transition Metal Oxides in the Oxygen Evolution Reaction in Alkaline Medium. *J. Mater. Chem. A* **2019**, *7* (45), 25865–25877. https://doi.org/10.1039/C9TA10308B.

(63) Enman, L. J.; Burke, M. S.; Batchellor, A. S.; Boettcher, S. W. Effects of Intentionally Incorporated Metal Cations on the Oxygen Evolution Electrocatalytic

Activity of Nickel (Oxy)Hydroxide in Alkaline Media. *ACS Catal.* **2016**, *6* (4), 2416–2423. https://doi.org/10.1021/acscatal.5b02924.

(64) Lu, X.; Zhao, C. Electrodeposition of Hierarchically Structured Three-Dimensional Nickel–Iron Electrodes for Efficient Oxygen Evolution at High Current Densities. *Nat. Commun.* **2015**, *6* (1), 6616. https://doi.org/10.1038/ncomms7616.

(65) Yang, C.; Batuk, M.; Jacquet, Q.; Rousse, G.; Yin, W.; Zhang, L.; Hadermann, J.; Abakumov, A. M.; Cibin, G.; Chadwick, A.; et al. Revealing PH-Dependent Activities and Surface Instabilities for Ni-Based Electrocatalysts during the Oxygen Evolution Reaction. *ACS Energy Lett.* **2018**, *3* (12), 2884–2890. https://doi.org/10.1021/acsenergylett.8b01818.

(66) Song, F.; Bai, L.; Moysiadou, A.; Lee, S.; Hu, C.; Liardet, L.; Hu, X. Transition Metal Oxides as Electrocatalysts for the Oxygen Evolution Reaction in Alkaline Solutions: An Application-Inspired Renaissance. *J. Am. Chem. Soc.* **2018**, *140* (25), 7748–7759. https://doi.org/10.1021/jacs.8b04546.

(67) Ooka, H.; Huang, J.; Exner, K. S. The Sabatier Principle in Electrocatalysis: Basics, Limitations, and Extensions. *Front. Energy Res.* **2021**, *9*, 654460. https://doi.org/10.3389/fenrg.2021.654460.

(68) Zeradjanin, A. R.; Menzel, N.; Strasser, P.; Schuhmann, W. Role of Water in the Chlorine Evolution Reaction at RuO_2-Based Electrodes-Understanding Electrocatalysis as a Resonance Phenomenon. *ChemSusChem* **2012**, *5* (10), 1897–1904. https://doi.org/10.1002/cssc.201200193.

(69) Dickens, C. F.; Nørskov, J. K. A Theoretical Investigation into the Role of Surface Defects for Oxygen Evolution on RuO_2. *J. Phys. Chem. C* **2017**, *121* (34), 18516–18524. https://doi.org/10.1021/acs.jpcc.7b03481.

(70) Hansen, H. A.; Man, I. C.; Studt, F.; Abild-Pedersen, F.; Bligaard, T.; Rossmeisl, J. Electrochemical Chlorine Evolution at Rutile Oxide (110) Surfaces. *Phys. Chem. Chem. Phys.* **2010**, *12* (1), 283–290. https://doi.org/10.1039/B917459A.

(71) de Moura, D. C.; de Araújo, C. K. C.; Zanta, C. L. P. S.; Salazar, R.; Martínez-Huitle, C. A. Active Chlorine Species Electrogenerated on $Ti/Ru_{0.3}Ti_{0.7}O_2$ Surface: Electrochemical Behavior, Concentration Determination and Their Application. *J.*

Electroanal. Chem. **2014**, *731*, 145–152. https://doi.org/10.1016/j.jelechem.2014.08.008.

(72) Cheng, H.; Scott, K.; Ramshaw, C. Chlorine Evolution in a Centrifugal Field. *J. Appl. Electrochem.* **2002**, *32* (7), 831–838. https://doi.org/10.1023/A:1020170627227.

(73) Gaudet, J.; Tavares, A. C.; Trasatti, S.; Guay, D. Physicochemical Characterization of Mixed RuO_2-SnO_2 Solid Solutions. *Chem. Mater.* **2005**, *17* (6), 1570–1579. https://doi.org/10.1021/cm048129l.

(74) Vazquez-Gomez, L.; Ferro, S.; De Battisti, A. Preparation and Characterization of RuO_2–IrO_2–SnO_2 Ternary Mixtures for Advanced Electrochemical Technology. *Appl. Catal. B* **2006**, *67* (1–2), 34–40. https://doi.org/10.1016/j.apcatb.2006.03.023.

(75) Palma-Goyes, R. E.; Vazquez-Arenas, J.; Torres-Palma, R. A.; Ostos, C.; Ferraro, F.; González, I. The Abatement of Indigo Carmine Using Active Chlorine Electrogenerated on Ternary Sb_2O_5-Doped Ti/RuO_2-ZrO_2 Anodes in a Filter-Press FM01-LC Reactor. *Electrochim. Acta* **2015**, *174*, 735–744. https://doi.org/10.1016/j.electacta.2015.06.037.

(76) Zeradjanin, A. R.; La Mantia, F.; Masa, J.; Schuhmann, W. Utilization of the Catalyst Layer of Dimensionally Stable Anodes—Interplay of Morphology and Active Surface Area. *Electrochim. Acta* **2012**, *82*, 408–414. https://doi.org/10.1016/j.electacta.2012.04.101.

(77) Arikawa, T.; Murakami, Y.; Takasu, Y. Simultaneous Determination of Chlorine and Oxygen Evolving at RuO_2/Ti and RuO_2-TiO_2/Ti Anodes by Differential Electrochemical Mass Spectroscopy. *J. Appl. Electrochem. 28* (1998), 511–516.

(78) Macounová, K.; Makarova, M.; Franc, J.; Jirkovský, J.; Krtil, P. Influence of Oxygen on Reactivity of $Ru_{1-x}Fe_xO_{2-y}$-Doped Materials. *Electrochem. Solid-State Lett.* **2008**, *11* (12), F27. https://doi.org/10.1149/1.2978963.

(79) Petrykin, V.; Macounová, K.; Okube, M.; Mukerjee, S.; Krtil, P. Local Structure of Co Doped RuO_2 Nanocrystalline Electrocatalytic Materials for Chlorine and Oxygen Evolution. *Catal. Today* **2013**, *202*, 63–69. https://doi.org/10.1016/j.cattod.2012.03.075.

(80) Petrykin, V.; Bastl, Z.; Franc, J.; Macounova, K.; Makarova, M.; Mukerjee, S.; Ramaswamy, N.; Spirovova, I.; Krtil, P. Local Structure of Nanocrystalline

$Ru_{1-x}Ni_xO_{2-\delta}$ Dioxide and Its Implications for Electrocatalytic Behavior—An XPS and XAS Study. *J. Phys. Chem. C* **2009**, *113* (52), 21657–21666. https://doi.org/10.1021/jp904935e.

(81) Macounova, K.; Makarova, M.; Krtil, P. Oxygen Evolution on Nanocrystalline RuO_2 and $Ru_{0.9}Ni_{0.1}O_{2-\delta}$ Electrodes – DEMS Approach to Reaction Mechanism Determination. *Electrochem. commun.* **2009**, *11* (10), 1865–1868. https://doi.org/10.1016/j.elecom.2009.08.004.

(82) Macounová, K.; Jirkovský, J.; Makarova, M. V.; Franc, J.; Krtil, P. Oxygen Evolution on $Ru_{1-x}Ni_xO_{2-y}$ Nanocrystalline Electrodes. *J. Solid State Electrochem.* **2009**, *13* (6), 959–965. https://doi.org/10.1007/s10008-008-0624-1.

(83) Petrykin, V.; Macounova, K.; Shlyakhtin, O. A.; Krtil, P. Tailoring the Selectivity for Electrocatalytic Oxygen Evolution on Ruthenium Oxides by Zinc Substitution. *Angew. Chem. Int. Ed.* **2010**, *49* (28), 4813–4815. https://doi.org/10.1002/anie.200907128.

(84) Makarova, M. V.; Jirkovský, J.; Klementová, M.; Jirka, I.; Macounová, K.; Krtil, P. The Electrocatalytic Behavior of $Ru_{0.8}Co_{0.2}O_{2-x}$—the Effect of Particle Shape and Surface Composition. *Electrochim. Acta* **2008**, *53* (5), 2656–2664. https://doi.org/10.1016/j.electacta.2007.01.084.

(85) Petrykin, V.; Macounova, K.; Franc, J.; Shlyakhtin, O.; Klementova, M.; Mukerjee, S.; Krtil, P. Zn-Doped RuO_2 Electrocatalyts for Selective Oxygen Evolution: Relationship between Local Structure and Electrocatalytic Behavior in Chloride Containing Media. *Chem. Mater.* **2011**, *23* (2), 200–207. https://doi.org/10.1021/cm1028782.

(86) Abbott, D. F.; Petrykin, V.; Okube, M.; Bastl, Z.; Mukerjee, S.; Krtil, P. Selective Chlorine Evolution Catalysts Based on Mg-Doped Nanoparticulate Ruthenium Dioxide. *J. Electrochem. Soc.* **2015**, *162* (1), H23–H31. https://doi.org/10.1149/2.0541501jes.

(87) Audichon, T.; Mayousse, E.; Morisset, S.; Morais, C.; Comminges, C.; Napporn, T. W.; Kokoh, K. B. Electroactivity of RuO_2–IrO_2 Mixed Nanocatalysts toward the Oxygen Evolution Reaction in a Water Electrolyzer Supplied by a Solar Profile. *Int. J.*

Hydrog. Energy **2014**, *39* (30), 16785–16796. https://doi.org/10.1016/j.ijhydene.2014.07.170.

(88) Audichon, T.; Napporn, T. W.; Canaff, C.; Morais, C.; Comminges, C.; Kokoh, K. B. IrO_2 Coated on RuO_2 as Efficient and Stable Electroactive Nanocatalysts for Electrochemical Water Splitting. *J. Phys. Chem. C* **2016**, *120* (5), 2562–2573. https://doi.org/10.1021/acs.jpcc.5b11868.

(89) Pfeifer, V.; Jones, T. E.; Wrabetz, S.; Massué, C.; Velasco Vélez, J. J.; Arrigo, R.; Scherzer, M.; Piccinin, S.; Hävecker, M.; Knop-Gericke, A.; et al. Reactive Oxygen Species in Iridium-Based OER Catalysts. *Chem. Sci.* **2016**, *7* (11), 6791–6795. https://doi.org/10.1039/C6SC01860B.

(90) Angelinetta, C.; Trasatti, S.; Atanososka, Lj. D.; Atanasoski, R. T. Surface Properties of RuO_2 + IrO_2 Mixed Oxide Electrodes. *J. electroanal. chem. interfacial electrochem.* **1986**, *214* (1–2), 535–546. https://doi.org/10.1016/0022-0728(86)80122-X.

(91) Danilovic, N.; Subbaraman, R.; Chang, K. C.; Chang, S. H.; Kang, Y.; Snyder, J.; Paulikas, A. P.; Strmcnik, D.; Kim, Y. T.; Myers, D.; et al. Using Surface Segregation To Design Stable Ru-Ir Oxides for the Oxygen Evolution Reaction in Acidic Environments. *Angew. Chem. Int. Ed.* **2014**, *53* (51), 14016–14021. https://doi.org/10.1002/anie.201406455.

(92) De Battisti, A.; Brina, R.; Gavelli, G.; Benedetti, A.; Fagherazzi, G. Influence of the Valve Metal Oxide on the Properties of Ruthenium Based Mixed Oxide Electrodes. *J. electroanal. chem. interfacial electrochem.* **1986**, *200* (1–2), 93–104. https://doi.org/10.1016/0022-0728(86)90048-3.

(93) Yoon, Y.; Cho, E.; Jung, Y.; Kwon, M.; Yoon, J.; Kang, J.-W. Evaluation of the Formation of Oxidants and By-Products Using Pt/Ti, RuO_2/Ti, and IrO_2/Ti Electrodes in the Electrochemical Process. *Environ. Technol.* **2015**, *36* (3), 317–326. https://doi.org/10.1080/09593330.2014.946098.

(94) Eberil’, V. I.; Fedotova, N. S.; Novikov, E. A.; Mazanko, A. F. Studying the Link between the Potential of a Metal-Oxide Anode, the Current Efficiency for Chlorate, and the Current Losses for the Oxygen and Chlorine Evolution in a Wide Range of the Chlorate Electrolysis Conditions. *Russ. J. Electrochem.* **2000**, *36* (12), 7.

(95) Serna-Galvis, E. A.; Jojoa-Sierra, S. D.; Berrio-Perlaza, K. E.; Ferraro, F.; Torres-Palma, R. A. Structure-Reactivity Relationship in the Degradation of Three Representative Fluoroquinolone Antibiotics in Water by Electrogenerated Active Chlorine. *J. Chem. Eng.* **2017**, *315*, 552–561. https://doi.org/10.1016/j.cej.2017.01.062.

(96) Sumaria, V.; Krishnamurthy, D.; Viswanathan, V. Quantifying Confidence in DFT Predicted Surface Pourbaix Diagrams and Associated Reaction Pathways for Chlorine Evolution. *ACS Catal.* **2018**, *8* (10), 9034–9042. https://doi.org/10.1021/acscatal.8b01432.

(97) Trieu, V.; Schley, B.; Natter, H.; Kintrup, J.; Bulan, A.; Hempelmann, R. RuO_2-Based Anodes with Tailored Surface Morphology for Improved Chlorine Electro-Activity. *Electrochim. Acta* **2012**, *78*, 188–194. https://doi.org/10.1016/j.electacta.2012.05.122.

(98) Zeradjanin, A. R.; Topalov, A. A.; Van Overmeere, Q.; Cherevko, S.; Chen, X.; Ventosa, E.; Schuhmann, W.; Mayrhofer, K. J. J. Rational Design of the Electrode Morphology for Oxygen Evolution – Enhancing the Performance for Catalytic Water Oxidation. *RSC Adv.* **2014**, *4* (19), 9579. https://doi.org/10.1039/c3ra45998e.

(99) Chen, R.; Trieu, V.; Zeradjanin, A. R.; Natter, H.; Teschner, D.; Kintrup, J.; Bulan, A.; Schuhmann, W.; Hempelmann, R. Microstructural Impact of Anodic Coatings on the Electrochemical Chlorine Evolution Reaction. *Phys. Chem. Chem. Phys.* **2012**, *14* (20), 7392. https://doi.org/10.1039/c2cp41163f.

(100) Moreno-Hernandez, I. A.; MacFarland, C. A.; Read, C. G.; Papadantonakis, K. M.; Brunschwig, B. S.; Lewis, N. S. Crystalline Nickel Manganese Antimonate as a Stable Water-Oxidation Catalyst in Aqueous 1.0 M H_2SO_4. *Energy Environ. Sci.* **2017**, *10* (10), 2103–2108. https://doi.org/10.1039/C7EE01486D.

(101) Roy, C.; Rao, R. R.; Stoerzinger, K. A.; Hwang, J.; Rossmeisl, J.; Chorkendorff, I.; Shao-Horn, Y.; Stephens, I. E. L. Trends in Activity and Dissolution on RuO_2 under Oxygen Evolution Conditions: Particles versus Well-Defined Extended Surfaces. *ACS Energy Lett.* **2018**, *3* (9), 2045–2051. https://doi.org/10.1021/acsenergylett.8b01178.

(102) Mozota, J.; Vukovic, M.; Conway, B. E. Enhanced Electrocatalysis for Chlorine Evolution on Oxidized Ir and Ru Anodes Modified by Potential Cycling. *J. Electroanal.*

Chem. Interfacial Electrochem. **1980**, *114* (1), 153–157. https://doi.org/10.1016/S0022-0728(80)80443-8.

(103) Pfeifer, V.; Jones, T. E.; Velasco Vélez, J. J.; Massué, C.; Greiner, M. T.; Arrigo, R.; Teschner, D.; Girgsdies, F.; Scherzer, M.; Allan, J.; et al. The Electronic Structure of Iridium Oxide Electrodes Active in Water Splitting. *Phys. Chem. Chem. Phys.* **2016**, *18* (4), 2292–2296. https://doi.org/10.1039/C5CP06997A.

(104) Näslund, L.-Å.; Sánchez-Sánchez, C. M.; Ingason, Á. S.; Bäckström, J.; Herrero, E.; Rosen, J.; Holmin, S. The Role of TiO_2 Doping on RuO_2 -Coated Electrodes for the Water Oxidation Reaction. *J. Phys. Chem. C* **2013**, *117* (12), 6126–6135. https://doi.org/10.1021/jp308941g.

(105) Yang, Y.; Kao, L. C.; Liu, Y.; Sun, K.; Yu, H.; Guo, J.; Liou, S. Y. H.; Hoffmann, M. R. Cobalt-Doped Black TiO_2 Nanotube Array as a Stable Anode for Oxygen Evolution and Electrochemical Wastewater Treatment. *ACS Catal.* **2018**, *8* (5), 4278–4287. https://doi.org/10.1021/acscatal.7b04340.

(106) Takata, T.; Domen, K. Defect Engineering of Photocatalysts by Doping of Aliovalent Metal Cations for Efficient Water Splitting. *J. Phys. Chem. C* **2009**, *113* (45), 19386–19388. https://doi.org/10.1021/jp908621e.

(107) Pan, S. S.; Wang, S.; Zhang, Y. X.; Luo, Y. Y.; Kong, F. Y.; Xu, S. C.; Xu, J. M.; Li, G. H. P-Type Conduction in Nitrogen-Doped SnO_2 Films Grown by Thermal Processing of Tin Nitride Films. *Appl. Phys. A* **2012**, *109* (2), 267–271. https://doi.org/10.1007/s00339-012-7288-5.

(108) Babar, A. R.; Shinde, S. S.; Moholkar, A. V.; Bhosale, C. H.; Kim, J. H.; Rajpure, K. Y. Structural and Optoelectronic Properties of Antimony Incorporated Tin Oxide Thin Films. *J. Alloys Compd.* **2010**, *505* (2), 416–422. https://doi.org/10.1016/j.jallcom.2010.06.091.

(109) Jeon, S.; Park, Y. M.; Park, J.; Saravanan, K.; Jeong, H.-K.; Bae, J. W. Synergistic Effects of Nb_2O_5 Promoter on Ru/Al_2O_3 for an Aqueous-Phase Hydrodeoxygenation of Glycerol to Hydrocarbons. *Appl. Catal. A: Gen.* **2018**, *551*, 49–62. https://doi.org/10.1016/j.apcata.2017.12.006.

(110) López, N.; Gómez-Segura, J.; Marín, R. P.; Pérez-Ramírez, J. Mechanism of HCl Oxidation (Deacon Process) over RuO_2. *J. Catal.* **2008**, *255* (1), 29–39. https://doi.org/10.1016/j.jcat.2008.01.020.

(111) Crihan, D.; Knapp, M.; Zweidinger, S.; Lundgren, E.; Weststrate, C. J.; Andersen, J. N.; Seitsonen, A. P.; Over, H. Stable Deacon Process for HCl Oxidation over RuO_2. *Angew. Chem. Int. Ed.* **2008**, *47* (11), 2131–2134. https://doi.org/10.1002/anie.200705124.

(112) Exner, K. S.; Anton, J.; Jacob, T.; Over, H. Chlorine Evolution Reaction on RuO_2(110): Ab Initio Atomistic Thermodynamics Study - Pourbaix Diagrams. *Electrochim. Acta* **2014**, *120*, 460–466. https://doi.org/10.1016/j.electacta.2013.11.027.

(113) Exner, K. S.; Anton, J.; Jacob, T.; Over, H. Microscopic Insights into the Chlorine Evolution Reaction on RuO_2(110): A Mechanistic Ab Initio Atomistic Thermodynamics Study. *Electrocatalysis* **2015**, *6* (2), 163–172. https://doi.org/10.1007/s12678-014-0220-3.

(114) Exner, K. S. Beyond the Traditional Volcano Concept: Overpotential-Dependent Volcano Plots Exemplified by the Chlorine Evolution Reaction over Transition-Metal Oxides. *J. Phys. Chem. C* **2019**, *123* (27), 16921–16928. https://doi.org/10.1021/acs.jpcc.9b05364.

(115) Karlsson, R. K. B.; Hansen, H. A.; Bligaard, T.; Cornell, A.; Pettersson, L. G. M. Ti Atoms in $Ru_{0.3}Ti_{0.7}O_2$ Mixed Oxides Form Active and Selective Sites for Electrochemical Chlorine Evolution. *Electrochim. Acta* **2014**, *146*, 733–740. https://doi.org/10.1016/j.electacta.2014.09.056.

(116) Exner, K. S.; Anton, J.; Jacob, T.; Over, H. Controlling Selectivity in the Chlorine Evolution Reaction over RuO_2-Based Catalysts. *Angew. Chem. Int. Ed.* **2014**, *53* (41), 11032–11035. https://doi.org/10.1002/anie.201406112.

(117) Exner, K. S.; Anton, J.; Jacob, T.; Over, H. Full Kinetics from First Principles of the Chlorine Evolution Reaction over a RuO_2 (110) Model Electrode. *Angew. Chem. Int. Ed.* **2016**, *55* (26), 7501–7504. https://doi.org/10.1002/anie.201511804.

(118) He, Z.; Chen, Y.; Santos, E.; Schmickler, W. The Pre‐exponential Factor in Electrochemistry. *Angew. Chem. Int. Ed.* **2018**, *57* (27), 7948–7956. https://doi.org/10.1002/anie.201800130.

(119) Exner, K. S. Controlling Stability and Selectivity in the Competing Chlorine and Oxygen Evolution Reaction over Transition Metal Oxide Electrodes. *ChemElectroChem* **2019**, *6* (13), 3401–3409. https://doi.org/10.1002/celc.201900834.

(120) Exner, K. S. Activity‐Stability Volcano Plots for Material Optimization in Electrocatalysis. *ChemCatChem* **2019**, *11* (14), 3234–3241. https://doi.org/10.1002/cctc.201900500.

(121) Kishor, K.; Saha, S.; Parashtekar, A.; Pala, R. G. S. Increasing Chlorine Selectivity through Weakening of Oxygen Adsorbates at Surface in Cu Doped RuO_2 during Seawater Electrolysis. *J. Electrochem. Soc.* **2018**, *165* (15), J3276–J3280. https://doi.org/10.1149/2.0361815jes.

(122) Kuznetsova, E.; Petrykin, V.; Sunde, S.; Krtil, P. Selectivity of Nanocrystalline IrO_2-Based Catalysts in Parallel Chlorine and Oxygen Evolution. *Electrocatalysis* **2015**, *6* (2), 198–210. https://doi.org/10.1007/s12678-014-0233-y.

(123) Kim, J.; Kwon, D.; Kim, K.; Hoffmann, M. R. Electrochemical Production of Hydrogen Coupled with the Oxidation of Arsenite. *Environ. Sci. Technol.* **2014**, *48* (3), 2059–2066. https://doi.org/10.1021/es4046814.

(124) Park, H.; Vecitis, C. D.; Hoffmann, M. R. Solar-Powered Electrochemical Oxidation of Organic Compounds Coupled with the Cathodic Production of Molecular Hydrogen. *J. Phys. Chem. A* **2008**, *112* (33), 7616–7626. https://doi.org/10.1021/jp802807e.

(125) Lim, T.; Jung, G. Y.; Kim, J. H.; Park, S. O.; Park, J.; Kim, Y.-T.; Kang, S. J.; Jeong, H. Y.; Kwak, S. K.; Joo, S. H. Atomically Dispersed Pt–N4 Sites as Efficient and Selective Electrocatalysts for the Chlorine Evolution Reaction. *Nat. Commun.* **2020**, *11* (1), 412. https://doi.org/10.1038/s41467-019-14272-1.

(126) Boehm, H.-P.; Schneider, M. Über die Hydroxylgruppen an der Oberfläche des Amorphen Siliciumdioxyds „Aerosil" und ihre Reaktionen. *Z. Anorg. Allg. Chem.* **1959**, *301* (5–6), 326–335. https://doi.org/10.1002/zaac.19593010516.

(127) Boehm, H.-P.; Schneider, M.; Arendt, F. Der Wassergehalt „getrockneter" Siliciumdioxyd-Oberflächen. *Z. Anorg. Allg. Chem.* **1963**, *320* (1–4), 43–53. https://doi.org/10.1002/zaac.19633200107.

(128) Peri, J. B. Infrared and Gravimetric Study of the Surface Hydration of γ-Alumina. *J. Phys. Chem.* **1965**, *69* (1), 211–219. https://doi.org/10.1021/j100885a032.

(129) Viganoò, R.; Taraszewska, J.; Daghetti, A.; Trasatti, S. The Point of Zero Charge of RuO_2 + IrO_2 Mixed Oxides. *J. Electroanal. Chem. Interfacial Electrochem.* **1985**, *182* (1), 203–209. https://doi.org/10.1016/0368-1874(85)85455-1.

(130) Kosmulski, M. Isoelectric Points and Points of Zero Charge of Metal (Hydr)Oxides: 50 Years after Parks' Review. *Adv. Colloid Interface Sci.* **2016**, *238*, 1–61. https://doi.org/10.1016/j.cis.2016.10.005.

(131) Kleijn, J. M.; Lyklema, J. Colloid-Chemical Properties of Ruthenium Dioxide in Relation to Catalysis of the Photochemical Generation of Hydrogen. *Colloid & Polymer Sci.* **1987**, *265* (12), 1105–1113. https://doi.org/10.1007/BF01417469.

(132) Kleijn, J. M.; Lyklema, J. The Electrical Double Layer on Oxides: Specific Adsorption of Chloride and Methylviologen on Ruthenium Dioxide. *J. Colloid Interface Sci.* **1987**, *120* (2), 511–522. https://doi.org/10.1016/0021-9797(87)90378-X.

(133) Kobayakawa, K.; Nakazawa, Y.; Ikeda, M.; Sato, Y.; Fujishima, A. Influence of the Density of Surface Hydroxyl Groups on TiO_2 Photocatalytic Activities. *Berichte der Bunsengesellschaft für physikalische Chemie* **1990**, *94* (12), 1439–1443. https://doi.org/10.1002/bbpc.199000056.

(134) Wu, C.-Y.; Tu, K.-J.; Deng, J.-P.; Lo, Y.-S.; Wu, C.-H. Markedly Enhanced Surface Hydroxyl Groups of TiO_2 Nanoparticles with Superior Water-Dispersibility for Photocatalysis. *Materials* **2017**, *10* (5), 566. https://doi.org/10.3390/ma10050566.

(135) Schindler, P. W.; Walti, E.; Furst, B. Role of Surface Hydroxyl Groups in Surface Chemistry of Metal Oxides. *Chimia* **1976**, *30* (2), 107–109.

(136) McCafferty, W. Determination of the Concentration of Surface Hydroxyl Groups on Metal Oxide Films by a Quantitative XPS Method. *Surf. Interface Anal.* **1998**, 16.

(137) Oosawa, Y.; Grätzel, M. Effect of Surface Hydroxyl Density on Photocatalytic Oxygen Generation in Aqueous TiO_2 Suspensions. *J. Chem. Soc., Faraday Trans. 1* **1988**, *84* (1), 197. https://doi.org/10.1039/f19888400197.

(138) Di Paola, A.; Bellardita, M.; Palmisano, L.; Barbieriková, Z.; Brezová, V. Influence of Crystallinity and OH Surface Density on the Photocatalytic Activity of TiO_2 Powders. *J. Photochem. Photobiol. A: Chem.* **2014**, *273*, 59–67. https://doi.org/10.1016/j.jphotochem.2013.09.008.

(139) Schindler, P. W.; Gamsjäger, H. Acid — Base Reactions of the TiO_2 (Anatase) — Water Interface and the Point of Zero Charge of TiO_2 Suspensions. *Kolloid-Z.u.Z.Polymere* **1972**, *250* (7), 759–763. https://doi.org/10.1007/BF01498568.

(140) Frei, H.; Fitzmaurice, D. J.; Graetzel, M. Surface Chelation of Semiconductors and Interfacial Electron Transfer. *Langmuir* **1990**, *6* (1), 198–206. https://doi.org/10.1021/la00091a032.

(141) Moser, J.; Grätzel, M. Photoelectrochemistry with Colloidal Semiconductors; Laser Studies of Halide Oxidation in Colloidal Dispersions of TiO_2 and α-Fe_2O_3. *Helv. Chim. Acta* **1982**, *65* (5), 1436–1444. https://doi.org/10.1002/hlca.19820650517.

(142) Rotzinger, F. P.; Kesselman-Truttmann, J. M.; Hug, S. J.; Shklover, V.; Grätzel, M. Structure and Vibrational Spectrum of Formate and Acetate Adsorbed from Aqueous Solution onto the TiO_2 Rutile (110) Surface. *J. Phys. Chem. B* **2004**, *108* (16), 5004–5017. https://doi.org/10.1021/jp0360974.

(143) Kosmulski, M. The Significance of the Difference in the Point of Zero Charge between Rutile and Anatase. *Adv. Colloid Interface Sci.* **2002**, *99* (3), 255–264. https://doi.org/10.1016/S0001-8686(02)00080-5.

(144) Stumm, W.; Morgan, J. J. *Aquatic Chemistry: Chemical Equilibria and Rates in Natural Waters*, 3rd ed.; Environmental science and technology; Wiley: New York, 1996.

(145) Dzombak, D. A.; Morel, F. M. M. *Surface Complexation Modeling: Hydrous Ferric Oxide*; Wiley: New York, 1990.

(146) Schindler, P. W.; Stumm, W. *Aquatic Surface Chemistry: Chemical Processes at the Particle-Water Interface.*; 1987.

(147) Rodríguez, R.; Blesa, M. A.; Regazzoni, A. E. Surface Complexation at the TiO_2(Anatase)/Aqueous Solution Interface: Chemisorption of Catechol. *J. Colloid Interface Sci.* **1996**, *177* (1), 122–131. https://doi.org/10.1006/jcis.1996.0012.

(148) Blesa, M. A.; Weisz, A. D.; Morando, P. J.; Salfity, J. A.; Magaz, G. E.; Regazzoni, A. E. The Interaction of Metal Oxide Surfaces with Complexing Agents Dissolved in Water. *Coord. Chem. Rev.* **2000**, *196* (1), 31–63. https://doi.org/10.1016/S0010-8545(99)00005-3.

(149) Geiger, S.; Kasian, O.; Mingers, A. M.; Nicley, S. S.; Haenen, K.; Mayrhofer, K. J. J.; Cherevko, S. Catalyst Stability Benchmarking for the Oxygen Evolution Reaction: The Importance of Backing Electrode Material and Dissolution in Accelerated Aging Studies. *ChemSusChem* **2017**, *10* (21), 4140–4143. https://doi.org/10.1002/cssc.201701523.

(150) Wang, Z.; Guo, X.; Montoya, J.; Nørskov, J. K. Predicting Aqueous Stability of Solid with Computed Pourbaix Diagram Using SCAN Functional. *Npj Comput. Mater.* **2020**, *6* (1), 160. https://doi.org/10.1038/s41524-020-00430-3.

(151) Hodnik, N.; Jovanovič, P.; Pavlišič, A.; Jozinović, B.; Zorko, M.; Bele, M.; Šelih, V. S.; Šala, M.; Hočevar, S.; Gaberšček, M. New Insights into Corrosion of Ruthenium and Ruthenium Oxide Nanoparticles in Acidic Media. *J. Phys. Chem. C* **2015**, *119* (18), 10140–10147. https://doi.org/10.1021/acs.jpcc.5b01832.

(152) Klyukin, K.; Zagalskaya, A.; Alexandrov, V. Role of Dissolution Intermediates in Promoting Oxygen Evolution Reaction at RuO_2 (110) Surface. *J. Phys. Chem. C* **2019**, *123* (36), 22151–22157. https://doi.org/10.1021/acs.jpcc.9b03418.

(153) Zagalskaya, A.; Alexandrov, V. Mechanistic Study of IrO_2 Dissolution during the Electrocatalytic Oxygen Evolution Reaction. *J. Phys. Chem. Lett.* **2020**, *11* (7), 2695–2700. https://doi.org/10.1021/acs.jpclett.0c00335.

(154) Kasian, O.; Grote, J.-P.; Geiger, S.; Cherevko, S.; Mayrhofer, K. J. J. The Common Intermediates of Oxygen Evolution and Dissolution Reactions during Water Electrolysis on Iridium. *Angew. Chem. Int. Ed.* **2018**, *57* (9), 2488–2491. https://doi.org/10.1002/anie.201709652.

(155) Maciá, M. D.; Herrero, E.; Feliu, J. M.; Aldaz, A. Formic Acid Self-Poisoning on Bismuth-Modified Stepped Electrodes. *J. Electroanal. Chem.* **2001**, *500* (1–2), 498–509. https://doi.org/10.1016/S0022-0728(00)00389-2.

(156) Metikoš-Huković, M.; Rešeti’c, A.; Gvozdić, V. Behaviour of Tin as a Valve Metal. *Electrochim. Acta* **1995**, *40* (11), 1777–1779. https://doi.org/10.1016/0013-4686(95)00243-8.

(157) Boggio, R.; Carugati, A.; Lodi, G.; Trasatti, S. Mechanistic Study of Cl_2 Evolution at Ti-Supported Co_3O_4 Anodes. *J. Appl. Electrochem.* **1985**, *15* (3), 335–349. https://doi.org/10.1007/BF00615986.

(158) Zhu, X.; Wang, P.; Wang, Z.; Liu, Y.; Zheng, Z.; Zhang, Q.; Zhang, X.; Dai, Y.; Whangbo, M.-H.; Huang, B. Co_3O_4 Nanobelt Arrays Assembled with Ultrathin Nanosheets as Highly Efficient and Stable Electrocatalysts for the Chlorine Evolution Reaction. *J. Mater. Chem. A* **2018**, *6* (26), 12718–12723. https://doi.org/10.1039/C8TA03689F.

(159) Singh, V.; Nagaiah, T. C. *In Situ* Incorporation of Cobalt Nanoclusters and Nitrogen into the Carbon Matrix: A Bifunctional Catalyst for the Oxygen Depolarized Cathode and Chlorine Evolution in HCl Electrolysis. *J. Mater. Chem. A* **2019**, *7* (16), 10019–10029. https://doi.org/10.1039/C9TA00675C.

(160) Wang, Y.; Wu, J.; Giammar, D. E. Kinetics of the Reductive Dissolution of Lead(IV) Oxide by Iodide. *Environ. Sci. Technol.* **2012**, *46* (11), 5859–5866. https://doi.org/10.1021/es2038905.

(161) Guo, D.; Robinson, C.; Herrera, J. E. Role of Pb(II) Defects in the Mechanism of Dissolution of Plattnerite (β-PbO_2) in Water under Depleting Chlorine Conditions. *Environ. Sci. Technol.* **2014**, *48* (21), 12525–12532. https://doi.org/10.1021/es502133k.

(162) Lin, Y.-P.; Valentine, R. L. The Release of Lead from the Reduction of Lead Oxide (PbO_2) by Natural Organic Matter. *Environ. Sci. Technol.* **2008**, *42* (3), 760–765. https://doi.org/10.1021/es071984w.

(163) Ham, K.; Hong, S.; Kang, S.; Cho, K.; Lee, J. Extensive Active-Site Formation in Trirutile $CoSb_2O_6$ by Oxygen Vacancy for Oxygen Evolution Reaction in Anion Exchange Membrane Water Splitting. *ACS Energy Lett.* **2021**, *6* (2), 364–370. https://doi.org/10.1021/acsenergylett.0c02359.

Chapter 3 Crystalline $CoSb_2O_6$ for Chlorine Evolution Reaction: Understanding the Catalytic Active Sites

Heng Dong[1], Xiaohan (Anita) Shao[2], Sean McBeath[3], William A. Tarpeh[2*], and Michael R. Hoffmann[1*]

[1] Linde Laboratories, California Institute of Technology, Pasadena, California 91125, USA

[2] Department of Civil and Environmental Engineering, Stanford University, Stanford, California, USA

[3] Department of Civil and Environmental Engineering, University of Massachusetts, Amherst, MA 01003, USA

[*]Corresponding authors:

William A. Tarpeh - wtarpeh@stanford.edu
Michael R. Hoffmann - mrh@caltech.edu

3.1 Abstract

Chlorine evolution reaction (CER) is a key reaction in electrochemical oxidation (EO) water treatment. The conventional anodes based on platinum group metals (PGMs) are prohibitively expensive, hindering their further application in EO systems. Crystalline cobalt antimonate ($CoSb_2O_6$) was recently identified as a promising alternative to the conventional anodes due to its high catalytic activity and excellent stability in acidic media. However, its catalytic site and mechanism have not been revealed yet. This study shed light on the catalytic site in crystalline $CoSb_2O_6$ anode by using scanning electrochemical microscopy (SECM) to compare the CER catalytic activities of a series of anode samples with different Sb/Co ratios. The results showed that Sb sites served as even more active catalytic sites than the Co sites. The varied Sb/Co ratios were also linked with slightly different chemical states of each element, leading to different CER selectivity in dilute chloride solutions. Both the counterintuitively high activity of Sb sites and the varied electronic states of the elements underscored the significance of the electronic interaction between Co and Sb.

3.2 Introduction

According to the World Health Organization, as late as in 2017, at least 1/3 of the world population still suffer from water-borne diseases due to inappropriate water sanitation[1]. Given the economical and topological limitations, conventional centralized water treatment and sanitation systems do not apply well in many rural regions[2]. On the other hand, electrochemical systems provide a decentralized route for onsite water sanitation and reuse[3]. Over the past decade, electrochemical oxidation (EO) systems have been successfully deployed in China, India, and South Africa to address the water sanitation problem. Chlorine evolution reaction (CER) is the core to the EO systems, where the electrochemically generated free chlorine is primarily responsible for the removal of organic wastes and ammonia[4] as well as deactivation of the pathogens[5].

The anode is key to the overall performance of the EO systems. Dimensionally stable anodes (DSAs), consisting of a Ti base and platinum group metal (PGM) oxides as the active coating layer, have been widely employed for CER catalysis in electrochemical wastewater treatment. However, their larger-scale application has been limited by the use of PGM oxides such as RuO_2 and IrO_2, which are only to the prohibitively expensive, but also suffer from long-term instability due to PGM dissolution[6].

As a result, researchers have been actively searching for noble-metal-free electrocatalysts for CER. Co_3O_4 nanobelt array electrodes were synthesized by hydrothermal methods as CER catalysts, which showed comparable catalytic CER activity to that of RuO_2[7]. The high activity of the Co_3O_4 nanobelt was attributed to its high surface area. Co-N-C nanocluster was also synthesized by pyrolyzing a Co-oxime complex to serve as a CER catalyst that showed high activity than RuO_2/TiO_2 electrode in 0.4 M HCl solution[8]. However, Co oxides are generally vulnerable to acidic conditions, which leads to short lifetime of the electrodes. On the other hand, PbO_2 has also been used for CER catalysis, but it is limited by high overpotentials and the reductive leaching of Pb^{2+} ions under open circuit conditions[9–12].

In recent years, metal antimonates have been considered to be promising alternatives for PGM-based electrodes due to their high catalytic activity, excellent stability and relatively low price[13,14]. The crystalline $CoSb_2O_x$ anode exhibited comparable CER catalytic activity to the state-of-art RuO_2-TiO_2 anodes and even better stability under anodic conditions[13]. However, considering that $CoSb_2O_6$ takes on a different crystalline structure from Co oxides, meaning that it is different from Sb-doped Co oxides in chemical nature, and that Sb oxides possess no intrinsic catalytic activity, the catalytic mechanisms of crystalline $CoSb_2O_x$ is still elusive. Attempts have been made to reveal the catalytic mechanism of amorphous $CoSb_2O_x$ for oxygen evolution reaction (OER), where the oxygen vacancy and Co(IV) species were identified to be the primary active sites[15]. However, similar features were not observed for the crystalline counterparts.

In this study, crystalline $CoSb_2O_x$ anodes with various Sb/Co ratios were fabricated and tested to compare the catalytic activities of Co and Sb sites in crystalline $CoSb_2O_6$ anode. The bulk and surface stoichiometries of the electrodes were examined with Energy dispersive spectrometry (EDS) and X-ray photoelectron spectroscopy (XPS), respectively, while the catalytic activities were studied by scanning electrochemical microscopy (SECM). This study also tried to shed light on the selectivity of $CoSb_2O_6$ anode for CER over OER in dilute chloride solution, which is another important factor to affect the EO wastewater treatment performance.

3.3 Methods

3.3.1 Electrode fabrication

Ti plates were cut into 1 cm × 2 cm pieces and degreased with acetone. Before performing electrodeposition, the native oxide layer on the Ti plates was removed by etching in boiling 10 wt% oxalic acid solution for an hour.

Mixed films of $Co(OH)_2$ and metallic Sb were electrochemically deposited onto the Ti plates as the precursor for $CoSb_2O_6$. Specifically, the electrodeposition was performed in an undivided three-electrode electrochemical cell with a commercial RuO_2-IrO_2-TiO_2/Ti counter electrode and a saturated calomel reference electrode (E = +0.244 V vs. SHE @ 25 °C). A solution containing 430 mM $CoCl_2$, 115 mM $K_2Sb_2(C_4H_2O_6)_2$, and 400 mM KNO_3 was used as the electrolyte, as modified from a previous study[16]. Films with different

Sb/Co ratios were reductively deposited at different applied potentials, and the total charge passed was controlled at 1 mAh for the deposition process.

The as-deposited films were rinsed with water, dried naturally in the air and then annealed at 600 °C for 6 h, with a ramping rate of 10 °C min^{-1}, to produce the crystalline $CoSb_2O_6$ films.

3.3.2 Material characterization

The morphology and bulk elemental composition of the electrodes were examined using a ZEISS 1550VP field emission scanning electron microscope (FE-SEM) equipped with an Oxford X-Max SDD energy dispersive X-ray spectrometer (EDS). The crystalline structures of the samples were characterized with a Rigaku Smartlab X-ray diffractometer with a Cu-Kα radiation (λ=1.5418 Å) source. The surface stoichiometry and chemical states of the elements were examined with a Surface Science M-Probe XPS system with an Al Kα monochromatic x-ray source. The pressure in the measurement chamber was controlled at ~1×10^{-9} Torr during measurement. The data was analyzed with CasaXPS software, and Shirley background was used when trying to quantify the XPS peak areas.

3.3.3 Electrochemical tests

The SECM was performed with a Biologic M470 scanning electrochemical workstation coupled with a Biologic SP 300 potentiostat. A Biologic SECM Ultra-micro electrode (UME) probe with a 10 μm Pt tip was used, and the probe was polished with sand paper prior to use. The electrochemical measurements were conducted in 5 M NaCl solution to ensure a ~100% Faradaic efficiency (FE) for CER, and glassy carbon (GC) was used as the counter electrode for both the tip and the sample. The setup is shown in Figure S3.1. A 50 μm × 50 μm area was taken for every measurement. The tip moved with a step size of 10 μm on both x and y directions, at a scan speed of 20 μm s^{-1}. To exclude the influence of sample topography on the measured current, the intermittent contact SECM (ic-SECM) mode was conducted, where the tip was controlled by piezo in z direction to maintain a constant distance of 1 μm to the surface of the sample. The vibration frequency of the tip was maintained 525 Hz.

The SECM was performed in Redox Competition (RC) regime[17], where both the tip and the underlying sample were applied a potential to catalyze CER (Figure S3.2). Specifically, the tip was applied +1.4 V vs. Ag/AgCl and the sample was applied +1.1 V vs. Ag/AgCl. The lower applied potential for the sample was to ensure a small CER current and that no chlorine gas bubble was formed. The sample activity was measured by comparing the tip current when the sample was applied an oxidation potential versus when the samples was sitting at open circuit potential. A larger difference indicates higher sample activity since it shows that the sample is competing hard with the tip for chloride. The data was processed with Biologic M470 software.

Attempts were also made to use specific activities, which denote the catalytic current densities normalized to electrochemically active surface areas (ECSAs), to characterize the catalytic activities of the anodes. Specifically, linear sweep voltammetry (LSV) was performed at a scan rate of 10 mV s^{-1} in an undivided three-electrode system with a Ti plate (2 cm × 3 cm) counter electrode and a saturated calomel reference electrode. Voltammograms were taken in both 5 M NaCl solution and 0.1 M H_2SO_4 solution to examine the catalytic activities for CER and OER, respectively.

ECSA was measured in 1 M H_2SO_4 based on a previously reported method[18]. Basically, the anodes were subjected to cyclic voltammetry (CV) in a 100 mV-wide potential window centering the open circuit potential (OCP), at scan rates of 5 mV s^{-1}, 10 mV s^{-1}, 25 mV s^{-1}, 50 mV s^{-1}, 100 mV s^{-1}, 200 mV s^{-1}, 400 mV s^{-1} and 800 mV s^{-1}, respectively. The measured current at the OCP was plotted against the scan rate to reveal the double layer capacitance, which was then converted to ECSA using a general specific capacitance value Cs = 0.035 mF cm^{-2} for 1 M H_2SO_4.

The CER catalytic selectivity over that for OER was examined by measuring the aqueous free chlorine (FC) concentration and calculating the FE for different samples. Specifically, the FC was measured in 30 mM NaCl solution. A 2 cm × 3 cm titanium plate was used as the counter electrode and a saturated calomel electrode was used as the reference electrode. All the samples had geometric surface areas of 20 cm^2, and for selectivity measurements, 20 mA constant current condition was adopted to ensure a geometric current density of 10 mA cm^{-2}. The FC concentration was measured by using DPD (N,N-diethyl-p-phenylenediamine) reagent (Hach method 10101 and 10102).

3.4 Results

3.4.1 Electrode characterization

Different Sb/Co ratios were produced by annealing $Co(OH)_2$/Sb films that were electrodeposited at different potentials (Figure S3.3). Generally, the Sb/Co dropped as the potential went more negative, consistent with previous reports. This was because the lower potential increased the FE for hydrogen evolution reaction (HER) with respect to the reduction of $K_2Sb_2(C_4H_2O_6)_2$ into metallic Sb.

On the other hand, the surface Sb/Co ratios were observed to be significantly higher than the bulk ratio (Figure 3.1), which agreed with the previous study[13]. Considering acid instability of Co species in acidic media, the enriched Sb at the surface might account for the acid stability of $CoSb_2O_6$ catalysts. However, the source of the stability still requires further study.

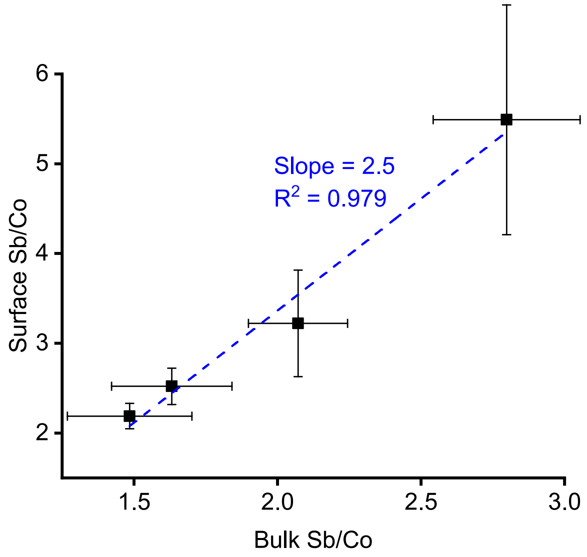

Figure 3.1. The comparison of surface and bulk Sb/Co ratios. The surface Sb/Co ratios were obtained by XPS, while the bulk ratios were obtained by EDS.

The $CoSb_2O_6$ samples generally take on a mudcrack-like morphology, and the width of the "cracks" generally increased as the ratio of Sb/Co drops (Figure S3.4). It was also interesting to notice the grape-like morphology in Co-rich samples. In the meantime, Co and Sb were uniformly distributed in the x and y directions (i.e., directions parallel to the sample surface plane) of the samples, as shown by EDS mapping (Figure S3.5). This also implied that the grape-like morphology was not caused by the cobalt oxides formed at the surface.

Despite the varied Sb/Co ratios, the samples generally maintained the rutile structure of $CoSb_2O_6$, consistent with previous studies (Figure S3.6a)[13]. However, it is worth noting that the crystallinity varied substantially with the stoichiometry. Specifically, no significant change in the XRD pattern was observed as the stoichiometry shifted from close-to-ideal (Sb/Co = 2.07) to Sb-rich (Sb/Co = 2.80). However, the samples became more amorphous as the Sb/Co ratio dropped. However, no distinct Co oxide phase was observed, indicating that the excessive Co and Sb were doped into the rutile lattices.

Since catalytic CER takes place at the electrode surface, the surface crystallinity of the samples was especially interesting for the catalytic activity. Grazing incidence XRD (GIXRD) was employed to reveal that the rutile structure was maintained at the catalyst surface (Figure S3.6b). The intensities of the GIXRD spectra were generally lower than the bulk XRD spectra because of the small incident angle (4° in this study) and therefore the small survey depth. Consistent with the bulk XRD results, Sb-rich samples had better rutile crystallinity, while Co-rich samples were more amorphous.

The chemical states of Co and Sb were studied by XPS (Figure 3.2). Co 2p 1/2 and 3/2 peaks were in the ranges of 780.6 – 780.7 eV and 796.6 – 796.7 eV, respectively. The Co 2p 1/2 peak position agreed well with the previously reported values for CoO, while the 2p 3/2 peak position was slightly more positive[19,20]. On the other hand, the Sb 3d 3/2 peak was observed in the range of 540.0 – 540.4 eV[21,22], which spanned the previously reported binding energies for both Sb_2O_3 and Sb_2O_5. Here Sb 3d 5/2 was not analyzed because of the serious overlap with O1s spectra. Considering that Co and Sb have nominal valences of +2 and +5 in $CoSb_2O_6$, it was interesting to note that the XPS signals of neither Co nor

Sb fully agreed with those of the individual metal oxides (CoO and Sb_2O_5). This indicated that both elements had altered electronic states compared to their individual metal oxides.

Meanwhile, we noticed that as the Sb/Co drops, the Co 2p peak positions shifted systematically towards being more positive, while the Sb peaks shifted towards being more negative. This indicated a potential electronic polarization between Co and Sb in the cobalt antimonate samples that either element got slightly more oxidized as it became more abundant.

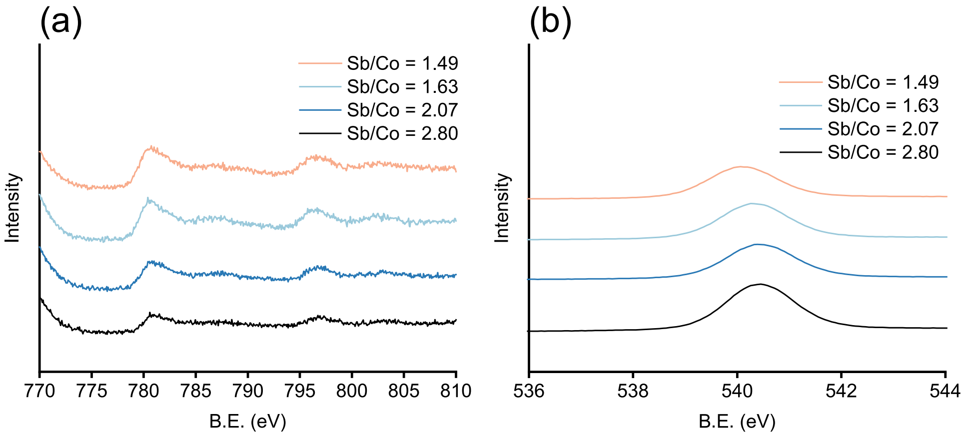

Figure 3.2. XPS spectra of (a) Co 2p and (b) Sb 3d 3/2 for various cobalt antimonate samples with different Sb/Co ratios.

3.4.2 SECM results

SECM was adopted in this study to compare the catalytic activities of the cobalt antimonate samples for CER. During the experiments, the tip-sample distance was kept constant at ~ 1 μm by the ic-SECM mode. This was not only to exclude the influence of sample topography on the measured tip current, but also to ensure that the tip was within the diffusion layer with regard to the sample surface. Based on that, the sample activity was gauged by comparing the tip current when an oxidation potential was applied to the sample versus when not.

The tip potential was determined based on the cyclic voltammograms obtained in the electrolyte with the sample sitting at OCP (Figure S3.7). A significant oxidative current showed that the tip was actively catalyzing CER at +1.4 V. On the other hand, a too high potential was not preferable since it might lead to bubble formation at the surface of the tip, which would seriously distort the results. As a result, +1.4 V was selected as the tip potential.

In contrast to the tip potential, the sample potential was carefully set to be close to the Nernstian potential (Figure S3.8), since, given the surface area of the sample, any larger potential may result in a current to produce enough chlorine that exceeds the solubility limit locally, and generate chlorine bubbles. When applied +1.1 V in 5 M NaCl solution, the sample initially produced an initial catalytic current of 0.35 mA. However, as the Nernstian potential rose with the aqueous chlorine concentration, the current quickly dropped to zero. This showed that +1.1 V was just slightly above the Nernstian potential for CER in fresh 5 M NaCl solution, and therefore it was selected as the sample potential.

The results of the SECM measurements were shown in Figure 3.3. It is interesting to note that the catalytic activities of the samples generally increased with the Sb content. However, the activities of the Sb/Co = 2.07 and the Sb/Co = 2.80 samples were very close, indicating that the activity might be insensitive to the stoichiometry in a certain stoichiometry window.

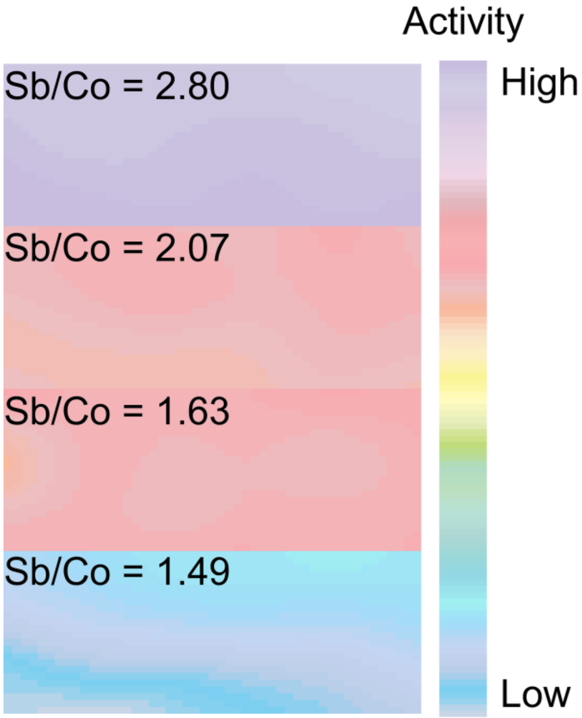

Figure 3.3. SECM mapping of cobalt antimonates with different Sb/Co ratios.

The selectivity of the electrodes for CER over OER in dilute chloride solutions was also examined by measuring the FC and FE (Figure 3.4). It was intriguing to observe that the change of FE with the stoichiometry was not monotonic. The Sb/Co = 2.07 sample had the highest cumulative FE of 40 ± 2% in 15 min, followed by Sb/Co = 1.63 (34 ± 5%), Sb/Co = 2.80 (31 ± 1%) and Sb/Co = 1.49 (26 ± 7%).

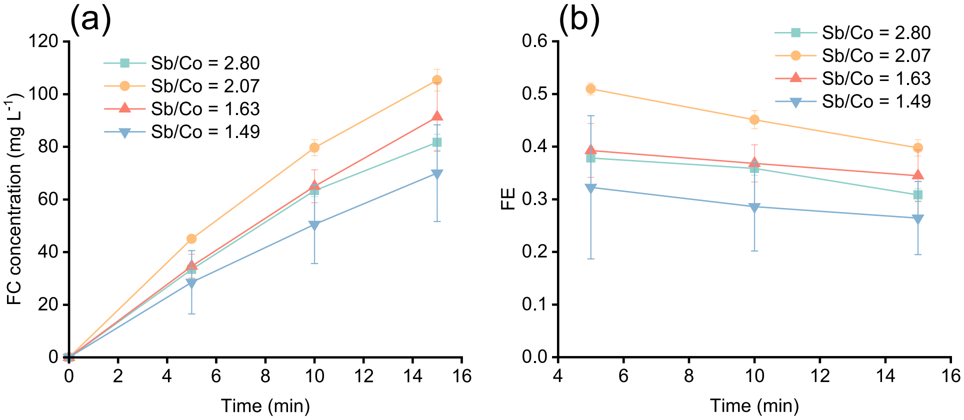

Figure 3.4. Evolution of (a) FC concentration and (b) FE over time. The electrolyte was 30 mM NaCl solution and the applied current was 20 mA for all samples.

3.5 Discussion

3.5.1 Is the Co site or the Sb site more active?

As a promising alternative to the conventional PGM-based catalysts, $CoSb_2O_6$ system has been employed by various works for OER[14,16] and CER[13] catalysis. Revealing the catalytic sites is key to further improving the catalytic activity. Ham et al. used electron spin resonance (ESR), X-ray absorption near-edge structure (XANES) analysis and CV to propose that Co(IV) species and oxygen vacancy were responsible for the catalytic activity in amorphous $CoSb_2O_6$[15]. However, they noted that the mechanism did not apply for the crystalline counterparts, and the catalytic site for crystalline $CoSb_2O_6$ remains unknown.

To ensure the validity of the comparison, it was important to control any other factor that may contribute to different catalytic performance, such as crystalline structures, surface heterogeneity, and influence of mass transport conditions. For crystalline structure, XRD showed that all the samples with different Sb/Co ratios possessed rutile structure both at the surface and in the bulk. At the same time, EDS maps showed that Co and Sb were uniformly distributed at the sample surface. Lastly, SECM with an UME tip was used to exclude potential mass transport limitation on the activity measurement. Contrary to the conclusion by Ham et al. about amorphous $CoSb_2O_6$, the SECM results showed that Sb sites were generally more active catalytic sites than the Co sites. This is highly interesting since antimony oxides are traditionally believed not to be active catalysts. The activity of the Sb sites was believed to originate from the electronic interaction between Co and Sb in crystalline $CoSb_2O_6$. Similar effects were not observed in amorphous systems because the influence of Co on Sb atoms was likely not to be systematic. Considering the surface segregation of Sb in $CoSb_2O_6$ and the leaching of Co under acidic pH conditions, the top Sb layer might be the reason that crystalline $CoSb_2O_6$ served as a CER catalyst to couple catalytic activity with stability in acidic environment.

We discovered that the conventional activity measurement tools, such as LSV, failed to provide objective comparison of the catalytic performances across different samples because the results were skewed by mass transport limitation and sample topology differences. The specific activities, which denoted the catalytic current densities normalized to the ECSAs, were shown in Figure S3.9, with the corresponding ECSAs shown in Figure S3.10. For both CER (tested in 5 M NaCl) and OER (tested in 1 M H_2SO_4), the samples with lower ECSAs (Sb/Co = 2.80 and Sb/Co = 1.49) showed substantially higher specific activities than those with higher ECSAs (Sb/Co = 2.07 and Sb/Co = 1.63), which was ascribed to the bubble formation at the sample surface. The specific activity test may have unfairly favored the samples with smaller ECSAs because fewer bubbles were present at the sample surface to block the mass transport of both the reactant and the product during the LSV measurement. As a result, the samples with smaller ECSAs "made better use" of the catalytic sites, and the specific activities generally followed the reverse order of ECSA. However, an exception was observed for the most Co-rich sample (Sb/Co = 1.49) with respect to the most Sb-rich sample (Sb/Co = 2.80). The difference was attributed to the different morphologies, where the Sb/Co = 1.49 sample had substantially larger cracks. According to previous studies, the morphology was favorable for bubble release during CER and OER[23], thereby enhancing the specific activity.

We do not argue that Sb is the only catalytic site in crystalline $CoSb_2O_6$. However, this study shows the significance of the electronic interaction between Co and Sb, whose presence was confirmed by XPS (Figure 3.2). Similar effect was reported in RuO_2-TiO_2 anodes, where TiO_2, after getting electronically tuned by RuO_2, has been proposed as an even more active catalytic site than RuO_2 based on both experimental[24] and computational evidence[25,26]. The electronic interaction is well worth further investigation. By turning the normally believed "stabilizer elements" (e.g. Ti in RuO_2-TiO_2 and Sb in $CoSb_2O_6$) into active catalytic sites, this provides solutions to couple catalytic activity with stability.

3.5.2 What impacts the selectivity for CER?

Despite that the selectivity for CER over OER is one of the most important indicators for electrochemical water treatment performance, the intertwined mechanisms of the two reactions make it difficult to create electrodes that are highly selective for CER even in dilute chloride solutions. As reported by various computational studies, CER and OER share important intermediate species, so their free energy barriers often change synchronously when the catalyst materials are varied[27–29]. However, it is still possible to achieve highly selective CER by lowering the free energy barrier for CER while raising that for OER. According to the computational studies, this requires the fine-tuning of the adsorption energy of the catalyst surfaces for some of the key intermediates, such as $\Delta E(O^c)$[30].

With this said, the selectivity differences of the samples were attributed to the different electronic states of Co and Sb atoms, as revealed by XPS (Figure 3.2). As the chemical states of the elements changed with the electrode stoichiometry, it was expected that the adsorption energy for oxygen- and chlorine-containing intermediate species was also adjusted. The highest selectivity of Sb/Co = 2.07 sample indicated that the electronic states of the Co and Sb were optimal to produce the largest free energy barrier difference between CER and OER. This indicated that varying the stoichiometry in $CoSb_2O_6$ systems may not only change the ratio of the two catalytic sites, but also slightly modified the properties of each catalytic center. This again further highlights the importance of electronic interaction between the metal elements.

3.6 Acknowledgements

The authors acknowledge generous financial support from Bill and Melinda Gates Foundation (Grant No. INV047212).

3.7 Supplementary information

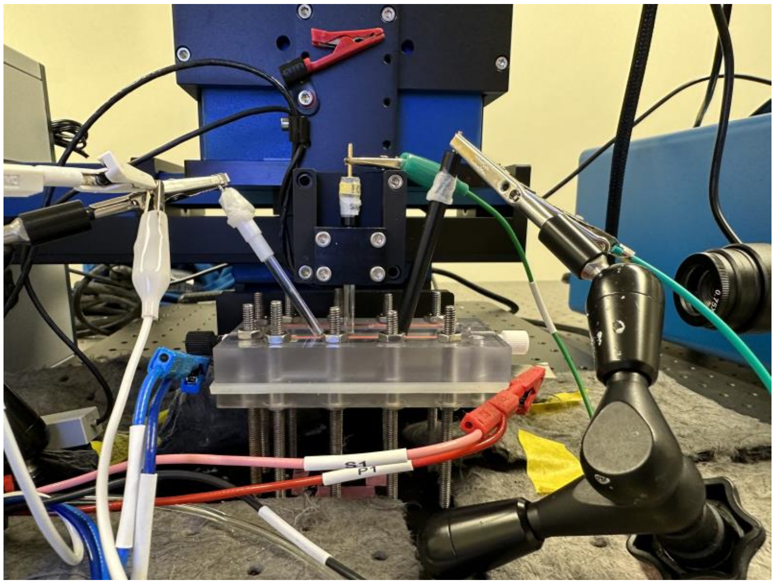

Figure S 3.1. The experimental setup used for SECM tests.

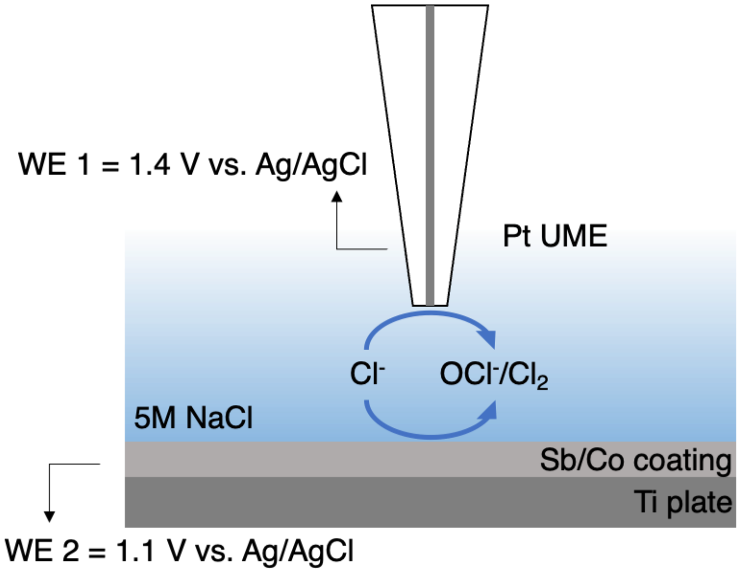

Figure S 3.2. The RC regime adopted for the SECM measurement.

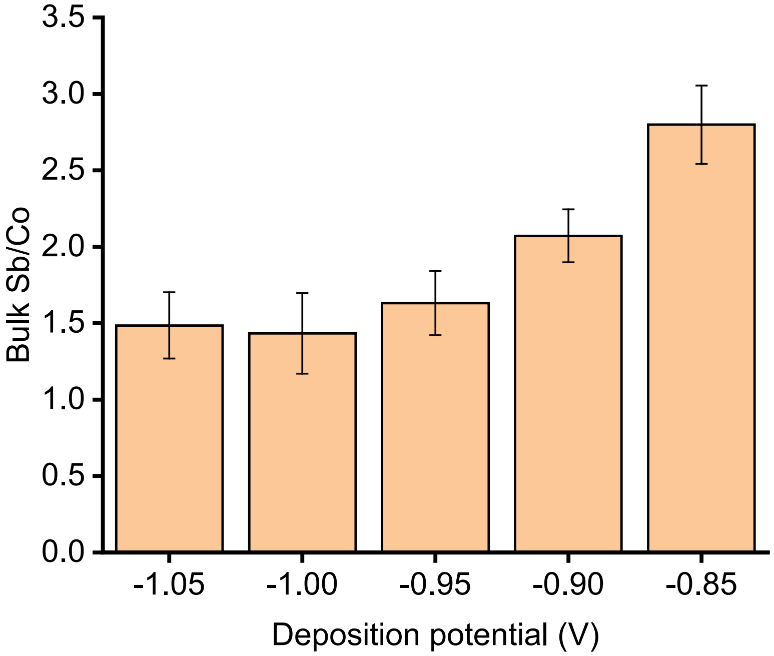

Figure S 3.3. The bulk Sb/Co ratios for samples deposited at different potentials. The bulk Sb/Co ratios were obtained using EDS.

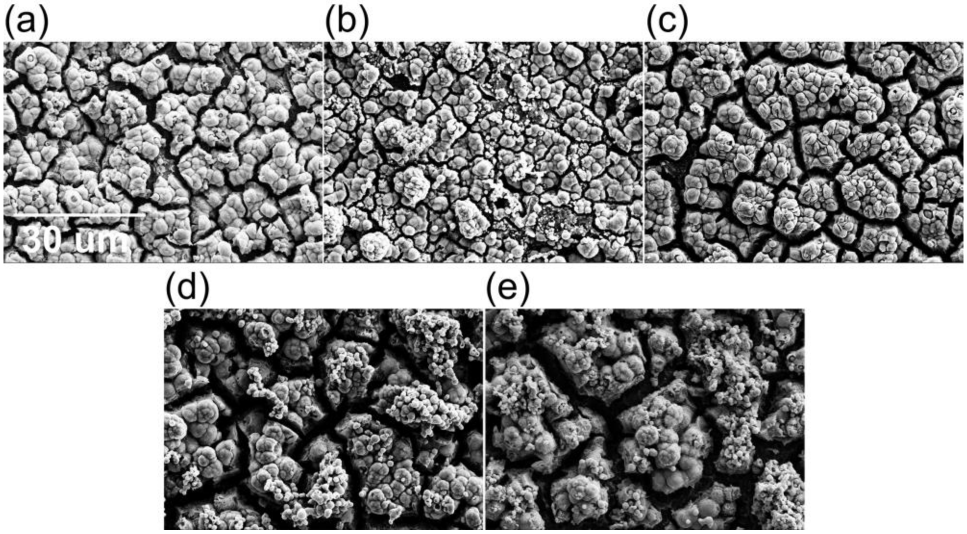

Figure S 3.4. SEM pictures of samples that were derived from electrodeposited $Co(OH)_2$/Sb films at (a) -0.85 V, (b) -0.90 V, (c) -0.95 V, (d) -1.00 V, and (e) -1.05 V. All potentials were versus saturated calomel electrode.

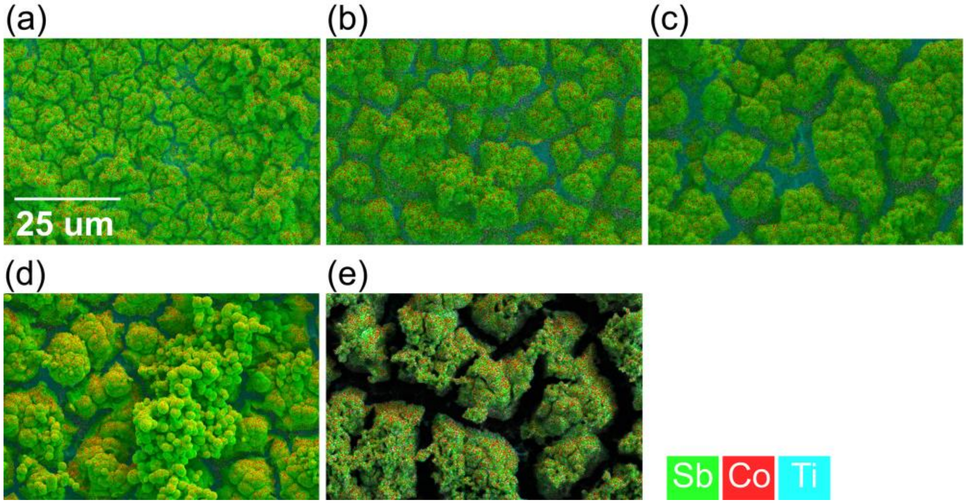

Figure S 3.5. EDS mapping of the samples that were derived from electrodeposited $Co(OH)_2$/Sb films at (a) -0.85 V, (b) -0.90 V, (c) -0.95 V, (d) -1.00 V, and (e) -1.05 V. All potentials were versus saturated calomel electrode. Co and Ti were uniformly distributed in the samples.

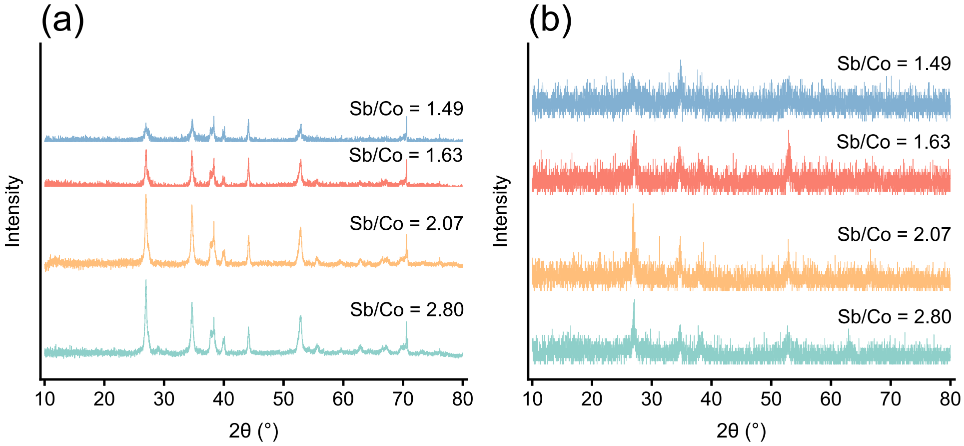

Figure S 3.6. Crystal structures of the cobalt antimonate samples with various Sb/Co ratios revealed by (a) bulk phase and (b) grazing incidence XRD. For GIXRD, the incidence angle was kept 4° for all the samples.

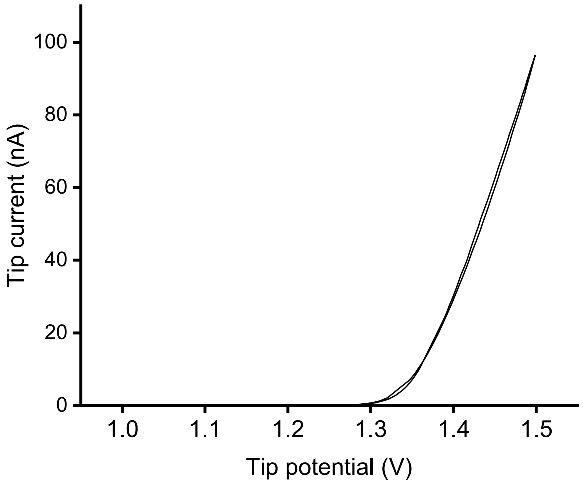

Figure S 3.7. Cyclic voltammograms of the SECM tip in 5 M NaCl solution. The sample was sitting at OCP during the cyclic voltammetry.

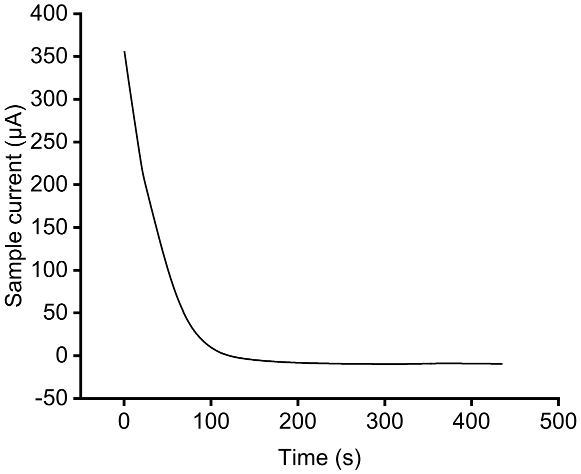

Figure S 3.8. The current of the sample in SECM under an applied potential of +1.1 V. The tip was sitting far from the sample and not applied a potential during this measurement.

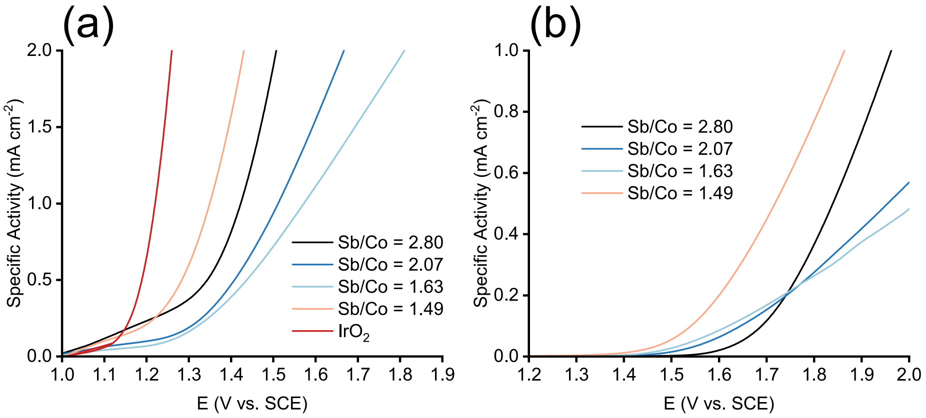

Figure S 3.9. The specific activities of the different samples in (a) 5 M NaCl, and (b) 0.1 M H_2SO_4 solutions.

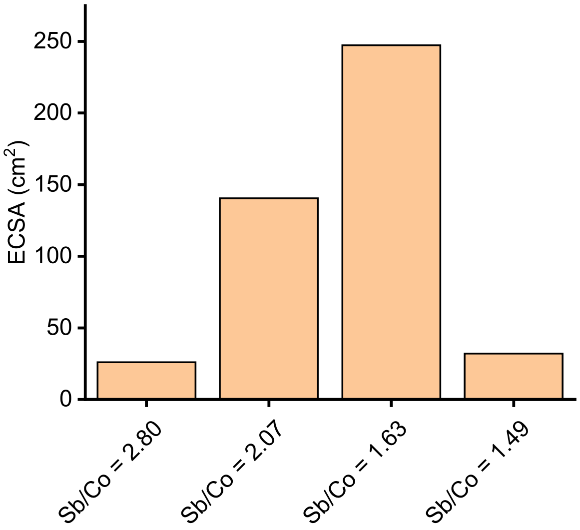

Figure S 3.10. The ECSA of samples with different Sb/Co ratios. The geometric surface areas of the samples were 2 cm^2.

References

(1) World Health Organization. *Sanitation*. https://www.who.int/news-room/fact-sheets/detail/sanitation.

(2) Massoud, M. A.; Tarhini, A.; Nasr, J. A. Decentralized Approaches to Wastewater Treatment and Management: Applicability in Developing Countries. *J. Environ. Manage.* **2009**, *90* (1), 652–659. https://doi.org/10.1016/j.jenvman.2008.07.001.

(3) Li, Y.; Zhang, Y.; Xia, G.; Zhan, J.; Yu, G.; Wang, Y. Evaluation of the Technoeconomic Feasibility of Electrochemical Hydrogen Peroxide Production for Decentralized Water Treatment. *Front. Environ. Sci. Eng.* **2021**, *15* (1), 1. https://doi.org/10.1007/s11783-020-1293-2.

(4) Yang, Y.; Shin, J.; Jasper, J. T.; Hoffmann, M. R. Multilayer Heterojunction Anodes for Saline Wastewater Treatment: Design Strategies and Reactive Species Generation Mechanisms. *Environ. Sci. Technol.* **2016**, *50* (16), 8780–8787. https://doi.org/10.1021/acs.est.6b00688.

(5) Huang, X.; Qu, Y.; Cid, C. A.; Finke, C.; Hoffmann, M. R.; Lim, K.; Jiang, S. C. Electrochemical Disinfection of Toilet Wastewater Using Wastewater Electrolysis Cell. *Water Res.* **2016**, *92*, 164–172. https://doi.org/10.1016/j.watres.2016.01.040.

(6) Dong, H.; Yu, W.; Hoffmann, M. R. Mixed Metal Oxide Electrodes and the Chlorine Evolution Reaction. *J. Phys. Chem. C* **2021**, *125* (38), 20745–20761. https://doi.org/10.1021/acs.jpcc.1c05671.

(7) Zhu, X.; Wang, P.; Wang, Z.; Liu, Y.; Zheng, Z.; Zhang, Q.; Zhang, X.; Dai, Y.; Whangbo, M.-H.; Huang, B. Co_3O_4 Nanobelt Arrays Assembled with Ultrathin Nanosheets as Highly Efficient and Stable Electrocatalysts for the Chlorine Evolution Reaction. *J. Mater. Chem. A* **2018**, *6* (26), 12718–12723. https://doi.org/10.1039/C8TA03689F.

(8) Singh, V.; Nagaiah, T. C. *In Situ* Incorporation of Cobalt Nanoclusters and Nitrogen into the Carbon Matrix: A Bifunctional Catalyst for the Oxygen Depolarized Cathode and Chlorine Evolution in HCl Electrolysis. *J. Mater. Chem. A* **2019**, *7* (16), 10019–10029. https://doi.org/10.1039/C9TA00675C.

(9) Zeradjanin, A. R.; Menzel, N.; Strasser, P.; Schuhmann, W. Role of Water in the Chlorine Evolution Reaction at RuO_2 -Based Electrodes-Understanding Electrocatalysis as a Resonance Phenomenon. *ChemSusChem* **2012**, *5* (10), 1897–1904. https://doi.org/10.1002/cssc.201200193.

(10) Lin, Y.-P.; Valentine, R. L. The Release of Lead from the Reduction of Lead Oxide (PbO_2) by Natural Organic Matter. *Environ. Sci. Technol.* **2008**, *42* (3), 760–765. https://doi.org/10.1021/es071984w.

(11) Guo, D.; Robinson, C.; Herrera, J. E. Role of Pb(II) Defects in the Mechanism of Dissolution of Plattnerite (β-PbO_2) in Water under Depleting Chlorine Conditions. *Environ. Sci. Technol.* **2014**, *48* (21), 12525–12532. https://doi.org/10.1021/es502133k.

(12) Wang, Y.; Wu, J.; Giammar, D. E. Kinetics of the Reductive Dissolution of Lead(IV) Oxide by Iodide. *Environ. Sci. Technol.* **2012**, *46* (11), 5859–5866. https://doi.org/10.1021/es2038905.

(13) Moreno-Hernandez, I. A.; Brunschwig, B. S.; Lewis, N. S. Crystalline Nickel, Cobalt, and Manganese Antimonates as Electrocatalysts for the Chlorine Evolution Reaction. *Energy Environ. Sci.* **2019**, *12* (4), 1241–1248. https://doi.org/10.1039/C8EE03676D.

(14) Moreno-Hernandez, I. A.; MacFarland, C. A.; Read, C. G.; Papadantonakis, K. M.; Brunschwig, B. S.; Lewis, N. S. Crystalline Nickel Manganese Antimonate as a Stable Water-Oxidation Catalyst in Aqueous 1.0 M H_2SO_4. *Energy Environ. Sci.* **2017**, *10* (10), 2103–2108. https://doi.org/10.1039/C7EE01486D.

(15) Ham, K.; Hong, S.; Kang, S.; Cho, K.; Lee, J. Extensive Active-Site Formation in Trirutile $CoSb_2O_6$ by Oxygen Vacancy for Oxygen Evolution Reaction in Anion Exchange Membrane Water Splitting. *ACS Energy Lett.* **2021**, *6* (2), 364–370. https://doi.org/10.1021/acsenergylett.0c02359.

(16) Evans, T. A.; Choi, K.-S. Electrochemical Synthesis and Investigation of Stoichiometric, Phase - Pure $CoSb_2O_6$ and $MnSb_2O_6$ Electrodes for the Oxygen Evolution Reaction in Acidic Media. *ACS Appl. Energy Mater.* **2020**, *3* (6), 5563–5571. https://doi.org/10.1021/acsaem.0c00526.

(17) Zeradjanin, A. R.; Schilling, T.; Seisel, S.; Bron, M.; Schuhmann, W. Visualization of Chlorine Evolution at Dimensionally Stable Anodes by Means of Scanning Electrochemical Microscopy. *Anal. Chem.* **2011**, *83* (20), 7645–7650. https://doi.org/10.1021/ac200677g.

(18) McCrory, C. C. L.; Jung, S.; Peters, J. C.; Jaramillo, T. F. Benchmarking Heterogeneous Electrocatalysts for the Oxygen Evolution Reaction. *J. Am. Chem. Soc.* **2013**, *135* (45), 16977–16987. https://doi.org/10.1021/ja407115p.

(19) Tan, B. J.; Klabunde, K. J.; Sherwood, P. M. A. XPS Studies of Solvated Metal Atom Dispersed (SMAD) Catalysts. Evidence for Layered Cobalt-Manganese Particles on Alumina and Silica. *J. Am. Chem. Soc.* **1991**, *113* (3), 855–861. https://doi.org/10.1021/ja00003a019.

(20) Okamoto, Y. Surface Structure of CoO-MoO_3/Al_2O_3 Catalysts Studied by X-Ray Photoelectron Spectroscopy. *J. Catal.* **1980**, *65* (2), 448–460. https://doi.org/10.1016/0021-9517(80)90322-X.

(21) Wang Jianqi; Feng Daming; Wu Wenhui; Zeng Minxiu; Li Yiz. An Investigation of the Flame Retardation Mechanism of Polypropylene Containing a Chlorine Flame Retardant System by XPS(ESCA). *Polym. Degrad. Stab.* **1991**, *31* (2), 129–140. https://doi.org/10.1016/0141-3910(91)90069-4.

(22) Izquierdo, R.; Sacher, E.; Yelon, A. X-Ray Photoelectron Spectra of Antimony Oxides. *Appl. Surf. Sci.* **1989**, *40* (1–2), 175–177. https://doi.org/10.1016/0169-4332(89)90173-6.

(23) Zeradjanin, A. R.; Topalov, A. A.; Van Overmeere, Q.; Cherevko, S.; Chen, X.; Ventosa, E.; Schuhmann, W.; Mayrhofer, K. J. J. Rational Design of the Electrode Morphology for Oxygen Evolution – Enhancing the Performance for Catalytic Water Oxidation. *RSC Adv.* **2014**, *4* (19), 9579. https://doi.org/10.1039/c3ra45998e.

(24) Finke, C. E.; Omelchenko, S. T.; Jasper, J. T.; Lichterman, M. F.; Read, C. G.; Lewis, N. S.; Hoffmann, M. R. Enhancing the Activity of Oxygen-Evolution and Chlorine-Evolution Electrocatalysts by Atomic Layer Deposition of TiO_2. *Energy Environ. Sci.* **2019**, *12* (1), 358–365. https://doi.org/10.1039/C8EE02351D.

(25) Karlsson, R. K. B.; Hansen, H. A.; Bligaard, T.; Cornell, A.; Pettersson, L. G. M. Ti Atoms in $Ru_{0.3}Ti_{0.7}O_2$ Mixed Oxides Form Active and Selective Sites for

Electrochemical Chlorine Evolution. *Electrochim. Acta* **2014**, *146*, 733–740. https://doi.org/10.1016/j.electacta.2014.09.056.

(26) Exner, K. S.; Anton, J.; Jacob, T.; Over, H. Controlling Selectivity in the Chlorine Evolution Reaction over RuO_2 -Based Catalysts. *Angew. Chem. Int. Ed.* **2014**, *53* (41), 11032–11035. https://doi.org/10.1002/anie.201406112.

(27) Sumaria, V.; Krishnamurthy, D.; Viswanathan, V. Quantifying Confidence in DFT Predicted Surface Pourbaix Diagrams and Associated Reaction Pathways for Chlorine Evolution. *ACS Catal.* **2018**, *8* (10), 9034–9042. https://doi.org/10.1021/acscatal.8b01432.

(28) Hansen, H. A.; Man, I. C.; Studt, F.; Abild-Pedersen, F.; Bligaard, T.; Rossmeisl, J. Electrochemical Chlorine Evolution at Rutile Oxide (110) Surfaces. *Phys. Chem. Chem. Phys.* **2010**, *12* (1), 283–290. https://doi.org/10.1039/B917459A.

(29) Exner, K. S.; Anton, J.; Jacob, T.; Over, H. Microscopic Insights into the Chlorine Evolution Reaction on RuO_2(110): A Mechanistic Ab Initio Atomistic Thermodynamics Study. *Electrocatalysis* **2015**, *6* (2), 163–172. https://doi.org/10.1007/s12678-014-0220-3.

(30) Exner, K. S. Controlling Stability and Selectivity in the Competing Chlorine and Oxygen Evolution Reaction over Transition Metal Oxide Electrodes. *ChemElectroChem* **2019**, *6* (13), 3401–3409. https://doi.org/10.1002/celc.201900834.

Chapter 4 Heterojunction Ni–Sb–SnO_2 Reactive Electrochemical Membrane for Domestic Wastewater and Greywater Treatment

Heng Dong, Parker Deptula, Nicolas Jimenez-Lozano, Yi Zhang, Clément A. Cid,
Léopold Dobelle*, and Michael R. Hoffmann*

Linde Laboratories, California Institute of Technology, Pasadena, California 91125, USA

*Corresponding authors:

Léopold Dobelle - ldobelle@caltech.edu
Michael R. Hoffmann - mrh@caltech.edu

4.1 Abstract

The world still faces serious water pollution and water sanitation issues. Electrochemical oxidation (EO) has been demonstrated to be a feasible decentralized water treatment technology to address these issues, and the electrode is a key for both the treatment performance and the energy consumption of EO systems. Herein we developed a Ni–Sb–SnO_2 reactive electrochemical membrane (REM) for high-performance and energy-efficient treatment of primary effluent and greywater. In 30 min, the REM removed up to 78 ± 2% COD and 94 ± 0.6% turbidity from the primary effluent. The REM had ~100% COD removal and 89 ± 4% turbidity removal from greywater, with the effluent meeting the NSF/ANSI 350 standard. When the volume was cut to about a half, the REM achieved fast removal of 93 ± 4% turbidity in 5 min. The internal cycling mode of REM was found to not only enhance the treatment performance, but also lower the energy consumption. REM showed better treatment performance and higher energy efficiency than the conventional plate-type electrode, demonstrating the importance of macroscopic electrode structure and morphology on the performance of EO systems.

4.2 Introduction

The lack of safe water supply has been an increasing threat, especially for developing countries and regions. According to World Health Organization (WHO), as late as in 2020, 10% the world population is believed to consume food irrigated by wastewater and at least 2 billion people globally use a drinking water source contaminated by feces[1,2]. Limited by both the economical and topological factors, traditional centralized water treatment plants are not applicable for many poor, remote and mountainous areas because the pipeline system cannot be successfully constructed or well maintained[3,4]. In this context, decentralized water treatment technologies have gained popularity over the years as an ideal alternative. By keeping the treatment units close to the wastewater source, the decentralized treatment units provide point-of-generation treatment and often recycle the treated water for non-potable reuse. Because of its independence from pipeline systems and often, electrical grid power, decentralized treatment systems feature high flexibility and are applied especially well in regions with low population density[4].

Many technologies have been employed in decentralized water treatment, including septic tanks, constructed wetlands, membrane processes, electrochemical technologies, etc[3–5]. Among these, electrochemical technologies have attracted considerable attention given their small footprints, modular design, environmental compatibility and ease of automation[6]. Furthermore, electrochemical oxidation (EO) systems have been demonstrated to be feasible for treating and recycling human wastewater[6] as well as producing valuable by-products[7–9] and removing trace contaminants[10]. For example, IrO_2-Ta_2O_5 based multi-layer anode achieved over 95% chemical oxygen demand (COD) and ammonia removal from domestic wastewater in 6 h[11]. NaCl dosage was observed to substantially increase the treatment efficiency. In the meantime, IrO_2-Ta_2O_5 based multilayer heterojunction anodes also achieved complete removal of COD and ammonia from the human wastewater in 4 h with minor NaCl dosing[6], demonstrating the potential of EO to be used in decentralized water treatment systems.

The electrode is key to the performance of EO systems, and a large volume of work has been performed to optimize both the electrode material and the macroscopic structures to enhance the treatment performance and lower the energy consumption. In terms of electrode materials, both “active” anode materials such RuO_2 and IrO_2, and “non-active” anode materials like boron doped diamond (BDD) and antimony doped tin oxide (Sb-SnO_2) catalyzed effective pollutant degradation and pathogen deactivation from wastewater[12].

Non-active anodes generally require higher applied potentials to achieve a similar current density than “active” anodes, because of their higher overpotential for oxygen evolution reaction (OER) and chlorine evolution reaction (CER). However, the higher overpotential also enables them to catalyze more advanced oxidation reactions, such as electrochemical production of ozone, hydroxyl radicals and even direct electron transfer with the aqueous pollutants, at substantially higher Faradaic efficiency (FE)[13]. As a result, for direct treatment of raw wastewater or septic tank effluent, non-active anodes feature faster COD removal and less energy consumption than active anodes[14]. We have recently reported a two-layer heterojunction Ni–Sb–SnO_2 anode that achieved more efficient organic compound destruction and pathogen deactivation in wastewater. The energy consumption was also lower than previously reported values obtained with other electrodes[15].

Separately, the macroscopic electrode structures can also be tuned to facilitate the mass transport and enhance the treatment performance. The porous magnéli phase Ti_4O_7 electrochemical membrane has gained considerable attention as an emerging electrode to degrade and mineralize a series of refractory aqueous pollutants including oxalic acid[16], perfluorooctanoic acid (PFOA)[17] and perfluorooctanesulfonic acid (PFOS)[17,18]. The excellent performance was attributed to not only the magnéli phase Ti_4O_7, but also the porous membrane structure that facilitated the mass transport[16]. Similar porous Sb-SnO_2 electrodes have also been used to degrade aqueous pyridine and antiretroviral drug stavudine[19,20]. However, the potential of such porous anodes in treating actual wastewater has not been fully demonstrated yet.

In this work, we combine the two-layer heterojunction Ni–Sb–SnO_2 electrode material with a porous membrane electrode structure to create reactive electrochemical membrane (REM) anodes that achieve fast and effective treatment of both grey water and primary effluent with relatively small energy input. COD and turbidity were employed to characterize the water quality, and the wastewater treatment process was evaluated based on both the contaminant abatement and the energy consumption.

4.3 Methods

4.3.1 Treatment scenarios

Three treatment scenarios were studied.

Scenario I: treatment of household domestic wastewater after simple biological pre-treatment. This scenario is often encountered in practice where EO systems collect and treat the household wastewater from septic tanks. We have previously studied this scenario using a multilayer heterojunction Ir-based electrode[6].

Scenario II: treatment of household greywater for non-potable reuse, where greywater refers to domestic wastewater generated from baths, showers, hand basins, washing machines, dishwashers and kitchen sinks, but not toilets[21]. The treated water is usually recycled for non-potable use or discharged into natural water bodies. The decentralized treatment system, by locally recycling part of the household waste, contributed to water conservation at the household level. This also reduces the waste input into the centralized sewage system, reducing the overall water treatment cost.

Scenario III: treatment of greywater from vehicles for toilet flushing reuse ("portable greywater treatment"). For vehicles such as recreational vehicles, vessels or airplanes, on-board recycling of the greywater not only reduces the environmental footprint, but also reduces the amount of water that needs to be carried, minimizing both water and fuel consumption.

4.3.2 Wastewater preparation

The greywater was prepared based on the NSF/ANSI 350-2012 standard (Table S4.1), and the typical water quality of the greywater was shown in Table S4.2. Primary effluent was used in this study to simulate the domestic wastewater after simple biological pre-treatment. The primary effluent, as well as the secondary effluent used for greywater preparation, was collected from San Jose Water Reclamation Plant.

4.3.3 Electrochemical cell setup

Two-electrode systems were adopted for all the scenarios. The REM anode and tubular stainless-steel cathode (shown in Figure S4.1) used in this study were purchased from Yixing Entrustech Environmental Co., Ltd. The microphone-shape REM, which consists of a porous Ti substrate and the mixed metal oxide coating as we reported[15], had a length of 10 cm and a diameter of 3 cm (Figure S4.1a). The anode was empty inside to allow for flow-through treatment. The outer geometric surface area was calculated to be 81 cm^2. On the other hand, the tubular stainless-steel cathode had an inner diameter of 3.8 cm. The cathode had 3 mm holes to allow the water to flow through. For all scenarios studied, the cathode was placed outside the cathode as shown in Figure S4.2, and the distance between the electrodes was kept 4 mm.

For Scenario I and II, a cylindrical reactor was used (Figure S4.1c), where the REM anode was mounted at the center of the reactor through the reactor bottom (shown also in Figure S4.2), and the cathode enveloped the anode from the top. For Scenario III, a smaller reactor was used but the electrode layout was kept the same.

Conventional plate-type electrodes, also supplied by Yixing Entrustech Environmental Co., Ltd., were used in this study as control. The plate-type electrodes also consist of a Ti substrate and the same mixed metal oxide coating as REM, and the geometric surface area of the plate-type electrode were controlled to be 80 cm^2, which was comparable to that of an REM. A stainless-steel sheet was used as the cathode for the plate-type electrodes, and the anode-cathode distance was also 4 mm.

4.3.4 Electrochemical characterization

Electrochemically active surface area (ECSA) was measured to compare the REM with the plate-type electrodes. The measurement was conducted in 1 M NaOH solution following a previously reported method[22].

4.3.5 Wastewater electrolysis

For Scenario I and II, 600 mL primary effluent and 600 mL synthetic greywater were used, respectively. For these two scenarios, the REM was applied a constant current of 5A, and the voltages were recorded at pre-determined time intervals to determine the energy consumption. The REM were tested under both static and internal-cycling modes. For the internal-cycling mode, the wastewater was pumped by a NE-9000B pump (New Era Pump Systems, Inc., Farmingdale, USA) to flow out of the reactor bottom through the REM and then return to the system from the top.

For Scenario III, 315 mL synthetic greywater was used as the electrolyte considering the small amount of greywater generated on vehicles compared to households. Besides, the treatment experiments were performed by keeping the power, instead of the current, constant.

For all three scenarios, the REM was powered using a CHUX s-6000 power supply (CHUX, Yueqing, Zhejiang Province, China). To simulate practical wastewater treatment, the reactor was not stirred.

The COD was measured according to the Hach Method 8000 with a DR 900 Colorimeter (Hach, Loveland, USA). The turbidity was measured by a HI93414 Turbidity meter (Hanna Instruments, Woonsocket, USA). pH was measured using an Orion 8157BNUMD Ross Ultra pH/ATC Triode (Thermo Scientific, Waltham, USA) connected to an Orion Star A215 pH/conductivity meter (Thermo Scientific, Waltham, USA).

4.4 Results & Discussion

4.4.1 Electrochemical characterization of the REMs and plate-type anodes

Despite the macroscopically porous structure of REM, it surprisingly had only about one third of the ECSA compared to plate-type electrodes (Figure S4.3). This was attributed to the combination of two factors. First, the plate-type electrodes fabricated by thermal deposition has long been known to have roughness factors on the order of 10^2, leading to high ECSAs. Second, although the REM had a porous structure, the inner surface area might not be directly accessible because of mass transport limitation, considering that the ECSA was measured under static conditions.

4.4.2 Scenario I: decentralized domestic wastewater treatment

Both the REM and plate-type electrode had over 70% COD removal in 30 min with an applied current of 5 A (Figure 4.1a). Specifically, internal cycling rate of 500 mL min^{-1} and 150 mL min^{-1} gave REM the similarly best performance, removing 78 ± 2% and 78 ± 5% COD in 30 min, respectively. This was followed by REM with 20 mL min^{-1} internal cycling (76 ± 3%). When the reactor was under static condition, the COD reduction was 72 ± 6% for the REM and 71 ± 9% for the plate-type electrode. Higher internal cycling flow rate led to better COD removal performance because of the better mass transport, in agreement with previous studies[16]. Meanwhile, higher flow rate also generally reduced the variation of the treatment data. Considering that stirring is not feasible in real-world water treatment systems, the internal cycling mode of REM is expected to ensure the consistency of effluent water quality.

In contrast to the dramatic difference in the ECSAs, the REM had similar performance to the plate-type electrode in removing COD under static conditions. This indicated that the plate-type electrode could not “take full use” of its catalytic sites because of the mass transport limitation under static conditions.

To understand the filtration effect on the wastewater treatment by REM, a series of primary effluent treatment experiments were conducted where the wastewater was constantly filtrated but only electrochemically treated intermittently (Figure 4.1b). With only mechanical filtration, there was 31% COD reduction in 30 min, and 39% removal in 60 min. The COD reduction gradually plateaued as the adsorption capacity was reached. This again highlighted that the internal cycling greatly enhanced the mass transport of organic contaminants to the REM electrode. On the other hand, when the system was only powered half of the time, ~70% COD was reduced in 60 min.

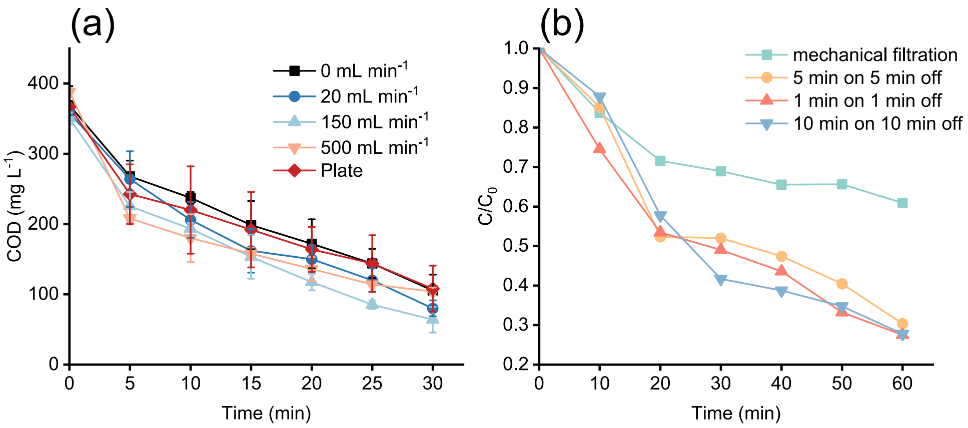

Figure 4.1. COD removal from primary effluent by REM and the plate-type electrode. (a) COD removal from primary effluent by REM with different internal cycling rates (0 mL min^{-1} denotes static condition), and the plate-type electrode; (b) influence of internal cycling conditions on the COD removal by the REM. The flow rate was controlled at 150 mL min^{-1}.

REM showed much higher turbidity removal form primary effluent than plate-type electrodes (Figure 4.2). Even without internal cycling, REM reduced the turbidity of primary effluent from 92.3 ± 6.8 NTU to 13.6 ± 3.3 NTU (85% reduction) in 30 min, substantially higher than the removal by plate-type electrodes (40.0 ± 2.2 NTU, 57% reduction). Furthermore, internal cycling rates of 20 mL min^{-1}, 150 mL min^{-1} and 500 mL min^{-1}, led to final turbidities of 5.7 ± 0.6 NTU (94 ± 0.6% removal), 7.0 ± 0.8 NTU (92 ± 0.9% removal) and 6.5 ± 0.8 NTU (93 ± 0.9% removal), respectively. Consistent with the COD reduction, internal cycling mode not only facilitated turbidity removal, but also minimized the variation in the water quality of the effluent.

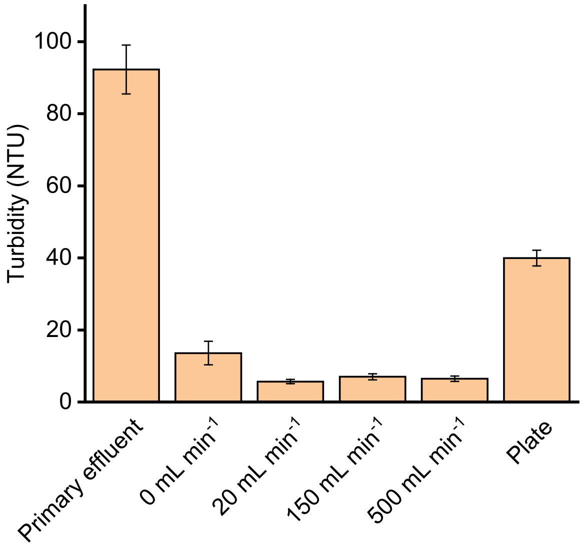

Figure 4.2. Turbidity of primary effluent before and after 30-min electrochemical treatment.

The voltages during the treatment are shown in Figure 4.3a. Plate-type electrode system had significantly higher voltages than the REM system. As a result, under constant current conditions, the REM could achieve even better wastewater treatment results with significantly less power consumption.

In terms of different internal cycling rates, the voltages of REM system increased with the internal cycling rate. This was due to that higher flow rate enhanced the mass transport so that the REM had higher FE for direct electron transfer with the pollutants, which required higher applied potential than OER and CER at the same current density.

Interestingly, the voltages generally decreased over the treatment time. This was due to either increasing conductivity in the wastewater or due to the elevating temperature. To determine the root cause, the conductivity was measured during the treatment (Figure S4.4). There was an initial dip in the conductivity because of consumption of chloride by CER. The conductivity then gradually increased as the organic contaminants were degraded into carboxylic acids[23] or mineralized into inorganic salts. However, it was clear that the conductivity after 20 min of treatment was lower than the initial value, inconsistent with the observation that the 20-min voltage was much lower than the 0-min one. On the other hand, the water temperature rose from room temperature to ~50 °C after the 30-min treatment, so we attribute the decrease in voltage to Joule heating. On the other hand, based on the conductivity measurement, dosing the wastewater with inorganic salts was found to substantially lower the voltages during the treatment, as well as the energy consumption (Figure S4.5).

The energy consumption for water treatment is further quantified in Figure 4.3b. Generally, the energy consumption with respect to unit COD removal increased with time. This was because of the pseudo-first order kinetics of electrochemical pollutant degradation as revealed by previous research[15,24], which meant that, with a constant power input, the COD decreased more slowly as the water became less polluted. The REM had a 30-min cumulative energy consumption of 268 ± 31 kWh kg^{-1} COD, 22% lower than the plate-type electrode the plate-type electrode (344 ± 61 kWh kg^{-1} COD). Remembering that the REM and the plate-type electrode had identical catalyst coating, this again highlights the significance of the REM structure in boosting the wastewater treatment performance while minimizing the energy consumption.

Despite the increasing voltage with the internal cycling flow rates, higher flow rates resulted in lower energy consumption. This implied that the enhancement of treatment performance outcompeted the increased voltages.

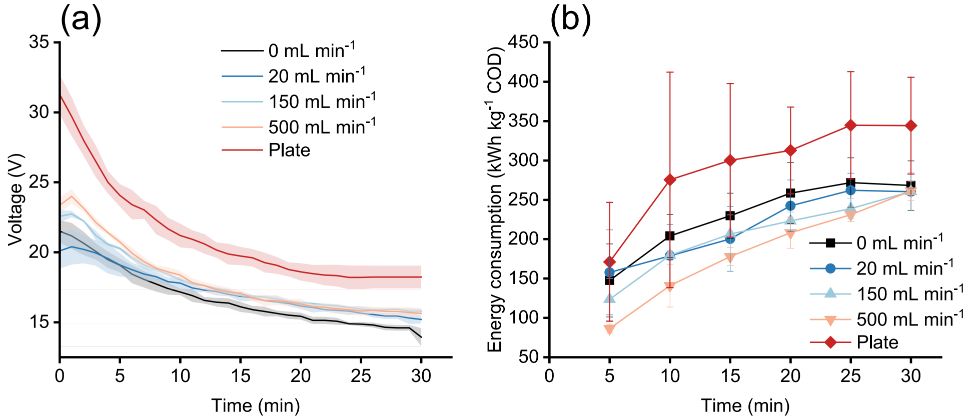

Figure 4.3. Evolution of (a) voltages and (b) cumulative energy consumptions for 600 mL primary effluent treatment under different conditions.

4.4.3 Scenario II: decentralized household greywater treatment

The REM successfully treated the synthetic greywater to a level that fulfilled the NSF/ANSI 350 standard Class R systems (single family residential dwelling) requirements (Figure 4.4). Specifically, with an internal cycling flow rate of 500 mL min^{-1}, the REM reduced the COD from 316 ± 27 mg L^{-1} to 1 ± 1 mg L^{-1} in 30 min, removing ~100% the COD from the synthetic greywater. At the same time, it also brought down the turbidity from 57 ± 4 NTU to 6 ± 2 NTU (89 ± 4% removal), meeting the NSF/ANSI 350 standard requirement.

Consistent with the primary effluent treatment, higher internal cycling flow rates generally led to better treatment results. Internal cycling flow rates of 150 mL min^{-1} and 20 mL min^{-1} led to 30-min COD removal of 88% (from 342 ± 5 mg L^{-1} to 40 ± 16 mg L^{-1}) and 81% (from 338 ± 6 mg L^{-1} to 63 ± 30 mg L^{-1}), respectively, both higher than the static condition (71% removal in 30 min, from 308 ± 6 mg L^{-1} to 63 ± 30 mg L^{-1}). This again illustrates that the internal cycling enhanced the treatment performance by facilitating the mass transport.

It was worth noting that the plate-type electrode had a better performance in greywater treatment compared to primary effluent treatment, achieving 86% COD removal in 30 min (from 313 ± 18 mg L^{-1} to 45 ± 31 mg L^{-1}). This was due to the fact that greywater, compared to domestic wastewater, contains high amounts of anionic surfactants, that were electrochemically drawn to the anode during the treatment. As a result, the performance of plate-type electrodes was less limited by mass transport. The higher treatment of plate-type electrode than the REM under static conditions agreed with its higher ECSA. However, the performance was still outcompeted by the REM with 500 mL min^{-1} internal cycling.

Consistent with the primary treatment results, the REM showed excellent turbidity removal (Figure 4.4b) from greywater. Under static conditions, the REM achieved 72% turbidity removal (from 57 ± 4 NTU to 16 ± 2 NTU) in 30 min, higher than the removal by plate-type electrode (56%, from 57 ± 4 NTU to 25 ± 2 NTU). Internal cycling rates of 20 mL min^{-1} and 150 mL min^{-1} both led to 93% turbidity removal.

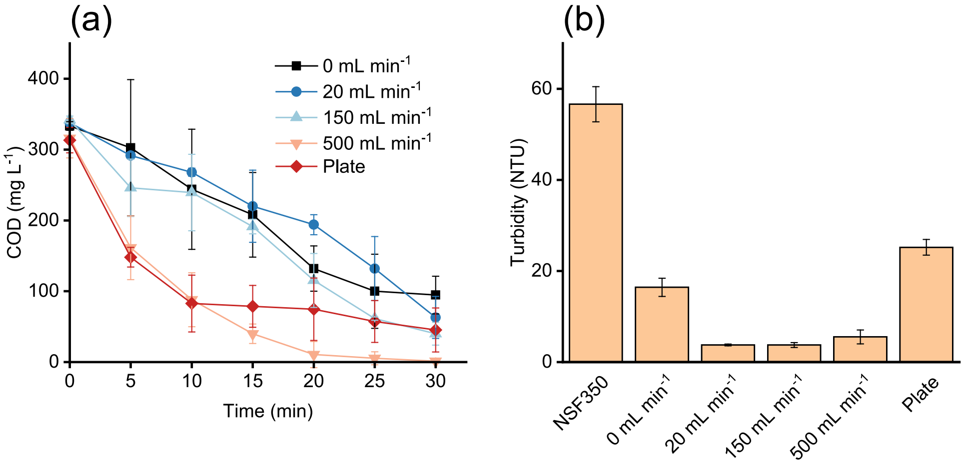

Figure 4.4. Removal of (a) COD and (b) turbidity from greywater by REM and the plate-type electrodes under various conditions.

In terms of energy consumption, the REM still had a notably lower voltage than the plate-type electrode under constant 5 A current condition (Figure 4.5a). Additionally, increasing internal cycling flow rates also elevated the treatment voltage. However, different from the primary treatment, increasing flow rates only slightly decreased the 30-

min cumulative energy consumption with respect to COD removal (Figure 4.5b). Specifically, internal cycling rates of 0 mL min^{-1}, 20 mL min^{-1}, 150 mL min^{-1} and 500 mL min^{-1} corresponded to 30-min cumulative energy consumption of 314 ± 34 kWh kg^{-1} COD, 291 ± 18 kWh kg^{-1} COD, 277 ± 6 kWh kg^{-1} COD and 275 ± 25 kWh kg^{-1} COD. This was likely due to the better intrinsic mass transport of the pollutants in greywater than in primary effluent. Still, the energy consumption was considerably lower than the plate-type electrode system (491 ± 95 kWh kg^{-1} COD).

Consistent with the primary effluent treatment, higher internal cycling flow rates not only promoted the water treatment performance, but also reduced the variation of the treatment results. Given the excellent treatment performance and the reasonable energy consumption, the internal-cycling-mode REM system was demonstrated to be a compact, portable, green yet powerful solution to septic tank effluent and greywater treatment and recycling for a single household. Combining the results from Scenario I and II, it is easy to discover that REM, with the internal cycling mode, presented an electrochemical wastewater treatment solution that is not only more powerful, but also more energy-efficient, than conventional plate-type electrodes. Considering that they had identical catalyst coating, this also highlights the importance of macroscopic morphology and structure for the performance of the electrodes.

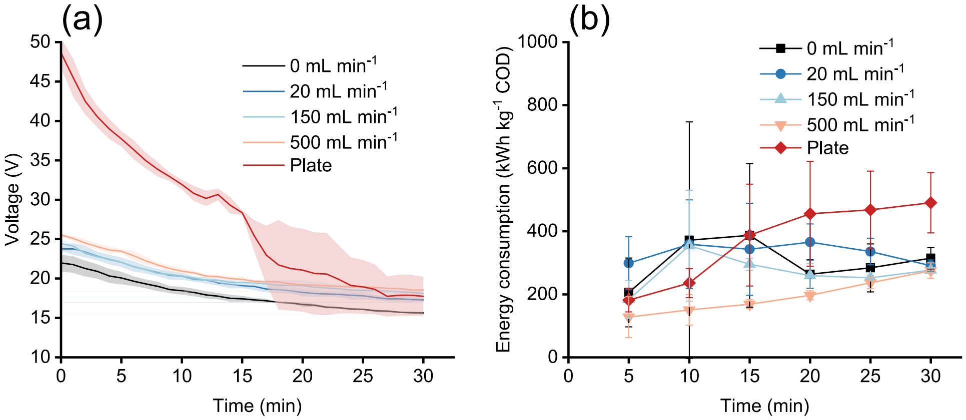

Figure 4.5. Evolution of (a) Voltages and (b) cumulative energy consumptions for 600 mL greywater treatment under different conditions.

4.4.4 Scenario III: portables greywater treatment

Apart from wastewater treatment for single households, the application of the REM in vehicles such as ships and airplanes was also explored. Different from households, these situations feature high-frequency generation of small-amount greywater such as handwashing wastewater, as well as absence of water reservoirs to store the treated water. On the other hand, there is also often high-frequency demand for toilet flushing, which the treated greywater is used for. As a result, fast treatment of small amount (315 mL batch) of greywater by REM was studied here. For the simplicity of the system, only static treatment was studied.

Similar to Scenario II, the REM achieved efficient treatment for the greywater (Figure 4.6). In 5 min, the REM achieved 38% (from 328 ± 8 mg L^{-1} to 206 ± 5 mg L^{-1}) and 67% (from 327 ± 7 mg L^{-1} to 107 ± 20 mg L^{-1}) COD removal with 100 W and 200 W applied power, respectively (Figure 4.6a). The increase in applied power had a substantial effect on the COD removal. On the other hand, however, the turbidity removal in 5 min only increased from 88 ± 0.4% (from 52 ± 2 NTU to 6 ± 0.2 NTU) to 93 ± 4% (from 56 ± 4 NTU to 4 ± 2 NTU) with the increasing power. With a smaller volume of greywater, the REM could achieve an excellent turbidity removal even without internal cycling.

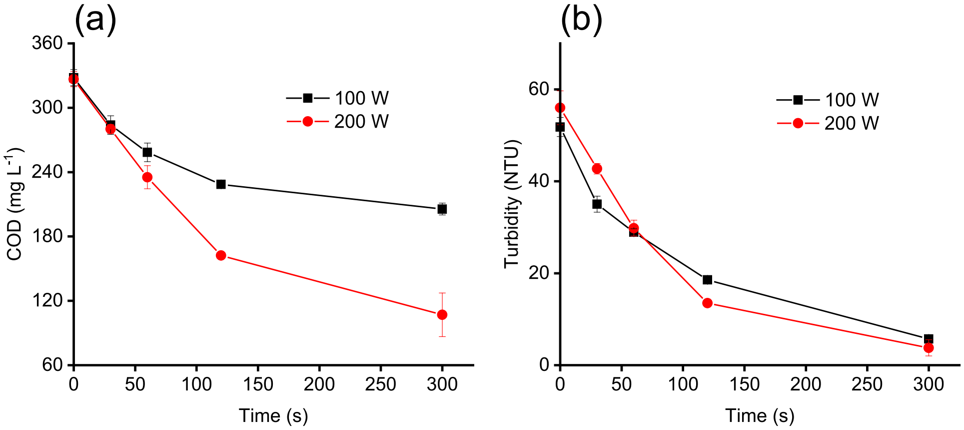

Figure 4.6. Degradation of (a) COD and (b) turbidity over 5 min of greywater treatment by REM with 100 W and 200 W power, respectively.

Similarly to the previous two scenarios, the cumulative energy consumption of the treatment also increased over time (Figure 4.7). An applied power of 100 W led to lower energy consumption with respect to the COD removal. In 5 min, the cumulative energy consumption was 216 ± 3 kWh kg^{-1} COD for an applied power of 100 W, and 229 ± 3 kWh kg^{-1} COD for 200 W. The values were consistent with Scenario II, but the variation of the data was considerably smaller. This was likely to be due to the smaller greywater volume. In terms of being reused for toilet flushing at a high frequency, the turbidity of the treated water might be the prioritized concern. Remembering that 100 W and 200 W produced similarly low-turbidity effluent, 100 W might be the more optimal condition for treatment of vehicle greywater by the REM for toilet flushing.

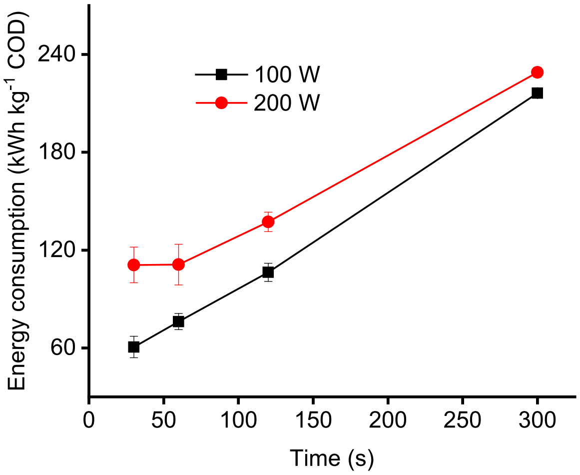

Figure 4.7. The cumulative energy consumption for 315 mL greywater treatment by the REM as a function of treatment time and applied power.

4.5 Conclusion

This study developed a Ni–Sb–SnO_2 REM as a compact, powerful, green and versatile system to be successfully applied in a series of wastewater treatment scenarios. The REM system was demonstrated to reduce both the COD and turbidity of primary effluent in 30 min to allow it to be recycled. The REM also managed to treat household greywater in 30 min to a level required by NSF/ANSI 350 standard. These showed the potential of the REM system to be deployed in single households for decentralized wastewater treatment and recycling. Additionally, it also succeeded in removing turbidity in 5 min from greywater, showing that it’s a promising solution for recycling the greywater on vehicles for toilet flushing. The internal cycling mode of REM was found to not only enhance the treatment performance, but also lower the energy consumption. With the internal cycling of the wastewater, REM showed better treatment performance and higher energy efficiency for both primary effluent and greywater treatment than conventional plate-type electrode.

4.6 Acknowledgement

The authors acknowledge generous financial support from the Bill and Melinda Gates Foundation (Grant No. INV047212) and Safran.

4.7 Supplementary information

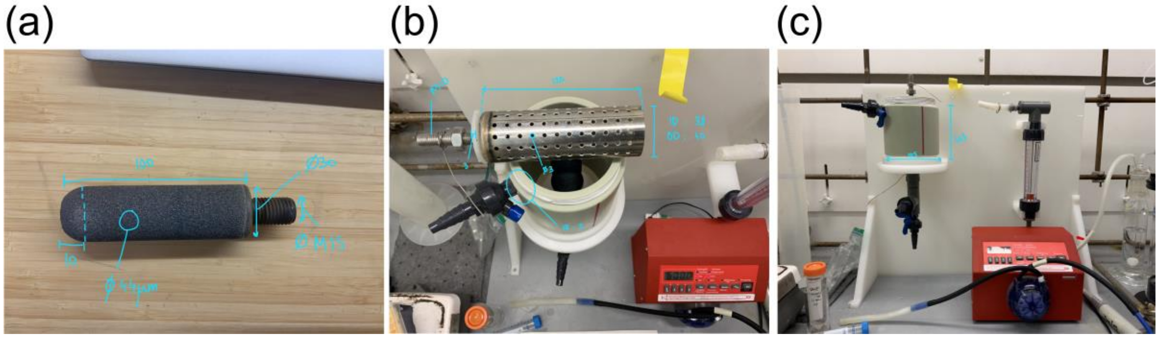

Figure S 4.1. Photos of the (a) REM and the (b) stainless-steel cathode; (c) the cylindrical reactor used for Scenario I and II treatment.

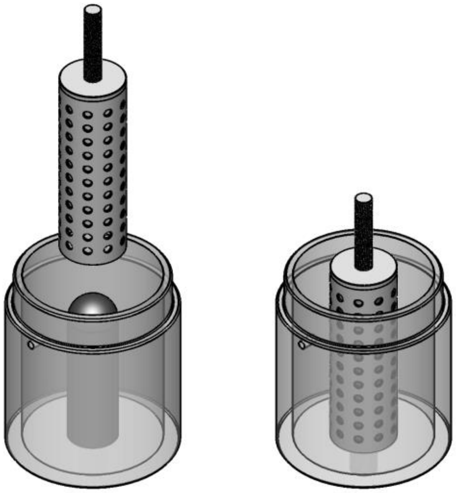

Figure S 4.2. Scheme showing the positions of the REM and the cathode during treatment. The anode-cathode distance was kept constantly at 4 mm.

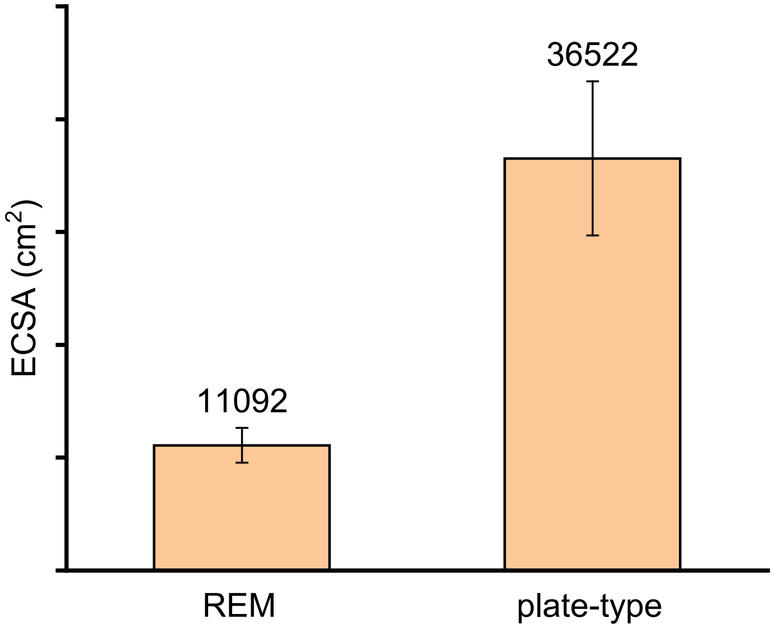

Figure S 4.3. The ECSA measured for both REM and the plate-type electrode. The geometric surface areas were 81 cm^2 for REM and 80 cm^2 for the plate-type electrode.

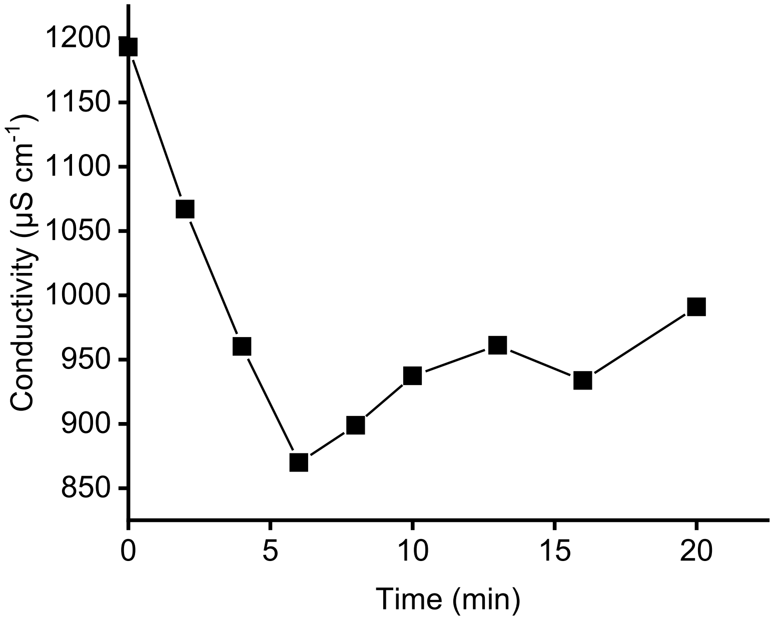

Figure S 4.4. Evolution of conductivity of the primary effluent over 20 min of electrochemical treatment by REM. The applied current was 5 A and the internal cycling rate was 150 mL min^{-1}.

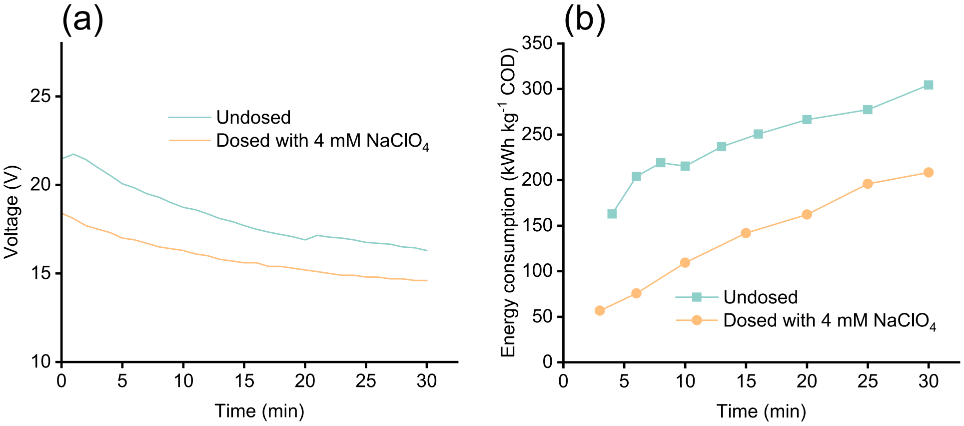

Figure S 4.5. Effect of dosing the primary effluent with 4 mM $NaClO_4$ on the treatment voltages and energy consumption by the REM. The internal cycling rate was 150 mL min^{-1}.

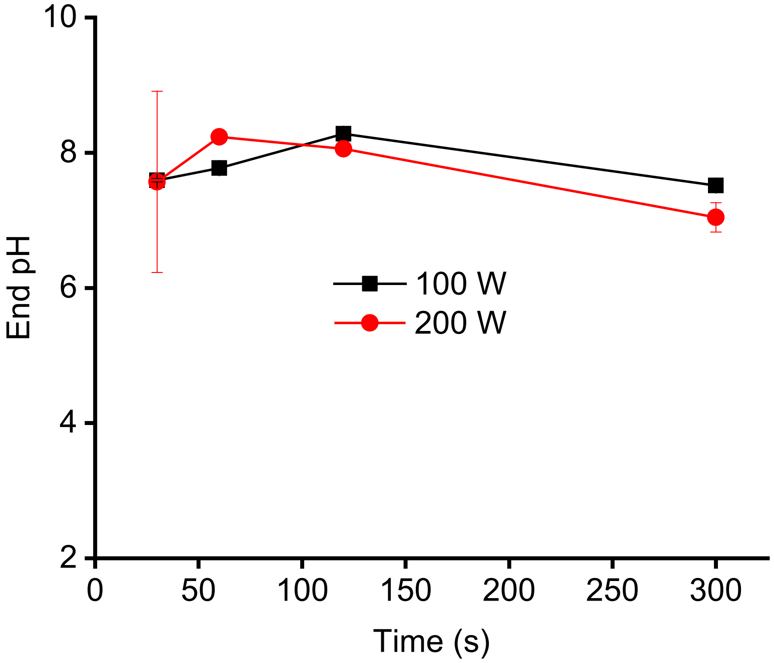

Figure S 4.6. The endpoint pH of the 315 mL greywater treated by the REM under various power and time conditions.

Table S 4.1. The NSF/ANSI 350-2012 greywater recipe.

Ingredient	Amount/10 L
Body wash with moisturizer	1.59 g
Toothpaste	0.159 g
Deodorant	0.106 g
Shampoo	1.007 g
Conditioner	1.113 g
Lactic acid	0.159 g
Secondary effluent	200 mL
Bath cleaner	0.53 g
Liquid hand soap	1.219 g
test dust	1 g
Liquid laundry detergent	1.88 mL
Liquid laundry fabric softener	0.987 mL
Na_2SO_4	0.188 g
$NaHCO_3$	0.094 g
Na_3PO_4	0.188 g

Table S 4.2. The NSF/ANSI 350-2012 greywater quality.

Parameter	Range
Total suspended solids (TSS)	80-160 mg L^{-1}
BOD5	130-180 mg L^{-1}
Temperature	25-35 °C
pH	6.5-8.0
Turbidity	50-100 NTU
Total phosphorous	1.0-3.0 mg L^{-1}
Total Kjeldahl nitrogen	3.0-5.0 mg L^{-1}
COD	250-400 mg L^{-1}
TOC	50-100 mg L^{-1}
Total coliforms	10^3-10^4 mg L^{-1}
E. Coli	10^2-10^3 mg L^{-1}

References

(1) World Health Organization. *Sanitation*. https://www.who.int/news-room/fact-sheets/detail/sanitation.

(2) World Health Organization. *Drinking-water*. https://www.who.int/news-room/fact-sheets/detail/drinking-water.

(3) Massoud, M. A.; Tarhini, A.; Nasr, J. A. Decentralized Approaches to Wastewater Treatment and Management: Applicability in Developing Countries. *J. Environ. Manage.* **2009**, *90* (1), 652–659. https://doi.org/10.1016/j.jenvman.2008.07.001.

(4) Geetha Varma, V.; Jha, S.; Himesh Karthik Raju, L.; Lalith Kishore, R.; Ranjith, V. A Review on Decentralized Wastewater Treatment Systems in India. *Chemosphere* **2022**, *300*, 134462. https://doi.org/10.1016/j.chemosphere.2022.134462.

(5) Hube, S.; Wu, B. Mitigation of Emerging Pollutants and Pathogens in Decentralized Wastewater Treatment Processes: A Review. *Sci. Total Environ.* **2021**, *779*, 146545. https://doi.org/10.1016/j.scitotenv.2021.146545.

(6) Yang, Y.; Shin, J.; Jasper, J. T.; Hoffmann, M. R. Multilayer Heterojunction Anodes for Saline Wastewater Treatment: Design Strategies and Reactive Species Generation Mechanisms. *Environ. Sci. Technol.* **2016**, *50* (16), 8780–8787. https://doi.org/10.1021/acs.est.6b00688.

(7) Cho, K.; Hoffmann, M. R. Molecular Hydrogen Production from Wastewater Electrolysis Cell with Multi-Junction BiOx/TiO_2 Anode and Stainless Steel Cathode: Current and Energy Efficiency. *Appl. Catal. B.* **2017**, *202*, 671–682. https://doi.org/10.1016/j.apcatb.2016.09.067.

(8) Park, H.; Vecitis, C. D.; Hoffmann, M. R. Solar-Powered Electrochemical Oxidation of Organic Compounds Coupled with the Cathodic Production of Molecular Hydrogen. *J. Phys. Chem. A* **2008**, *112* (33), 7616–7626. https://doi.org/10.1021/jp802807e.

(9) Park, H.; Vecitis, C. D.; Choi, W.; Weres, O.; Hoffmann, M. R. Solar-Powered Production of Molecular Hydrogen from Water. *J. Phys. Chem. C* **2008**, *112* (4), 885–889. https://doi.org/10.1021/jp710723p.

(10) Jasper, J. T.; Shafaat, O. S.; Hoffmann, M. R. Electrochemical Transformation of Trace Organic Contaminants in Latrine Wastewater. *Environ. Sci. Technol.* **2016**, *50* (18), 10198–10208. https://doi.org/10.1021/acs.est.6b02912.

(11) Cho, K.; Qu, Y.; Kwon, D.; Zhang, H.; Cid, C. A.; Aryanfar, A.; Hoffmann, M. R. Effects of Anodic Potential and Chloride Ion on Overall Reactivity in Electrochemical Reactors Designed for Solar-Powered Wastewater Treatment. *Environ. Sci. Technol.* **2014**, *48* (4), 2377–2384. https://doi.org/10.1021/es404137u.

(12) Martínez-Huitle, C. A.; Ferro, S. Electrochemical Oxidation of Organic Pollutants for the Wastewater Treatment: Direct and Indirect Processes. *Chem. Soc. Rev.* **2006**, *35* (12), 1324–1340. https://doi.org/10.1039/B517632H.

(13) Fóti, G. Oxidation of Organics by Intermediates of Water Discharge on IrO_2 and Synthetic Diamond Anodes. *Electrochem. Solid-State Lett.* **1999**, *2* (5), 228. https://doi.org/10.1149/1.1390792.

(14) Tien, T. T.; Luu, T. L. Electrooxidation of Tannery Wastewater with Continuous Flow System: Role of Electrode Materials. *Environ. Eng. Res.* **2019**, *25* (3), 324–334. https://doi.org/10.4491/eer.2018.349.

(15) Zhang, Y.; Yang, Y.; Yang, S.; Quispe-Cardenas, E.; Hoffmann, M. R. Application of Heterojunction Ni–Sb–SnO_2 Anodes for Electrochemical Water Treatment. *ACS EST Eng.* **2021**, *1* (8), 1236–1245. https://doi.org/10.1021/acsestengg.1c00122.

(16) Guo, L.; Jing, Y.; Chaplin, B. P. Development and Characterization of Ultrafiltration TiO_2 Magnéli Phase Reactive Electrochemical Membranes. *Environ. Sci. Technol.* **2016**, *50* (3), 1428–1436. https://doi.org/10.1021/acs.est.5b04366.

(17) Le, T. X. H.; Haflich, H.; Shah, A. D.; Chaplin, B. P. Energy-Efficient Electrochemical Oxidation of Perfluoroalkyl Substances Using a Ti_4O_7 Reactive Electrochemical Membrane Anode. *Environ. Sci. Technol. Lett.* **2019**, *6* (8), 504–510. https://doi.org/10.1021/acs.estlett.9b00397.

(18) Shi, H.; Wang, Y.; Li, C.; Pierce, R.; Gao, S.; Huang, Q. Degradation of Perfluorooctanesulfonate by Reactive Electrochemical Membrane Composed of Magnéli Phase Titanium Suboxide. *Environ. Sci. Technol.* **2019**, *53* (24), 14528–14537. https://doi.org/10.1021/acs.est.9b04148.

(19) Li, D.; Tang, J.; Zhou, X.; Li, J.; Sun, X.; Shen, J.; Wang, L.; Han, W. Electrochemical Degradation of Pyridine by Ti/SnO_2–Sb Tubular Porous Electrode. *Chemosphere* **2016**, *149*, 49–56. https://doi.org/10.1016/j.chemosphere.2016.01.078.

(20) Zhou, C.; Wang, Y.; Chen, J.; Niu, J. Porous Ti/SnO2-Sb Anode as Reactive Electrochemical Membrane for Removing Trace Antiretroviral Drug Stavudine from Wastewater. *Environ. Int.* **2019**, *133*, 105157. https://doi.org/10.1016/j.envint.2019.105157.

(21) Li, F.; Wichmann, K.; Otterpohl, R. Review of the Technological Approaches for Grey Water Treatment and Reuses. *Sci. Total Environ.* **2009**, *407* (11), 3439–3449. https://doi.org/10.1016/j.scitotenv.2009.02.004.

(22) McCrory, C. C. L.; Jung, S.; Peters, J. C.; Jaramillo, T. F. Benchmarking Heterogeneous Electrocatalysts for the Oxygen Evolution Reaction. *J. Am. Chem. Soc.* **2013**, *135* (45), 16977–16987. https://doi.org/10.1021/ja407115p.

(23) Malinović, B. N.; Markelj, J.; Žgajnar Gotvajn, A.; Kralj Cigić, I.; Prosen, H. Electrochemical Treatment of Wastewater to Remove Contaminants from the Production and Disposal of Plastics: A Review. *Environ. Chem. Lett.* **2022**, *20* (6), 3765–3787. https://doi.org/10.1007/s10311-022-01497-8.

(24) Yang, Y.; Hoffmann, M. R. Synthesis and Stabilization of Blue-Black TiO_2 Nanotube Arrays for Electrochemical Oxidant Generation and Wastewater Treatment. *Environ. Sci. Technol.* **2016**, *50* (21), 11888–11894. https://doi.org/10.1021/acs.est.6b03540.

Chapter 5 Diffusion-boosting monolithic electro-Fenton cathodes derived from 3D-printing

Heng Dong#, Menglin Yu#, Léopold Dobelle* and Michael R. Hoffmann*

Linde Laboratories, California Institute of Technology, Pasadena, California 91125, USA

*Corresponding authors:

Léopold Dobelle - ldobelle@caltech.edu
Michael R. Hoffmann - mrh@caltech.edu

5.1 Abstract

The Fenton reaction is one of the most important advanced oxidation processes (AOPs) that is widely used in water treatment to remove non-biodegradable pollutant. Heterogeneous electro-Fenton (HEF) process, catalyzed by carbon-based cathodes, has received considerable attention as an evolving branch due to its wide working pH range and independence from chemical dosing. However, the conventional carbon cathodes suffered from poorly controlled porosities, which hamper mass transport and limit the overall catalytic performance. Here, a series of carbon lattice cathodes derived from 3D-printed resin lattices were successfully used to catalyze electro-Fenton reaction. Grid-2% cathode showed 157% higher specific activity for electrochemical H_2O_2 production and 256% higher specific activity for trimethoprim degradation than Star-2%, and the different performance was attributed to the rationally designed macroscopic porosities. Grid-2% achieved 97% aqueous trimethoprim removal in 60 min. This work demonstrated that 3D printing serves as a feasible method to allow for fabrication of carbon cathodes with controllable macroscopic porosities, greatly enhancing the electro-Fenton catalytic performance.

5.2 Introduction

The Fenton reaction, featuring generation of hydroxyl radicals (·OH) from Fe(II)/Fe(III) redox couple and H_2O_2, is one of the most important advanced oxidation processes (AOPs)[1].

Due to its high efficiency, engineering simplicity and low price, Fenton reaction has been widely used in treatment of a series of nonbiodegradable pollutants. However, conventional homogeneous Fenton process relies on dosing the wastewater with external Fe(II) and H_2O_2[2]. H_2O_2 is currently produced industrially by oxidation of anthraquinone, which leads to not only extensive energy consumption but also further waste production. Furthermore, the transportation of H_2O_2 also poses potential hazard[3]. On the other hand, the solubility of the Fe^{2+} and Fe^{3+} requires acidic pH (< 4). Therefore, circum-neutral wastewater needs acidification before conventional Fenton treatment, and sequential addition of bases to adjust the pH back to neutral, which adds to the total treatment cost and generated Fe sludge in the effluent[4].

Considering these drawbacks, alternative sources of both H_2O_2 and Fe catalysts have been sought for Fenton reaction. Electrochemical 2-electron oxygen reduction reaction (ORR) has been widely adopted for in situ generation of H_2O_2[5–12]. Carbon-based materials are often used to catalyze the reaction because of the earth abundance, unique surface properties and tunable porosity[13,14]. On the other hand, for catalytic H_2O_2 activation, heterogeneous Fenton reactions (HEFs) have been developed where solid Fe catalysts replace soluble Fe^{2+} and Fe^{3+} species to catalyze H_2O_2 cleavage to produce ·OH. Compared to conventional homogeneous Fenton systems, heterogeneous electro-Fenton systems have a substantially wider working pH range[1]. Furthermore, with the Fe catalysts embedded in carbon cathodes, the two techniques can be combined into electrochemical heterogeneous Fenton process, which is able to perform water treatment with no requirement for external addition of chemicals[15,16]. An HEF carbon nanotube filter functionalized with FeOCl was used for flow-through removal of tetracycline in the pH range of 3.4 – 10.1, and an oxidation flux was obtained with an applied potential of −0.8 V vs. Ag/AgCl and a flow rate of 1.5 mL min^{-1} [17]. Multi-phase porous HEF catalysts derived from Fe-containing metal-organic frameworks also achieved efficient degradation of multiple herbicides, and 90% mineralization of napropamide was obtained in 2 h in circum-neutral condition under -0.14 V vs. RHE[15].

For electrochemical heterogeneous Fenton process, the water treatment performance is closely associated with the aqueous H_2O_2 concentration, which is dictated by the catalytic activity of the carbon cathodes. Despite their rich porosity and relatively large surface areas, the activity of the carbon catalysts is often limited by the sluggish inner mass transport[18,19]. Specifically, carbon catalysts can be generally categorized into powders and monoliths. For powdery carbon catalysts such as activated carbon (AC) or carbon black (CB), use of polymeric binders such as Nafion and PTFE is required for electrode fabrication[3,20]. Use of binders not only blocked the porosity of carbon materials, but also reduce the conductivity and compromise the electrocatalytic activity, hence leading to “waste” of inner surface area and compromised overall catalytic activity.

Monolithic carbon cathodes also generally suffer from poorly controlled porosities that hamper inner mass transport. Various monolithic carbon-based HEF catalysts have been developed as binder-free alternatives. Carbon felt has been conventionally used for 2-electron ORR catalysis[21], and it has also been incorporated with Co and Fe hydroxides to function as HEF catalysts[22]. Carbon fibers fabricated by pyrolyzing electrospun fibers were also demonstrated to be freestanding HEF cathodes[16]. In addition, carbon aerogels have been employed by numerous studies as monolithic cathodes for electro-Fenton removal of a wide spectrum of aqueous contaminants including chlorophenol, haloacetamides[23], and a fungicide Metalaxyl[24]. Different metal species, such as Fe, Fe_2O_3 and Pd-Fe nanoalloy, were incorporated into the carbon aerogels to catalyze H_2O_2 activation. Following a similar procedure to typical carbon aerogel synthesis, we have also developed porous carbon monoliths as a “one-stop” catalyst for both 2-electron ORR and H_2O_2 activation to directly produce ·OH[13]. However, despite the binder-free nature of the monolithic cathodes, these materials usually feature mesoporous or even microporous structure that leads to sluggish inner diffusion[13]. This is likely to also cause “waste” of inner surface area and catalytic sites because the overall catalytic activity is anticipated to be mainly contributed by the catalysts near the outer surface. This limitation is expected to get worse for scaled-up cathodes in practical applications.

Given the importance of mass transfer for electrochemical reactions, it is imperative to develop carbon cathodes with controlled porosities to facilitate the inner mass transport. 3D printing has been used increasingly in fabrication of electrodes with highly controlled porosity and enhanced diffusion that were used in lithium-oxygen batteries and flow-through electrochemical cell. Here, by using 3D-printed polymer resin lattice as the precursor, we demonstrate that it is feasible to improve the inner mass transport and enhance the specific activity by rationally designing the macroscopic structure of the carbon-based cathodes.

5.3 Experimental

5.3.1 Materials

All chemicals were obtained from Sigma Aldrich and used without further purification. Solvents were HPLC grade unless otherwise stated.

5.3.2 Preparation of carbon lattice electrodes

The carbon lattice cathodes were prepared by pyrolyzing the 3D-printed resin lattices, as shown in Figure S5.1. First, to fabricate the precursor resin lattices, MIL-53(Fe), prepared using a reported procedure[25], was mixed with Nova3D grey 405nm LCD rapid resin at predetermined mass ratios. The mixture was stirred for 12 h to form a uniform suspension. The resin lattices were then printed from the suspension using a Nova3D Bene 3 Printer. The as-printed resin lattices were ultrasonically washed with methanol and dried at 70 °C. The carbon lattice cathodes were produced by pyrolyzing the resin lattices at 800 °C for 2 h in N_2, with a ramping rate of 3 °C/min.

To demonstrate the influence of macroscopic porous structure on the catalytic performance, three lattice structures (Grid, Diamond, and Star) with different macroscopic porosities were selected. Details of the three lattice structures synthesized in this work are shown in Table 5.1 and Figure S5.2, where the porosities were calculated by SolidWorks 2019 software. The Grid structure had the largest macroscopic porosity, followed by Diamond and Star structures.

The fabricated cathodes were named based on the structure and percentage of MIL-53(Fe) in the precursor resin lattice (e.g. Grid-2% refers to grid-structure carbon lattices printed from resin mixture containing 2% of MIL-53(Fe)).

Table 5.1. Macroscopic structural information about the three lattice structures.

Structure name	Length : Width : Height	Macroscopic porosity
Grid	13 : 8 : 3	0.78
Diamond	13 : 8 : 3	0.63
Star	13 : 8 : 3	0.47

5.3.3 Characterization of the electrodes

Surface morphology and elemental composition of the CMOFs-NH_2@PCMs were examined using a ZEISS 1550VP field emission scanning electron microscope (FE-SEM) equipped with an Oxford X-Max SDD energy dispersive X-ray spectrometer (EDS). X-ray powder diffraction (XRD) patterns were collected using a Bruker D8 A25 Advance diffractometer with Cu-Kα radiation (λ=1.5418 Å). To characterize the microscopic porosity of the C-Fe lattice materials, the carbon lattices were ground to powder and nitrogen adsorption-desorption isotherms were measured by a gas adsorption instrument (Micromeritics 3Flex) to determine the Brunauer-Emmett-Teller (BET) surface area and pore size distribution.

5.3.4 Electrochemical experiments

Electrochemical experiments were performed in conventional three-electrode cells using a Bio-Logic VSP potentiostat at room temperature. 10 mL 0.1 M Na_2SO_4 solution was used as the supporting electrolyte for all electrochemical tests. A Pt wire was used as the counter electrode and saturated calomel electrode (SCE) was used as the reference electrode. Recorded potentials were converted to reversible hydrogen electrode (RHE) scale with the formula RHE = SCE + 0.059 × pH + 0.241 V).

The 2-electron catalytic activity of the carbon lattice cathodes were characterized by cyclic voltammetry (CV) and measuring the concentration of electrochemically generated H_2O_2 and ·OH. CV was conducted in N_2- and O_2-saturated electrolyte at a scan rate of 10 mV s^{-1}, and electrocatalytic production of H_2O_2 and ·OH was performed under constant potential conditions.

The electro-Fenton water treatment performance of the carbon lattice cathodes was demonstrated by using trimethoprim (information shown in Table S5.1) as a model pollutant. Electrochemical treatment of trimethoprim was also tested under constant potential conditions. For all the trimethoprim degradation experiments, the initial concentration of pesticides was 5 mg L^{-1}. H_2O_2 production and trimethoprim degradation tests were conducted under various pH conditions by adjusting the initial solution pH to 4-10 with 1 M H_2SO_4 and 1 M NaOH solutions, while no buffer was added in the reaction process.

Stability of the electrodes was characterized by their multi-batch pesticide degradation performance. Specifically, the electrode was subjected to five consecutive trimethoprim degradation batches. The trimethoprim concentration was also 5 mg L^{-1}. Between each two batches, the electrode was rinsed with water and dried at 60 °C.

5.3.5 Analytical methods

To quantify the production of reactive species and degradation of the pesticides, the electrolyte was sampled at certain time intervals. The H_2O_2 concentration was analyzed by titanium oxalate spectrophotometric method, as detailed in previous papers. The absorbance of the ($TiO(H_2O_2)^{2+}$) complex was measured using a JASCO V-750 spectrophotometer at 400 nm. H_2O_2 solutions with known concentration were used to construct a calibration curve. Hydroxyl radical was quantified using terephthalic acid, which forms the 2-hydroxyterephthalic acid adduct in the presence of ·OH. The concentration of TAOH was quantified using a fluorescence spectroscopy (Hitachi F7000) with an excitation wavelength of 350 nm and a monitored emission wavelength of 430 nm.

The concentrations of trimethoprim were analyzed using a high-performance liquid chromatography (Waters Acquity UPLC) system coupled with an e2998 photodiode array detector and an e2695 separation module. 0.1% phosphoric acid and methanol were used as mobile phase at a flow rate of 0.8 mL min^{-1}, and Sunfire C18 column (4.6 × 50 mm; 5 µm particles) was used. The total organic carbon (TOC) was determined using an Analytik Jena MultiN/C3100 TOC analyzer.

5.4 Results & discussions

5.4.1 Electrode characterization

The porous structures of the carbon lattice electrode, both on the macroscopic and on the microscopic scale, are shown in Figure 5.1. After pyrolysis, each carbon lattice cathode was composed of 13 × 8 × 3 = 312 structural units, and a structural unit, regardless of the structure, had a size of ~1 mm × 1 mm × 1 mm. (Figure 5.1a) Besides the macroscopic scaffold structure, the carbon struts also possessed mesoporous structures, which were examined by N_2 adsorption-desorption isotherms (Figure 5.1b), with the corresponding pore distribution shown in Figure 5.1c. Grid carbon lattice cathodes had abundant mesopores concentrated at ~4.9 nm, while Diamond and Star cathodes showed smaller mesoporosity concentrated at ~3.5 nm and ~2.9 nm, respectively. The BET specific surface area was 564.38 m^2 g^{-1} for Grid carbon lattice, 483.84 m^2 g^{-1} for Diamond and 420.86 m^2 g^{-1} for Star (Table S5.2). As the BET surface areas were measured after griding the carbon lattices to powder, the specific surface areas in the monolithic form were expected to be smaller. The microscopic porosities were comparable to our previously reported carbon cathodes. However, given the macroscopic lattice structure, the inner mass transport was expected to be much better than the conventional carbon monoliths.

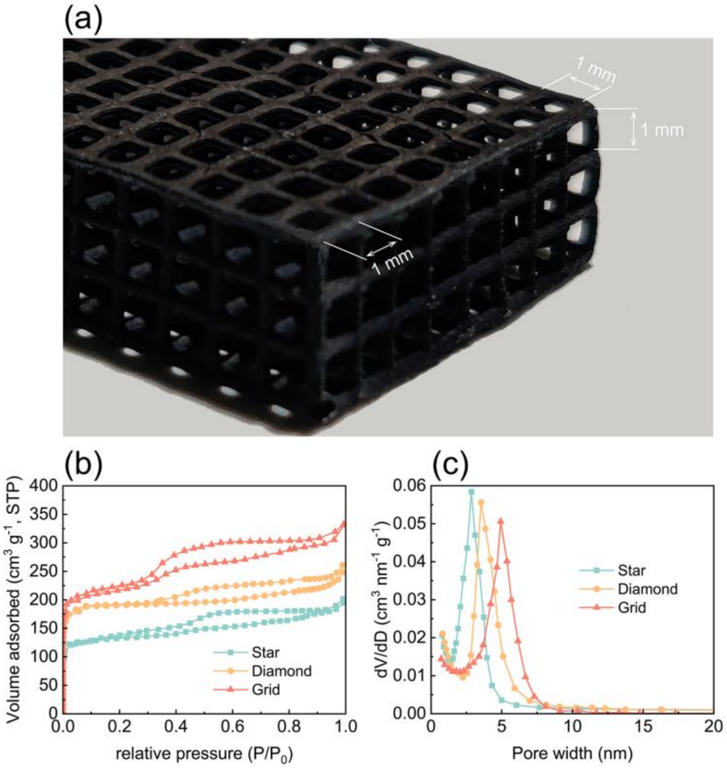

Figure 5.1. Illustration of the porous structures of the carbon lattices. (a) Illustration of lattice structure of Grid carbon cathode; (b) N_2 adsorption-desorption isotherms and (c) pore distribution of carbon lattice cathodes of three structures.

The embedded Fe was uniformly distributed in the carbon lattice cathodes, as shown in Figure S5.3. This was consistent with our previous work on electro-Fenton cathode, indicating that using Fe-bearing MOFs as the precursor led to good dispersion of Fe in the formed carbon monoliths. Meanwhile, EDS mapping also reveals the elemental composition of the carbon lattice cathodes with respect to the contents of MIL-53(Fe) in the precursor resins (Table S5.3). The Fe content was generally proportional to the MIL-53(Fe) content in the precursor resin, and no significant change was observed between Grid and Star structure cathodes. When the MIL-53(Fe) content was above a certain threshold, the resin mixture became "unprintable". The "printability" threshold varied with cathode structures. For Star lattices, resin lattices with as high as 8% MIL-53(Fe) were successfully printed, while for Grid lattices, resin mixtures with MIL-53(Fe) content beyond 3% were not successfully printed.

The specific form of the embedded Fe varied with the Fe percentages in the carbon lattices according to XRD spectra (Figure 5.2), and the features observed for Grid and for Star cathodes were similar. Specifically, for both Grid and Star carbon lattices, when the percentage of MIL-53(Fe) was no larger than 2% (which corresponded to a final Fe concentration of ~9% in the carbon lattices), all the embedded Fe was in the form of Fe_3O_4. As the Fe content went higher, the excessive Fe was in the form of metallic Fe. This was consistent with the reducing environment used in pyrolysis. The "humps" in the XRD spectra between 20° and 30° was ascribed to the carbon substrate.

The surface chemical states of Grid-2% and Star-2% cathodes were also in good agreement (Figure S5.4). The C1s peaks of both Grid-2% and Star-2% were at 285.5 eV (Figure S5.4a and S5.4d), in good agreement with the C-C peak position. Clear shoulders were observed for the C1s peaks, which were ascribed to the C-O and C=O bonds[26]. The O1s peaks for both cathodes were observed at 532.5 eV (Figure S5.4b and S4e), which was between the standard positions of C-O and C=O[26]. It is worth noting that the contribution of incorporated Fe to the position of the O1s peak was expected to be small since the O1s peak was observed at 529.9 eV for Fe_3O_4 (Figure S5.4g). On the other hand, two Fe 2p peaks were observed for both cathodes at 711.5 eV and 724.8 eV, respectively (Figure S5.4c and S5.4f), slightly higher than those for pure Fe_3O_4 (710.8 eV and 724.0 eV, Figure S5.4h). This indicated that the surface Fe species might get further oxidized.

The surface concentration of O (14.2%) and Fe (0.4%), as acquired by XPS, was substantially lower than the bulk concentrations examined using EDS. This implied that the majority of Fe in the carbon lattice cathodes was shielded by carbon and not directly exposed to the electrolyte, which is anticipated to minimize the Fe leaching and enhance the stability of the cathodes[15]. However, this also reduced the number of effective catalytic sites for H_2O_2 activation. The incorporation of Fe in the carbon lattice cathodes may require further study to reach an optimal balance of catalytic activity and stability.

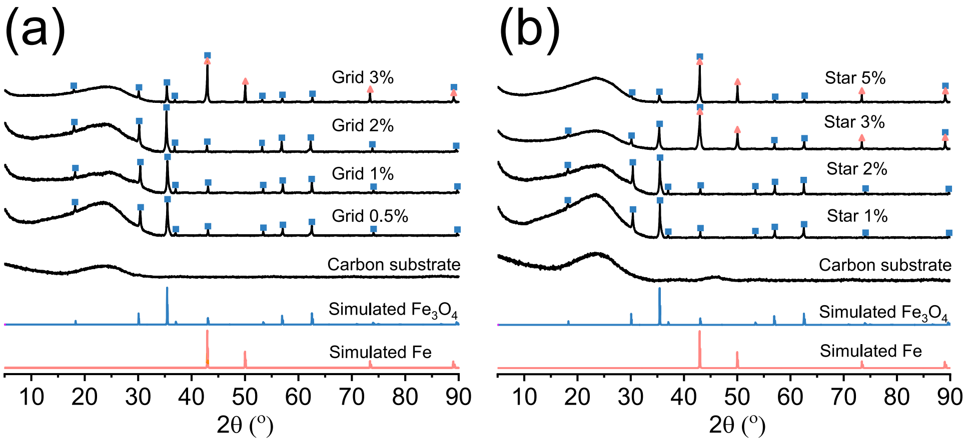

Figure 5.2. XRD spectra of (a) Grid and (b) Star carbon lattice cathodes. The percentages denote the content of MIL-53(Fe) added to the precursor resin lattices.

5.4.2 Electrochemical H_2O_2 and ·OH production

The carbon lattice skeleton successfully catalyzed 2-electron ORR to produce H_2O_2, as shown by CV and H_2O_2 concentration measurement (Figure S5.5 & Figure 5.3). Specifically, pure Grid carbon lattice cathode was subjected to CV in 0.1 M Na_2SO_4 solutions under various pH conditions, and the data was shown in the Figure S5.5. A reduction peak was observed when the electrode was tested in oxygen-saturated solutions, while the peak was absent in nitrogen-saturated solutions, showing the ORR catalytic activity of the carbon lattice cathode. The catalytic activity was further demonstrated by measuring the electrochemically produced H_2O_2 under constant potential condition (Figure 5.3). Under an applied potential of -0.146 V vs. RHE in circum-neutral 0.1 M Na_2SO_4 solution, the Grid pure carbon cathode had a H_2O_2 production rate of 3.08 mmol g^{-1} h^{-1}, 50% higher than Diamond (2.05 mmol g^{-1} h^{-1}) and 157% higher than Star (1.20 mmol g^{-1} h^{-1}) cathodes. The higher specific electrocatalytic activity indicated that the Grid structure may lead to higher utilization efficiency of the catalyst.

The specific catalytic activity normalized to the mass of the catalysts was a gauge of the combined effects of the intrinsic catalytic activity of the carbon materials and the mass transport. Given the similar elemental ratios and chemical nature as revealed by EDS, XRD and XPS, the intrinsic catalytic activities of the carbon materials for the three types of cathodes were anticipated to be similar. On the other hand, the mass transport was contributed by both the macroscopic and microscopic porosities.

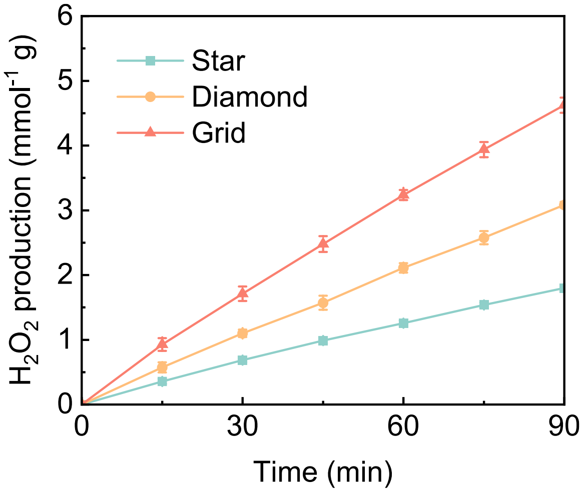

Figure 5.3. Electrochemical H_2O_2 production by carbon lattice cathodes of different structures, measured under -0.146 V vs. RHE in circum-neutral 0.1 M Na_2SO_4 solution.

The H_2O_2 production Grid cathode was high over the pH range of 4-10 (Figure S5.6). The highest H_2O_2 production rates at pH 4, 7 and 10 were 0.59 mmol g^{-1} h^{-1}, 0.60 mmol g^{-1} h^{-1} and 0.58 mmol g^{-1} h^{-1} respectively, showing that the Grid carbon lattice catalyzed efficient 2-electron ORR in a wide pH range. On the other hand, lowering the applied potential significantly increased the H_2O_2 production.

Based on the electrochemically produced H_2O_2, the incorporated Fe in the carbon lattices successfully catalyzed *in situ* Fenton reaction to generate ·OH (Figure 5.4). Grid-2%, Diamond-2% and Star-2% produced ·OH at an almost constant rate within an hour. Consistent with the trend of H_2O_2 production, Grid-2% had the highest ·OH production, followed by Diamond-2% and Star-2% (Figure 5.4a). Consistent with the H_2O_2 production, the higher specific ·OH production rate for Grid-2% was also attributed to its better mass transport conditions.

The influence of Fe loading on the ·OH production for Grid cathodes was shown in Figure 5.4b. Constant ·OH production rates were observed for Grid-0%, Grid-0.1%, Grid-0.5%, Grid-1% and Grid-2%, and the ·OH production increased with the Fe content. Considering that electro-Fenton reaction is a two-step process involving H_2O_2 production and activation, this indicated that the H_2O_2 activation was the rate-limiting step here. However, for Grid-3%, the initial ·OH production rate was higher than that of Grid-2%, but then decreased significantly and the cumulative ·OH levelled off within an hour. This indicated that the Grid-3%, although starting with hither catalytic activity than Grid-2%, was less stable. It is also worth noting that ·OH was also detected for pure carbon lattice cathode, which agreed with our previous study on the activation of H_2O_2 by carbon materials.

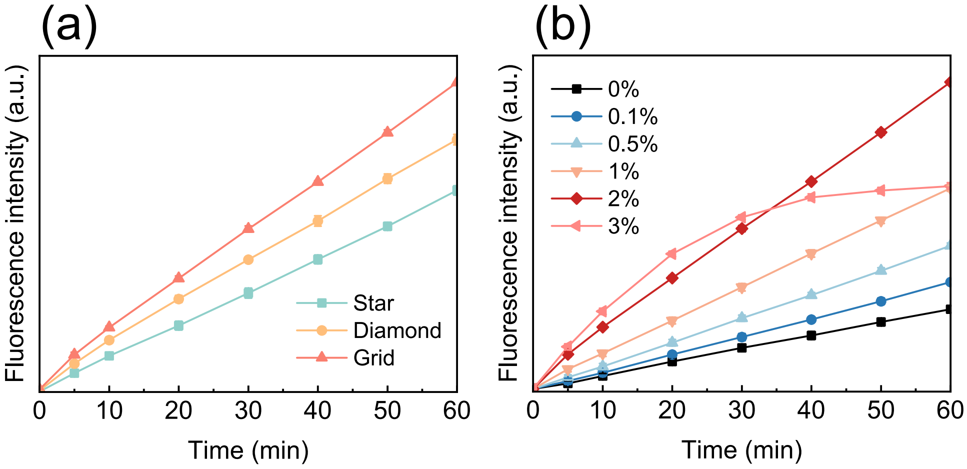

Figure 5.4. Electro-Fenton generation of ·OH by the carbon lattices. (a) Electrochemical generation of ·OH by Grid-2%, Diamond-2% and Star-2% carbon lattice cathodes in 0.1 M circum-neutral Na_2SO_4 solution under -0.146 V vs RHE, as quantified by using terephthalic acid as a probe; (b) production of ·OH by Grid carbon lattices with different Fe contents.

5.4.3 Electrochemical trimethoprim degradation

Grid-2% showed the best specific activity for trimethoprim degradation, compared to Diamond-2% and Star-2% (Figure 5.5a). Under an applied potential of -0.146 V in circum-neutral 0.1 M Na_2SO_4 solution, Grid-2% cathode achieved a trimethoprim degradation of 0.57 mg g^{-1} in 60 min, 73% higher than Diamond-2% (0.33 mg g^{-1}) and 256% higher than Star-2% (0.16 mg g^{-1}). The result was consistent with the H_2O_2 and ·OH production results. By normalizing the degradation to the mass of the catalysts, the measured performance was again a combination of both the intrinsic activity of the carbon materials and the mass transport, where the mass transport was contributed by both the macroscopic and the microscopic porosities.

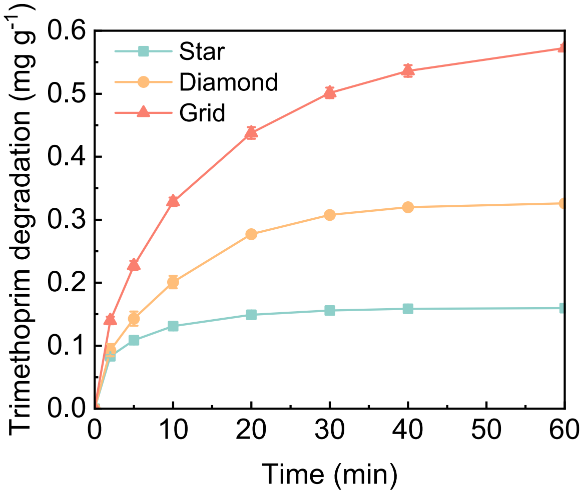

Figure 5.5. Degradation of 5 mg L^{-1} trimethoprim by carbon lattice cathodes of three structures.

The electro-Fenton degradation of trimethoprim by Grid cathodes was further studied (Figure S5.7a). First, the degradation of trimethoprim by Grid-2% was tested under various to verify the degradation mechanism. Little trimethoprim degradation was caused by 400 mg L^{-1} H_2O_2, showing that H_2O_2 alone could not degrade trimethoprim. Grid-2% cathode achieved 97% trimethoprim degradation in 60 min in O_2-saturated solution, as opposed to only 26% degradation in N_2-saturated circum-neutral 0.1 M Na_2SO_4 solution, which was ascribed to electrosorption. Notably, similar degradation performance (28%) to that in N_2-saturated solution in 60 min were obtained when testing in O_2-saturated solution with 45 mM isopropanol as a ·OH scavenger. The results confirmed that the trimethoprim degradation was mainly caused by the ·OH generated by the electro-Fenton reaction catalyzed by Grid-2% cathode. In addition to obtaining efficient trimethoprim degradation, Grid-2% also achieved 99% mineralization in 120 min (Figure S5.8).

The influence of Fe loading on the trimethoprim degradation performance is shown in Figure S5.7b. Grid-2% had the best trimethoprim degradation performance, consistent with its highest ·OH production rate. Due to the decrease in ·OH production over time (Figure 5.4b), the trimethoprim degradation performance of Grid-3% was inferior to Grid-2%.

The trimethoprim degradation by Grid-2% maintained over 0.57 mg g^{-1} in the range of 4-10 (Figure S5.7c), agreeing with the H_2O_2 production results. This showed that Grid-2% cathode was capable of not only producing H_2O_2, but also effectively activating it in the pH range of 4-10 to generate ·OH. This also indicated that the carbon lattice cathodes might be applied to a variety of water bodies for electrochemical pharmaceutical removal. On the other hand, more negative applied potential led to significantly better degradation performance (Figure S5.7d).

Degradation of trimethoprim by carbon lattice cathode under various pH and applied potential conditions was well described by pseudo first-order kinetic models (Table S5.4).

5.4.4 Stability

The stability of Grid-2% cathode was examined by multi-batch trimethoprim degradation tests. In 6 consecutive batches, Grid-2% cathode maintained over 99% trimethoprim degradation in 60 min, and the pseudo first-order rate constant ranged 0.06 ± 0.007 min^{-1}. This demonstrated the good stability of Grid-2% cathode.

More generally, all the carbon lattice cathodes were subjected to the same stability tests, and the change in elemental composition was monitored (Table S5.3). Little change in the composition was observed for cathodes with MIL-53(Fe) percentages no larger than 2%, showing the excellent stability. However, for the cathodes with higher Fe content, a drastic decrease in the Fe percentages was observed after the test. This accounted for the inferior ·OH production and trimethoprim degradation performance of Grid-3%. The different stabilities of the electrodes were ascribed to the different forms of embedded Fe in the carbon lattice cathodes, as shown by the XRD spectra (Figure 5.1).

5.5 Conclusion

A series of carbon lattice cathodes were synthesized to catalyze electro-Fenton reaction, demonstrating that 3D printing serves as a feasible method to allow for fabrication of carbon cathodes with controllable macroscopic porosities that greatly enhanced the electro-Fenton catalytic performance. The Grid-2% cathode achieved effective electrochemical generation of H_2O_2 and ·OH. It could also degrade and mineralize trimethoprim in a wide pH range. Furthermore, with the optimal Fe content, the carbon lattice cathodes showed excellent stability. These features make the carbon lattice cathodes promising candidates for aqueous pharmaceutical removal and water remediation.

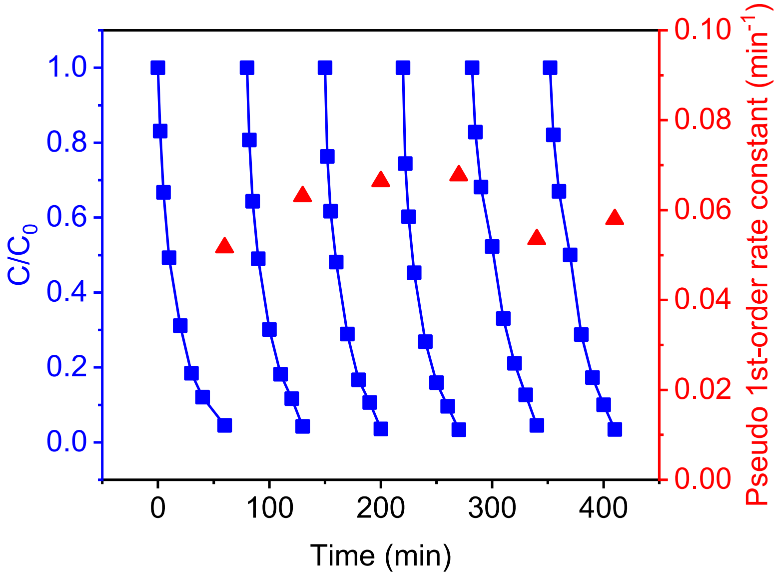

Figure 5.6. 6 Consecutive trimethoprim degradation batches to test the stability of Grid-2% cathode.

5.6 Supplementary materials

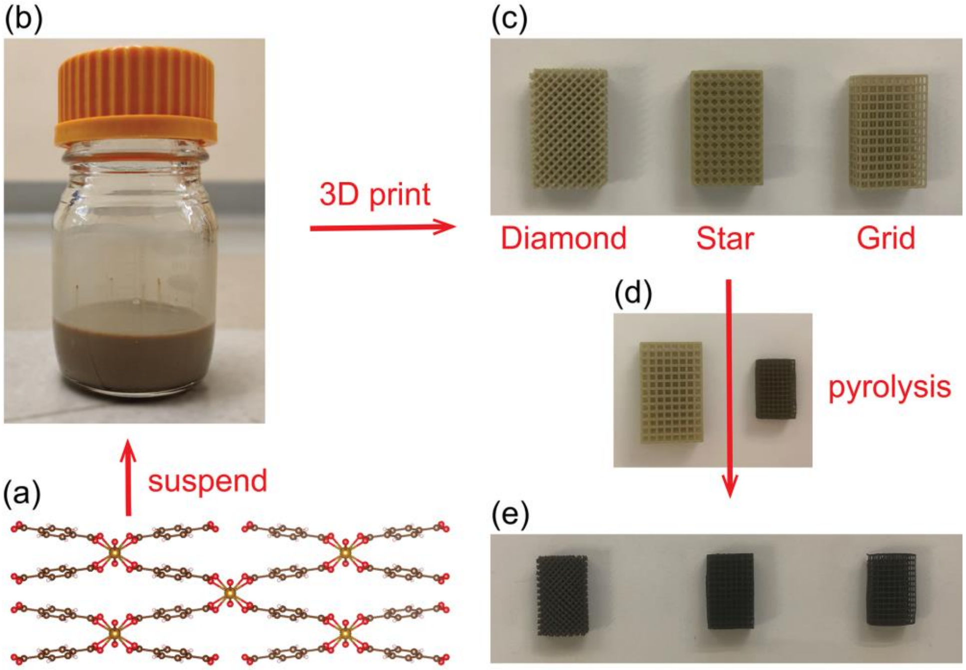

Figure S 5.1. Fabrication process of carbon lattice cathodes.

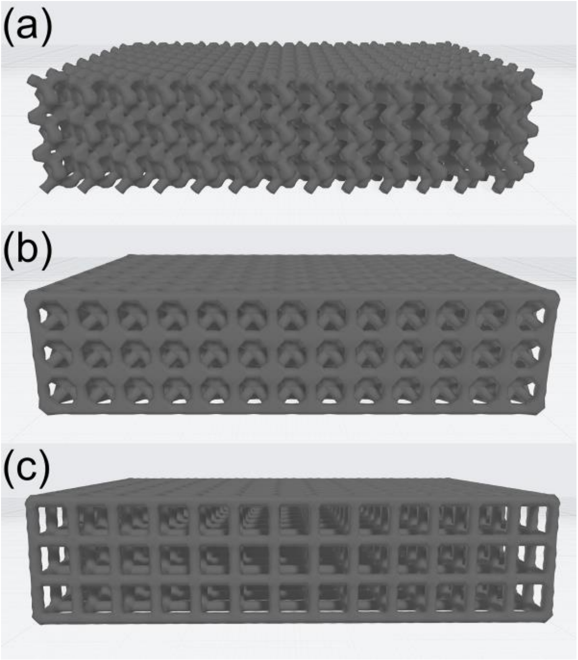

Figure S 5.2. Fabrication process of carbon lattice cathodes.

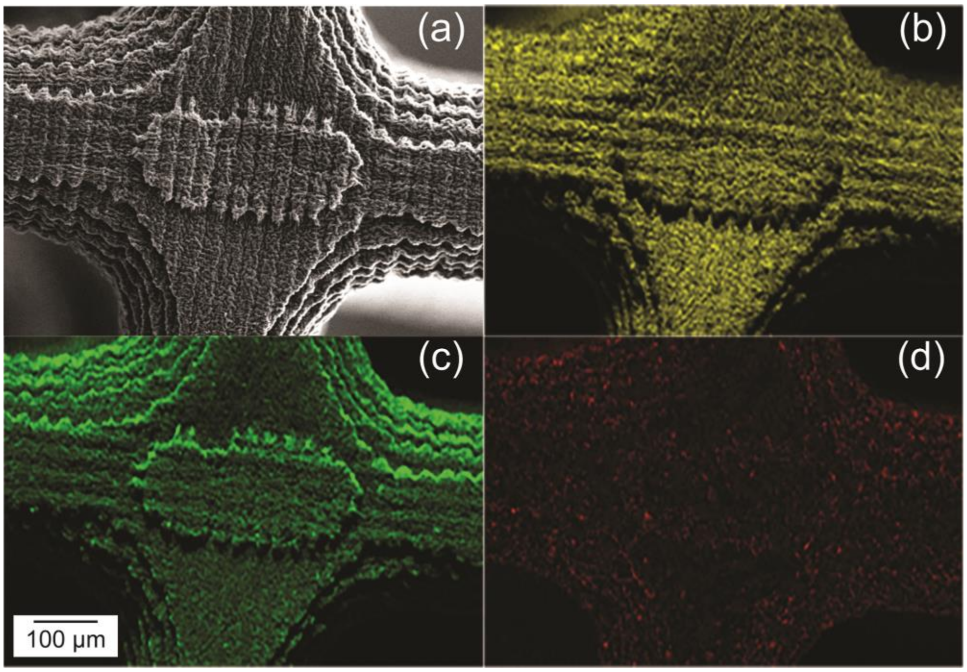

Figure S 5.3. EDS mapping of Grid carbon lattice cathode.

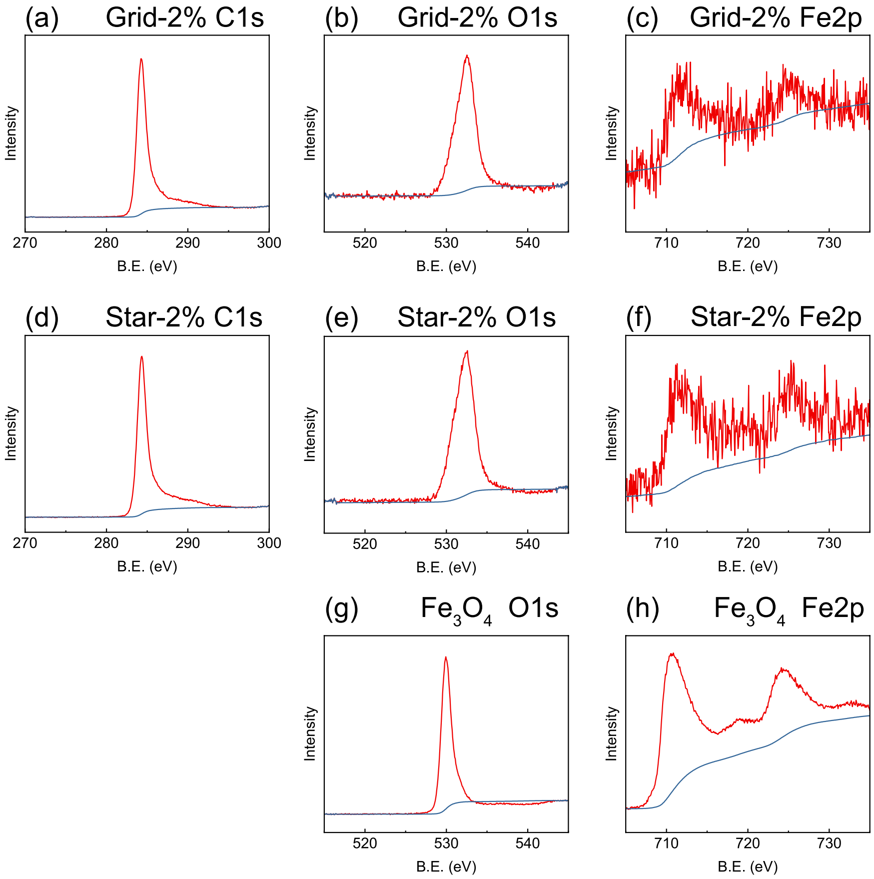

Figure S 5.4. XPS spectra of (a)-(c) Grid-2% and (d)-(f) Star-2% carbon lattice cathodes. The Fe 2p spectrum of pure Fe_3O_4 was measured for reference. The blue curves denote the Shirley background.

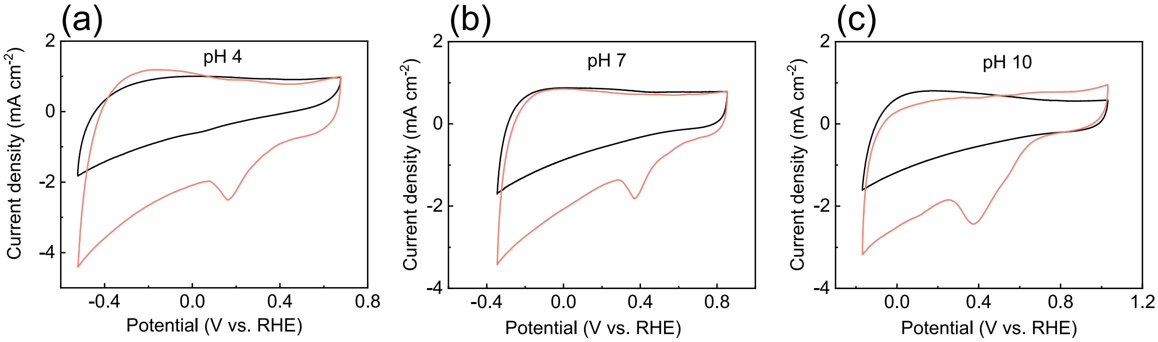

Figure S 5.5. Cyclic voltammograms of pure Grid carbon lattice cathode.

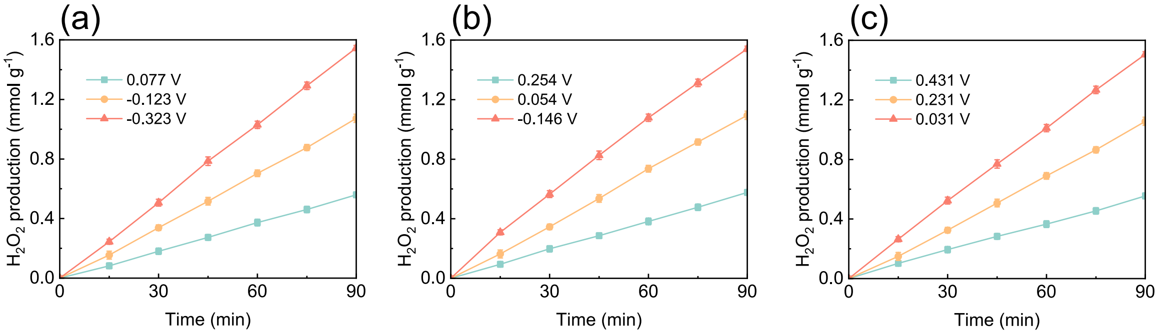

Figure S 5.6. Electrochemical production of H_2O_2 by Grid pure carbon lattice cathode under various applied potentials at (a) pH 4, (b) pH 7 and (c) pH 10.

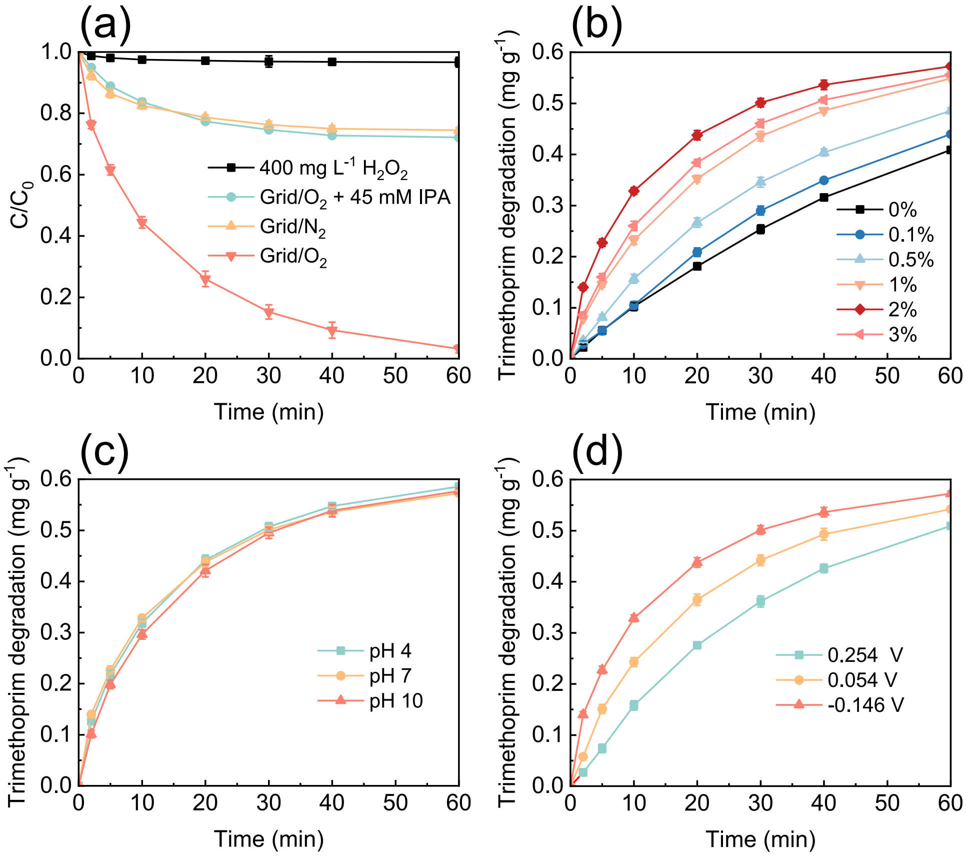

Figure S 5.7. Influence of various factors on the degradation of trimethoprim by Grid-2%. (a) Degradation of trimethoprim by Grid-2% under various conditions; (b) degradation of trimethoprim by Grid cathodes with different Fe loading; (c) Degradation of trimethoprim by Grid-2% at various pH levels; (d) Degradation of trimethoprim by Grid-2% under different applied potentials.

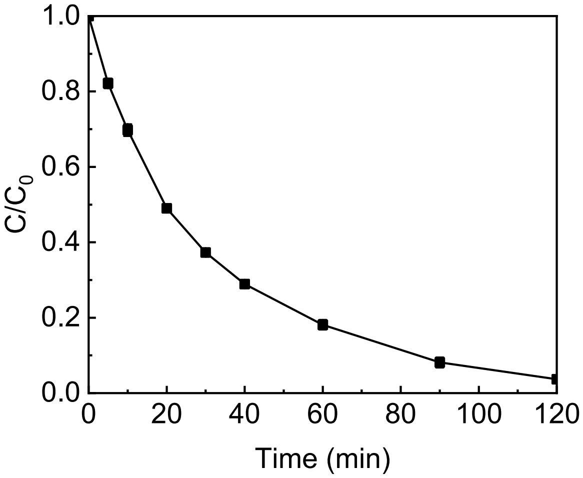

Figure S 5.8. TOC removal by Grid-2% cathode under -0.146 V vs RHE in 0.1 M Na_2SO_4 solution with 5 mg L^{-1} trimethoprim.

Table S 5.1. Chemical used in this study.

Chemical name	**IUPAC name**	**Formula**	**Structure**	**CAS**
Trimethoprim	5-[(3,4,5-trimethoxyphenyl)methyl]-2,4-pyrimidinediamine	$C_{14}H_{18}N_4O_3$	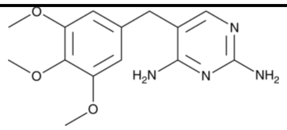	738-70-5

Table S 5.2. BET surface area of different construction 3D printed carbon electrodes.

Sample name	BET surface area (m^2 g^{-1})
Star	420.46
Diamond	483.84
Grid	564.38

Table S 5.3. Elemental composition of different doping of MIL-53(Fe) in cross construction 3D printed carbon electrode before and after cycle.

Materials	**Elemental Composition (at%)**					
	Before stability test			**After stability test**		
	C	**O**	**Fe**	**C**	**O**	**Fe**
Grid 0.1%	88.9	10.6	0.5	89.1	10.4	0.5
Grid 0.5%	84.6	13.2	2.2	84.3	13.4	2.3
Grid 1%	80.1	15.5	4.4	79.7	16.0	4.3
Grid 2%	73.5	17.6	8.9	73.2	17.8	9.0
Grid 3%	66.9	19.5	13.6	70.3	22.1	7.6
Star 0.1%	89.4	10.2	0.4	89.2	10.4	0.4
Star 0.5%	84.9	13.0	2.1	85.2	12.8	2.0
Star 1%	79.8	15.9	4.3	79.9	15.8	4.3
Star 2%	73.4	17.8	8.8	73.1	18.0	8.9
Star 3%	67.1	19.5	13.4	70.6	21.9	7.5
Star 5%	63.0	15.1	21.9	77.4	18.8	3.8
Star 8%	54.4	11.9	33.7	81.7	16.6	1.7

Table S 5.4. Pseudo-first order rate constant and square regression coefficient for electro-Fenton degradation of trimethoprim ($C_0 = 5$ ppm).

Sample name	**Reaction conditions**		**K_1 (h^{-1} g^{-1})**	**r^2**
	potential (V)	electrolyte pH		
Grid 2%	0.254	7	22.79	1.000
Grid 2%	0.054	7	30.45	0.996
Grid 2%	-0.146	7	40.18	0.995
Grid 2%	-0.323	4	41.08	0.997
Grid 2%	0.031	10	39.75	0.998
Diamond 2%	-0.146	7	35.01	0.999
Star 2%	0.254	7	7.36	0.997
Star 2%	0.054	7	10.13	0.997
Star 2%	-0.146	7	21.26	0.992
Star 2%	-0.323	4	22.43	0.993
Star 2%	0.031	10	20.69	0.992

References

(1) Sun, M.; Chu, C.; Geng, F.; Lu, X.; Qu, J.; Crittenden, J.; Elimelech, M.; Kim, J.-H. Reinventing Fenton Chemistry: Iron Oxychloride Nanosheet for PH-Insensitive H_2O_2 Activation. *Environ. Sci. Technol. Lett.* **2018**, *5* (3), 186–191. https://doi.org/10.1021/acs.estlett.8b00065.

(2) Zhu, Y.; Zhu, R.; Xi, Y.; Zhu, J.; Zhu, G.; He, H. Strategies for Enhancing the Heterogeneous Fenton Catalytic Reactivity: A Review. *Appl. Catal. B.* **2019**, *255*, 117739. https://doi.org/10.1016/j.apcatb.2019.05.041.

(3) Dong, H.; Liu, X.; Xu, T.; Wang, Q.; Chen, X.; Chen, S.; Zhang, H.; Liang, P.; Huang, X.; Zhang, X. Hydrogen Peroxide Generation in Microbial Fuel Cells Using Graphene-Based Air-Cathodes. *Bioresour. Technol.* **2018**, *247*, 684–689. https://doi.org/10.1016/j.biortech.2017.09.158.

(4) Munoz, M.; de Pedro, Z. M.; Casas, J. A.; Rodriguez, J. J. Preparation of Magnetite-Based Catalysts and Their Application in Heterogeneous Fenton Oxidation – A Review. *Appl. Catal. B.* **2015**, *176–177*, 249–265. https://doi.org/10.1016/j.apcatb.2015.04.003.

(5) Verdaguer-Casadevall, A.; Deiana, D.; Karamad, M.; Siahrostami, S.; Malacrida, P.; Hansen, T. W.; Rossmeisl, J.; Chorkendorff, I.; Stephens, I. E. L. Trends in the Electrochemical Synthesis of H_2O_2: Enhancing Activity and Selectivity by Electrocatalytic Site Engineering. *Nano Lett.* **2014**, *14* (3), 1603–1608. https://doi.org/10.1021/nl500037x.

(6) Jirkovský, J. S.; Panas, I.; Ahlberg, E.; Halasa, M.; Romani, S.; Schiffrin, D. J. Single Atom Hot-Spots at Au–Pd Nanoalloys for Electrocatalytic H_2O_2 Production. *J. Am. Chem. Soc.* **2011**, *133* (48), 19432–19441. https://doi.org/10.1021/ja206477z.

(7) Perazzolo, V.; Durante, C.; Pilot, R.; Paduano, A.; Zheng, J.; Rizzi, G. A.; Martucci, A.; Granozzi, G.; Gennaro, A. Nitrogen and Sulfur Doped Mesoporous Carbon as Metal-Free Electrocatalysts for the in Situ Production of Hydrogen Peroxide. *Carbon* **2015**, *95*, 949–963. https://doi.org/10.1016/j.carbon.2015.09.002.

(8) Iglesias, D.; Giuliani, A.; Melchionna, M.; Marchesan, S.; Criado, A.; Nasi, L.; Bevilacqua, M.; Tavagnacco, C.; Vizza, F.; Prato, M.; Fornasiero, P. N-Doped Graphitized Carbon Nanohorns as a Forefront Electrocatalyst in Highly Selective O_2

Reduction to H_2O_2. *Chem* **2018**, *4* (1), 106–123. https://doi.org/10.1016/j.chempr.2017.10.013.

(9) Fellinger, T.-P.; Hasché, F.; Strasser, P.; Antonietti, M. Mesoporous Nitrogen-Doped Carbon for the Electrocatalytic Synthesis of Hydrogen Peroxide. *J. Am. Chem. Soc.* **2012**, *134* (9), 4072–4075. https://doi.org/10.1021/ja300038p.

(10) Choi, C. H.; Kwon, H. C.; Yook, S.; Shin, H.; Kim, H.; Choi, M. Hydrogen Peroxide Synthesis via Enhanced Two-Electron Oxygen Reduction Pathway on Carbon-Coated Pt Surface. *J. Phys. Chem. C* **2014**, *118* (51), 30063–30070. https://doi.org/10.1021/jp5113894.

(11) Zheng, Z.; Ng, Y. H.; Wang, D.-W.; Amal, R. Epitaxial Growth of Au-Pt-Ni Nanorods for Direct High Selectivity H_2O_2 Production. *Adv. Mater.* **2016**, *28* (45), 9949–9955. https://doi.org/10.1002/adma.201603662.

(12) Lu, Y.; Jiang, Y.; Gao, X.; Chen, W. Charge State-Dependent Catalytic Activity of $[Au_{25}(SC_{12}H_{25})_{18}]$ Nanoclusters for the Two-Electron Reduction of Dioxygen to Hydrogen Peroxide. *Chem. Commun.* **2014**, *50* (62), 8464–8467. https://doi.org/10.1039/C4CC01841A.

(13) Yu, M.; Dong, H.; Liu, K.; Zheng, Y.; Hoffmann, M. R.; Liu, W. Porous Carbon Monoliths for Electrochemical Removal of Aqueous Herbicides by “One-Stop” Catalysis of Oxygen Reduction and H_2O_2 Activation. *J. Hazard. Mater.* **2021**, *414*, 125592. https://doi.org/10.1016/j.jhazmat.2021.125592.

(14) Jiang, Y.; Ni, P.; Chen, C.; Lu, Y.; Yang, P.; Kong, B.; Fisher, A.; Wang, X. Selective Electrochemical H_2O_2 Production through Two-Electron Oxygen Electrochemistry. *Adv. Energy Mater.* **2018**, *8* (31), 1801909. https://doi.org/10.1002/aenm.201801909.

(15) Liu, K.; Yu, M.; Wang, H.; Wang, J.; Liu, W.; Hoffmann, M. R. Multiphase Porous Electrochemical Catalysts Derived from Iron-Based Metal–Organic Framework Compounds. *Environ. Sci. Technol.* **2019**, *53* (11), 6474–6482. https://doi.org/10.1021/acs.est.9b01143.

(16) Liu, K.; Yu, J. C.-C.; Dong, H.; Wu, J. C. S.; Hoffmann, M. R. Degradation and Mineralization of Carbamazepine Using an Electro-Fenton Reaction Catalyzed by Magnetite Nanoparticles Fixed on an Electrocatalytic Carbon Fiber Textile Cathode.

Environ. Sci. Technol. **2018**, *52* (21), 12667–12674. https://doi.org/10.1021/acs.est.8b03916.

(17) Li, Z.; Shen, C.; Liu, Y.; Ma, C.; Li, F.; Yang, B.; Huang, M.; Wang, Z.; Dong, L.; Wolfgang, S. Carbon Nanotube Filter Functionalized with Iron Oxychloride for Flow-through Electro-Fenton. *Appl. Catal. B.* **2020**, *260*, 118204. https://doi.org/10.1016/j.apcatb.2019.118204.

(18) Wang, Y.; Zhao, G.; Chai, S.; Zhao, H.; Wang, Y. Three-Dimensional Homogeneous Ferrite-Carbon Aerogel: One Pot Fabrication and Enhanced Electro-Fenton Reactivity. *ACS Appl. Mater. Interfaces* **2013**, *5* (3), 842–852. https://doi.org/10.1021/am302437a.

(19) Chen, W.; Yang, X.; Huang, J.; Zhu, Y.; Zhou, Y.; Yao, Y.; Li, C. Iron Oxide Containing Graphene/Carbon Nanotube Based Carbon Aerogel as an Efficient E-Fenton Cathode for the Degradation of Methyl Blue. *Electrochim. Acta* **2016**, *200*, 75–83. https://doi.org/10.1016/j.electacta.2016.03.044.

(20) Zhang, D.; Liu, T.; Yin, K.; Liu, C.; Wei, Y. Selective H_2O_2 Production on N-Doped Porous Carbon from Direct Carbonization of Metal Organic Frameworks for Electro-Fenton Mineralization of Antibiotics. *J. Chem. Eng.* **2020**, *383*, 123184. https://doi.org/10.1016/j.cej.2019.123184.

(21) Drogui, P.; Elmaleh, S.; Rumeau, M.; Bernard, C.; Rambaud, A. Hydrogen Peroxide Production by Water Electrolysis: Application to Disinfection. *J. Appl. Electrochem.* **2001**, *31* (8), 877–882. https://doi.org/10.1023/A:1017588221369.

(22) Ganiyu, S. O.; Huong Le, T. X.; Bechelany, M.; Esposito, G.; van Hullebusch, E. D.; Oturan, M. A.; Cretin, M. A Hierarchical CoFe-Layered Double Hydroxide Modified Carbon-Felt Cathode for Heterogeneous Electro-Fenton Process. *J. Mater. Chem. A* **2017**, *5* (7), 3655–3666. https://doi.org/10.1039/C6TA09100H.

(23) Shen, X.; Xiao, F.; Zhao, H.; Chen, Y.; Fang, C.; Xiao, R.; Chu, W.; Zhao, G. In Situ-Formed PdFe Nanoalloy and Carbon Defects in Cathode for Synergic Reduction–Oxidation of Chlorinated Pollutants in Electro-Fenton Process. *Environ. Sci. Technol.* **2020**, *54* (7), 4564–4572. https://doi.org/10.1021/acs.est.9b05896.

(24) Wang, Y.; Zhao, G.; Chai, S.; Zhao, H.; Wang, Y. Three-Dimensional Homogeneous Ferrite-Carbon Aerogel: One Pot Fabrication and Enhanced Electro-

Fenton Reactivity. *ACS Appl. Mater. Interfaces* **2013**, *5* (3), 842–852. https://doi.org/10.1021/am302437a.

(25) Munn, A. S.; Ramirez-Cuesta, A. J.; Millange, F.; Walton, R. I. Interaction of Methanol with the Flexible Metal-Organic Framework MIL-53(Fe) Observed by Inelastic Neutron Scattering. *Chem. Phys.* **2013**, *427*, 30–37. https://doi.org/10.1016/j.chemphys.2013.05.017.

(26) Lu, Z.; Chen, G.; Siahrostami, S.; Chen, Z.; Liu, K.; Xie, J.; Liao, L.; Wu, T.; Lin, D.; Liu, Y.; Jaramillo, T. F.; Nørskov, J. K.; Cui, Y. High-Efficiency Oxygen Reduction to Hydrogen Peroxide Catalysed by Oxidized Carbon Materials. *Nat. Catal.* **2018**, *1* (2), 156–162. https://doi.org/10.1038/s41929-017-0017-x.

Chapter 6 Future Outlook

By diagnosing the electrode processes and optimizing the electrode materials as well as the structures, this thesis has improved the catalytic performance, energy efficiency, and design costs, enabling the wider application of electrochemical water treatment systems. Based on the findings of this thesis, future research should be focused in the following three areas.

6.1 Studying the electronic interaction in mixed metal oxides to develop anodes that couple catalytic activity with stability

By employing various characterization methods and scanning electrochemical microscopy (SECM) in Chapter 3, this thesis began to illuminate the catalytic sites in crystalline $CoSb_2O_6$, a next-generation noble-metal-free anode for chlorine evolution reaction (CER) catalysis. We observed that the Sb sites showed even higher catalytic activity than the Co sites, even though Sb oxides normally possess no catalytic activity under ambient conditions. The XPS results indicated that this might be due to the electronic interactions between Co and Sb, which enabled Sb to become an active catalyst. This is consistent with the previous discoveries on RuO_2-TiO_2 anodes, where TiO_x was proposed both experimentally[1] and computationally[2,3] as a catalytic site due to the electronic interaction with RuO_x. This phenomenon is worth further study. Considering the relatively low price and higher acid resistance of Ti and Sb oxides compared to those of Ru and Co, this “Midas touch” effect, once carefully controlled, is highly promising for the development of anodes that couple catalytic activity, long service lifetime, and low price.

6.2 Tuning the macroscopic structure of the electrodes to facilitate mass transport

Despite the enthusiasm of research community in finding more intrinsically active catalysts, mass transport is equally important in practical water treatment systems. Chapter 4 and Chapter 5 illustrated that it is possible to dramatically enhance the electrochemical water treatment performance by tuning the macroscopic structure of the electrodes to facilitate the mass transport. In both chapters, the enhanced performance was obtained without changing the nature of the catalyst or increasing the mass loading of the catalyst. Compared to the traditional strategy where the reactor was filled with electrode arrays to ensure the mass transport, this revolutionary electrode design can substantially lower the material cost. More engineering-inspired research is needed to successfully translate the scientific advancements into wider application of electrochemical water treatment systems.

6.3 Developing high-performance electro-Fenton cathodes for decentralized water treatment

The Fenton process, one of the most studied advanced oxidation processes (AOPs), has been successfully applied in conventional centralized water treatment plants as the tertiary treatment step. However, conventional Fenton process requires external addition of both H_2O_2 and Fe salts, limiting its application in remote areas. Heterogeneous electro-Fenton (HEF) overcomes these limitations by in situ generating H_2O_2 through electrochemical oxygen reduction reaction (ORR), and activating the H_2O_2 to produce $\cdot OH$ via the embedded solid Fe species. The performance of HEF systems depends on the cathode. Chapter 5 illustrates that carbon lattice cathodes degrade and mineralize aqueous pharmaceuticals with a minimal energy input, demonstrating the potential of HEF systems to be used for decentralized water treatment. Future research should be focused on developing high-efficient HEF cathodes and promoting the HEF systems as a decentralized water treatment solution.

References

(1) Finke, C. E.; Omelchenko, S. T.; Jasper, J. T.; Lichterman, M. F.; Read, C. G.; Lewis, N. S.; Hoffmann, M. R. Enhancing the Activity of Oxygen-Evolution and Chlorine-Evolution Electrocatalysts by Atomic Layer Deposition of TiO_2. *Energy Environ. Sci.* **2019**, *12* (1), 358–365. https://doi.org/10.1039/C8EE02351D.

(2) Karlsson, R. K. B.; Hansen, H. A.; Bligaard, T.; Cornell, A.; Pettersson, L. G. M. Ti Atoms in $Ru_{0.3}Ti_{0.7}O_2$ Mixed Oxides Form Active and Selective Sites for Electrochemical Chlorine Evolution. *Electrochim. Acta* **2014**, *146*, 733–740. https://doi.org/10.1016/j.electacta.2014.09.056.

(3) Exner, K. S.; Anton, J.; Jacob, T.; Over, H. Controlling Selectivity in the Chlorine Evolution Reaction over RuO_2 -Based Catalysts. *Angew. Chem. Int. Ed.* **2014**, *53* (41), 11032–11035. https://doi.org/10.1002/anie.201406112.